Title
Optimization of a Laser Plasma Accelerator through Pulse Characterization and Controlled Spatiotemporal Coupling

Author
Mittelberger, Daniel E.

Publication Date
2017

Peer reviewed|Thesis/dissertation

Optimization of a Laser Plasma Accelerator through Pulse Characterization and Controlled Spatiotemporal Coupling

by

Daniel E. Mittelberger

A dissertation submitted in partial satisfaction of the

requirements for the degree of

Doctor of Philosophy

in

Physics

in the

Graduate Division

of the

University of California, Berkeley

Committee in charge:

Professor Wim P. Leemans, Co-chair
Professor Marjorie D. Shapiro, Co-chair
Professor Jonathan S. Wurtele
Professor David T. Attwood

Fall 2017

Optimization of a Laser Plasma Accelerator through Pulse Characterization and Controlled Spatiotemporal Coupling

Abstract

Optimization of a Laser Plasma Accelerator through Pulse Characterization and Controlled Spatiotemporal Coupling

by

Daniel E. Mittelberger

Doctor of Philosophy in Physics

University of California, Berkeley

Professor Wim P. Leemans, Co-chair

Professor Marjorie D. Shapiro, Co-chair

Unlike conventional accelerators, the accelerating structure in a laser plasma accelerator (LPA) is dynamically created by the interaction of a high-peak-power laser pulse with a plasma target. This dynamic nature allows extensive control over the acceleration process but requires detailed knowledge and regulation of the laser, the plasma target, and their interaction. In this thesis, the effect of laser pulse structure, in particular temporal profile and spatiotemporal coupling, on laser plasma acceleration is investigated through theoretical models and experiments at the BErkeley Laboratory Laser Accelerator (BELLA) Center. The temporal profile of the laser and the density profile of the plasma target are probed by laser spectral shifting. A novel model of laser steering and electron beam deflection due to pulse front tilt is developed. The effects of pulse front tilt are measured in experiments and found to be in good agreement with the theoretical model. The application of these results for the optimization of a laser plasma accelerator is discussed.

To my parents, Ralph and Harriett

Who always support me in whatever I do.

Contents

List of Figures

List of Tables

Acknowledgments

I would like to acknowledge Wim Leemans, my advisor. When I joined the BELLA Center (née LOASIS) in 2010, Wim could often be found in the lab, adjusting optics in the laser amplifiers or helping a student fix a HeNe. As I have transitioned from student to scientist, he has assumed a leadership role as both the head of the BELLA Center and Director of the Accelerator Technology and Applied Physics Division at Lawrence Berkeley National Laboratory. Despite his shifting responsibilities, Wim always knew what his students were working on and was available to give guidance. When I was in the hospital in Fall 2011 Wim visited me multiple times, and as I came back to work in 2012 he never pressured me to work harder or longer hours, despite my lengthy transition back into the lab.

Many people contributed to the research which is presented in this thesis and to my development as a young scientist. I would like to thank the scientists at BELLA who worked with me on my thesis experiments: Anthony Gonsalves, Kei Nakamura, Hann-Shin Mao, Sven Steinke, and Csaba Toth. In particular, Anthony Gonsalves and Kei Nakamura provided extensive guidance and feedback during the experiments and subsequent analysis. I would also like to thank Carlo Benedetti, Maxence Thévenet, and Remi Lehe for the numerous simulations they ran on my behalf and for their contributions to the theory presented in this thesis. In addition, I must acknowledge the Building 71 Machine Shop, led by Don Syversrud, for innumerable last-minute prototypes and modifications to parts, general assistance, and a never-ending supply of good humor.

Finally, I wish to acknowledge that my graduate studies and research activities have been financially supported by the Director, Office of Science, Office of High Energy Physics, of the U.S. Department of Energy under Contract No. DE-AC02-05CH11231 as well as by the National Science Foundation, most recently under Grant No. PHY-1415596. This research used the resources of the National Energy Research Scientific Computing Center, a DOE Office of Science User Facility.

Chapter 1

Introduction

1.1 Laser Plasma Accelerators

Particle accelerators are the workhorse of particle and nuclear physics, used to probe subatomic structures since E. O. Lawrence created his first table-top cyclotrons [1] and are an indispensable tool for areas as diverse as condensed matter physics, geology, and protein crystallography through accelerator-driven photon sources [2]. Conventional accelerators based on radio-frequency-technology have a maximum accelerating gradient of $\lesssim$100 MV/m, which is set by material breakdown in the cavity walls [3]. This accelerating gradient sets a minimum size requirement to achieve the particle energies necessary for high-brightness photon sources. For example, the 1.9 GeV electrons in the Advanced Light Source (ALS) require a 197 m circumference accelerator ring [4] in addition to a 75 m circumference booster synchrotron. Particle colliders, with particle energies of hundreds to thousands of GeV, require even larger facilities. The Large Hadron Collider, for example, has a circumference of 27 km. In part because of their increasing size, the historical trend of rising collider energy shown in Figure 1.1 may be slowing in the most recently constructed facilities.

Laser plasma accelerators (LPAs) do not have the same limitations as RF-based accelerator technology and can achieve 1000$\times$ larger particle accelerating gradients, which allows for correspondingly smaller accelerators. Acceleration of electrons to 4.2 GeV ($>$ 2$\times$ the ALS energy) was demonstrated in a 9 cm accelerating structure [5]. LPA experiments have also shown a steady increase in accelerated particle energies, shown in Figure 1.1. As the technology matures, LPAs are poised to transform accelerator science by drastically reducing the physical size of particle accelerators and allowing the construction of linear colliders with energies beyond what is possible with conventional technology. In addition, laser-based accelerators can potentially benefit from economy of scale since high-power ultrafast lasers are increasingly used in an industrial setting and multiple companies now produce laser systems with up to 10 PW peak power. Combined with the smaller size and facility requirements of an LPA, this will potentially increase the availability of photon sources, benefitting the many areas of science which rely on these tools.

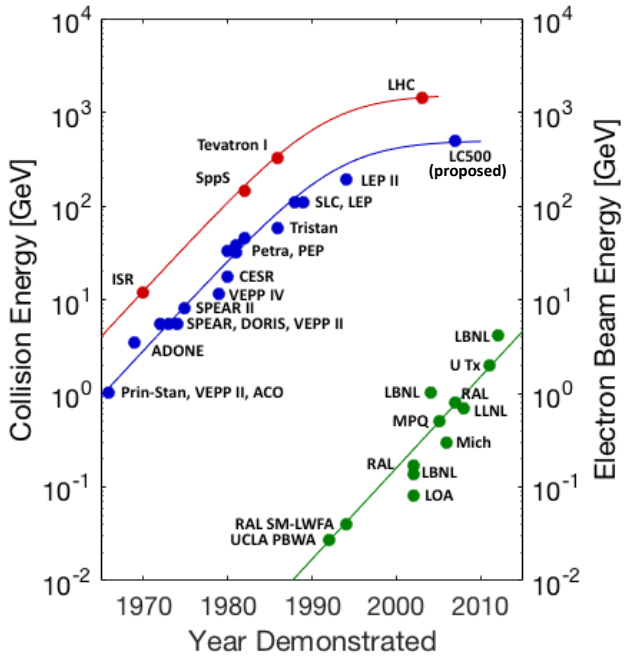

Figure 1.1: Maximum accelerator energies as a function of time. Hadron and lepton colliders (red and blue points, resp.) are plotted against collision energy (the sum of beam energies of the colliding beams). Laser plasma accelerators (green points) are plotted against beam energy. Adapted from [1, 6].

A laser plasma accelerator consists of a high-peak-power ultrafast laser and a plasma target [7]. As the intense laser pulse propagates through the plasma, radiation pressure pushes aside the plasma electrons and creates a wave of displaced electrons in its wake. The electric field associated with this wave can be 10-100 GV/m [3, 8] and is responsible for accelerating and focusing particles. The properties of the accelerated particles depend on the structure and evolution of the laser wake, which in turn are functions of the driving laser pulse and the plasma source. In order to excite a large amplitude wake, the laser pulse must be high power (typically TW-level or higher so the radiation pressure is large) and similar duration to the Langmuir period (1-100 fs for a plasma suitable for particle acceleration).

Peak power and time duration do not completely characterize a laser however, and the structure of the laser pulse (spatial distribution, profile in time, etc.) also influences the performance of the accelerator. An ultrafast laser pulse can have a complicated intensity structure as a function of time, which is related to its spectrum and spectral phase, and may exhibit coupling between its spatial and temporal profiles (spatiotemporal coupling). This coupling may be linear (e.g. the top of the laser arrives before the bottom) or more complicated (e.g. the laser group delay has radial dependence, as in spherical aberration). Pulse front tilt (PFT) is the special case of spatiotemporal coupling in which the group delay is linear in the transverse spatial coordinate. PFT affects the injection [9] and the direction [10] of electrons accelerated by an LPA. It can also seed a hosing instability in the self-guiding of the driving laser pulse [11].

In this work, the effect of pulse front tilt (PFT) in the driving laser pulse of a laser plasma accelerator (LPA) is investigated. A theoretical model of the effect of PFT on the laser-plasma interaction is developed which predicts the steering of the laser pulse due to the asymmetry caused by the PFT, the structure of the resulting plasma wake, and the deflection of accelerated electrons. Spectral modulation due to the interaction of the laser pulse with the neutral gas target and the plasma wake is shown to be useful, both as a diagnostic of the plasma density and potentially of the spectral phase of the laser pulse. Experiments were performed at the BErkeley Laboratory Laser Accelerator (BELLA) at Lawrence Berkeley National Laboratory to measure these effects. The results of these experiments are presented and analyzed with complimentary simulations performed using the particle-in-cell code WARP [12–14] and a version of the code INF&RNO [15–17]. An overview of the BELLA Center LPA system is presented along with a description of the relevant experimental diagnostics below.

1.2 BELLA Center

Accelerator and Diagnostics Overview

The laser plasma accelerator (LPA) in these experiments consisted of the gas jet target together with the BELLA Petawatt laser system. The gas jet was mounted on a remotely-controlled six degree of freedom stage (three translational and three rotational) and could be positioned within a $\sim$4 cm range around the vacuum focus. In addition to the laser amplifiers,

the PW laser system includes a deformable mirror (DM), a four-grating optical compressor, and beam transport optics which transport and focus the compressed laser onto the target. These elements are show in Figure 1.2, where the laser path is indicated in red. The final two beam transport optics are an off-axis paraboloid (OAP) mirror ($f = 13.5$ m) to focus the laser and a final steering mirror to adjust the laser propagation axis, respectively.

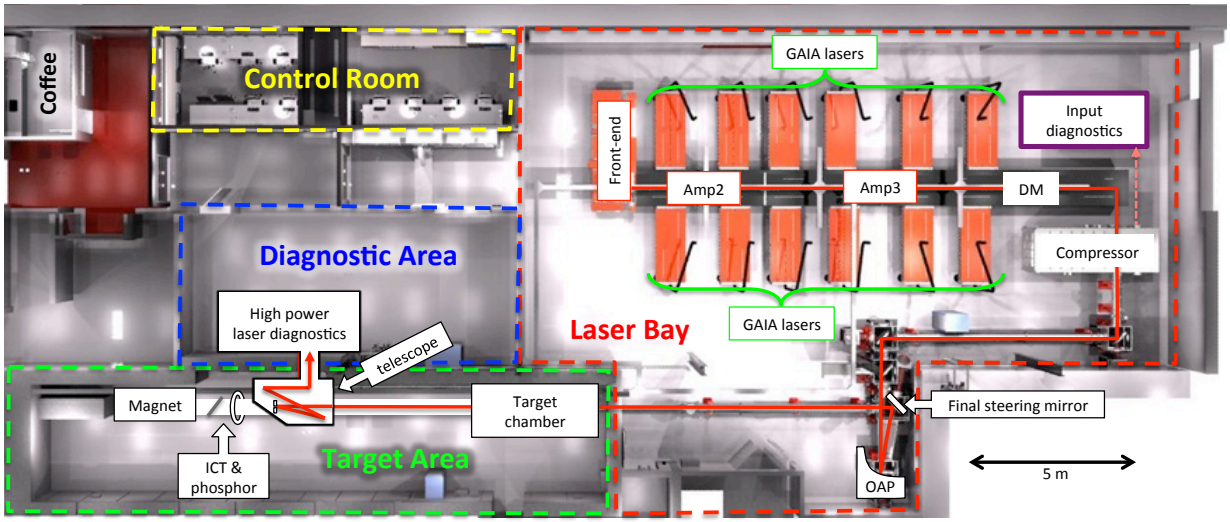

Figure 1.2: Schematic of the BELLA experimental facility. Adapted with permission from [18]

.

The accelerator system incorporates a variety of diagnostics to measure the driver laser and characterize LPA operation and performance. Several plasma diagnostics are located at the target chamber, including the plasma emission camera used to determine the jet orientation in Chapter 3. After the LPA the accelerated electrons and the remaining driver laser are separated, and the electron energy, charge, and spatial distribution are measured in the Target Area. A variety of tools to measure the properties of the laser after the LPA are located in the Diagnostic Area. These laser measurements are also used to characterize the input laser by turning off the gas jet.

There are three primary laser diagnostics after the LPA interaction: the far-field imaging system, the near-field imaging system, and the optical spectrometer. The far-field imaging system consists of an all-reflective telescope that images the LPA region onto a camera on an automated translation stage. The translation stage allows the image plane to be adjusted or scanned through the LPA region. The all-reflective telescope images the laser focus into the Diagnostic Area, where the camera is located, at significantly reduced energy. The telescope consists of an uncoated wedged optical flat with a hole, three uncoated curved optics, a flat window, two flat uncoated optics, and several silver-coated flat mirrors. The first optic

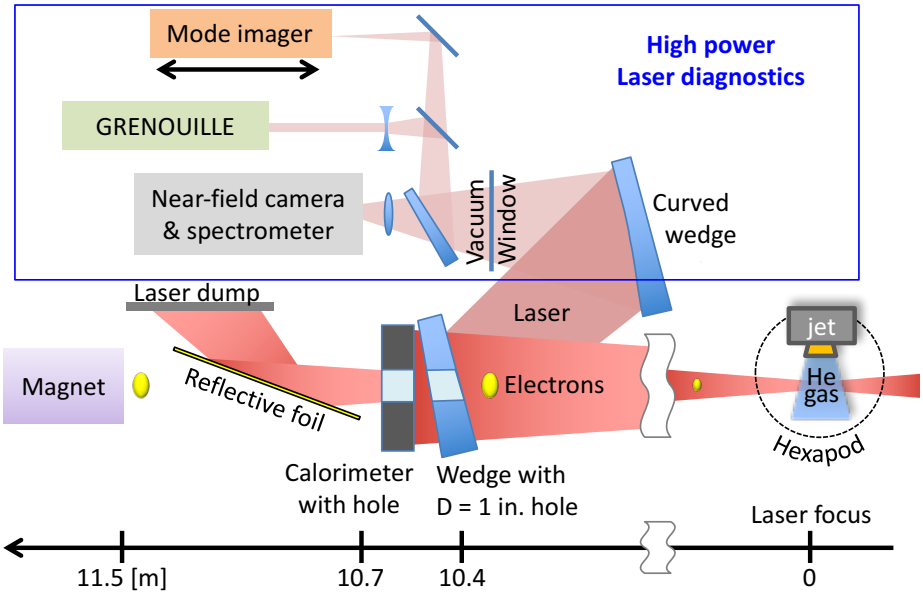

Figure 1.3: Schematic of the electron and laser beam paths after the LPA target. Only the first four telescope optics are included (see text), for simplicity. The relative position of the beamline elements is indicated by the scale at bottom. The target chamber contains a hexapod (*i.e.*, six degrees of freedom) positioner to move the LPA gas jet target. Adapted with permission from [18]

.

separates the laser reflection from the electron beam and has a 1 inch (2.54 cm) hole centered at the optical axis to allow the electron beam to continue straight without passing through material. Since the optic is uncoated, only ∼4% of the incident light is reflected from the front surface for imaging. Without the LPA, far-field imaging system is used to determine the laser focal location and the input laser spatial mode (intensity and phase distribution) as discussed in Chapter 2. The near-field laser diagnostic images the first optic of the telescope (the wedge with hole located 10.4 m downstream of the vacuum focus, as shown in Figure 1.3) onto an imaging screen, which is viewed by a camera. The near-field diagnostic gives the laser output angle, transmission fraction, and near-field spatial distribution. Scattered light from the near-field diagnostic imaging screen is also collected and sent to an optical spectrometer to measure the spectral modulation due to the laser-plasma interaction or the initial laser spectrum if the gas jet is off.

The three diagnostics of the electron beam properties are the magnetic spectrometer, the imaging phosphor screen, and the integrating current transformer (ICT). The magnetic spectrometer yields the energy spectrum of the electrons accelerated by each laser pulse. The ICT and the phosphor screen each give independent measurements of the total charge of electron bunches. The phosphor screen also yields their spatial distribution. After the

LPA the electron beam must pass through the 1 in. (25.4 mm) diameter hole in the first telescope optic. The accelerated electrons then pass through a hole of the same size in a laser calorimeter and through an optically reflective foil, to eliminate any remaining laser light. The electron beam then strikes the imaging phosphor, if it is inserted, and passes through the ICT ring. Because the electron beam must pass through a series of apertures, the acceptance of the the electron beam diagnostics is limited to ±1.2 mrad (4.5 μsr of total solid angle). As a result, many electron beams from these experiments were partially obscured (clipped). Finally, the electrons enter the magnetic spectrometer.

1.3 Thesis Overview

The subsequent chapters detail the BELLA laser and gas jet plasma target, the theory of their interaction, and experiments which validate this theory. A summary of the structure of this work is presented below.

The temporal and spatial structure of ultrafast lasers are discussed in Chapter 2 along with diagnostics used to determine laser structure. The measured temporal and spatial profiles obtained for the BELLA laser system are given. Coupling of a laser's spatial and temporal profiles (spatiotemporal coupling) is discussed, and measurements are presented of controlled spatiotemporal coupling of the BELLA laser resulting in pulse front tilt.

The density distribution of the experimental plasma target, a helium gas jet, is characterized in Chapter 3. Interferometric and tomographic measurements of the gas jet are presented, and the density trends measured by interferometry are explained by the results of an electromechanical model of the jet's operation. This model is given in the supplementary Appendix A. Based on the tomographically reconstructed three dimensional density distribution and the alignment of the gas jet to the BELLA laser, the density profile and transverse density gradients along the laser propagation axis are determined. The details of the jet alignment determination are given in Appendix B.

In Chapter 4, plasma wave formation from high-peak-power ultrafast laser pulses is described along with the guiding effect of the plasma wave on the laser pulse. The results of this discussion are applied to explain how plasma waves can be used to guide and accelerate particles, creating a laser plasma accelerator. A theory of laser steering in the presence of pulse front tilt is developed and benchmarked against two-dimensional particle-in-cell simulations. A model of the effect of pulse front tilt on the wake structure is presented, and the resulting deflection of accelerated electrons is derived. This theory is compared in Chapter 6 with measurements of electron deflection performed at the BELLA Center.

Applying the results of Chapter 4, two methods of charactering the laser-plasma interaction are presented in Chapter 5 based on spectral modulation of the driving laser pulse. A technique of determining the laser temporal profile *in-situ* based on ionization blue-shifting [19] is presented. The density profile experienced by the laser pulse in pulse front tilt experiments is checked against the density profile from tomographic reconstruction given in Chapter 3. The

density profiles in the experiment is determined by simulating the laser-plasma interaction and comparing the simulated spectrum with the laser spectra measured in the experiment.

In Chapter 6, laser plasma acceleration experiments performed at the BELLA Center are discussed, beginning analysis of the laser and electron beam pointing diagnostics. Performance of the LPA system in the absence of spatiotemporal coupling is presented, and then the results of controllably adding pulse front tilt to the drive laser are analyzed. The measurements are explained with the theory developed in Chapter 4 and compared with complimentary three-dimensional WARP simulations.

The results of the preceding Chapters are summarized in Chapter 7, and conclusions about the significance of pulse front tilt for laser plasma acceleration are discussed. Possible applications and future directions for research are also presented.

Chapter 2

Laser Structure and Characterization

The focus of this thesis is the impact of laser structure on laser-plasma interactions and, in particular, on laser plasma accelerators. To facilitate the explanation of these effects, an overview of the relevant aspects of ultrafast (timescale $\lesssim 1$ ps) laser structure is presented in this chapter along with the methods used to characterize them. First, an introduction is provided to the formal description and generation of ultrafast laser pulses. Several techniques for determining the laser properties described by this formalism are discussed, and the structure of the BELLA laser pulse is characterized via these methods. In particular, the temporal mode and spatiotemporal coupling of the laser pulses are examined.

A laser (Light Amplification by Stimulated Emission of Radiation) is a system which amplifies light by stimulated emission from a gain medium (the lasing medium) or the light produced by such a system. The defining properties of laser light are that it has spatial and temporal coherence and that it is polarized. It is assumed here and in the remainder of the text that the laser polarization is fixed, which is true for the BELLA laser used in these experiments and for most laser systems. Because electromagnetic theory is linear, an arbitrary light field can be expressed as a sum of light components with different directions, frequencies, polarizations, and phases. Coherence is the property of having a well defined phase relationship between these different components of the light field. The dependence of this phase relationship on space and time determines many of a laser's properties. In particular, the spatial dependence determines how a laser pulse's intensity profile will evolve with time.

Lasers are typically highly directional, and their propagation is primarily along a single direction (*i.e.*, they are beams). Propagation is assumed throughout to be in the z-direction with no loss of generality. Because of this directionality, the laser light field in vacuum can typically be decomposed into a transverse spatial profile $E_s(\vec{r})$ that is only a function of position and a temporal profile $E_t(\tau)$ that is only a function of position in the pulse $\tau = t - z/c$. Explicitly, this decomposition is

$$\vec{E}(\vec{r}, t) = \vec{\epsilon} E_0 E_s(\vec{r}) E_t(\tau). \tag{2.1}$$

The electric field polarization is in the $\vec{\epsilon}$-direction, which could be linear or elliptical, but is

assumed to be fixed. The profiles E_{trans} and E_{long} are normalized to unity by convention (*i.e.*, the maximum of the function magnitude is set to unity), and the scalar E_0 is the electric field amplitude. In this decomposition, the phase can be also decomposed into a transverse spatial phase and a longitudinal temporal phase. Explicitly, this is

$$\vec{E}(\vec{r},t) = \vec{\epsilon}E_0|E_s(\vec{r})||E_t(\tau)|e^{i\theta_s(\vec{r})}e^{i\theta_t(\tau)}. \tag{2.2}$$

The real, measurable electric field is the real component of the complex function $\vec{E}(\vec{r},t)$. Exceptions to the validity of this decomposition into separate spatial and temporal profiles include very tight focusing (e.g. focusing by an $f/2$ optic), multidirectional focusing (e.g. focusing by an axicon), and laser temporal profiles that depend on position (e.g. one half of the laser is delayed relative to the other).

The laser's phase determines many of its properties. The transverse spatial phase determines the pulse's propagation. For example, a parabolic spatial phase $\theta_s = -\pi(x^2 + y^2)\,/\,\lambda f$ at $z = -f$ corresponds to focusing from a focal length f optic on the origin. Optical aberrations of the laser pulse, which affect the focus quality, or high order modes contribute more complicated spatial phases. The temporal phase determines the instantaneous frequency of the laser, which is not typically a constant. Dependence of the instantaneous frequency on time is called temporal chirp.

2.1 Spectral and Temporal Structure

An arbitrary laser pulse in vacuum can be decomposed because of Fourier's theorem into a sum of plane waves with different directions:

$$E(\vec{r},t) = \frac{E_0}{(2\pi)^4}\iint E(\vec{k},\omega)e^{i(\omega t - \vec{k}\cdot\vec{r})}d\vec{k}\,d\omega. \tag{2.3}$$

If the decomposition in Eqn. 2.1 is valid, then this can be rewritten as

$$\begin{aligned} E(\vec{r},t) =& E_0E_s(\vec{r})E_t(\tau) \\ =& E_0\left[\frac{1}{(2\pi)^3}\iiint \tilde{E}_s(\vec{k})e^{-i\vec{k}\cdot\vec{r}}d\vec{k}\right]\left[\frac{1}{2\pi}\int \tilde{E}_t(\omega)e^{i\omega\tau}\,d\omega\right] \end{aligned}$$

Spectral Domain Representation

Definition of Spectral Phase

Any analytic temporal profile $f(\tau)$ can be expressed exactly as a sum of continuous frequency components, each with its own amplitude and phase, based on Fourier's Theorem. Because ultrafast laser pulses are short in time, they are necessarily composed of a wide range of frequencies. Explicitly, these components are given by the Fourier transform $\mathcal{F}_{(\tau,\omega)}$ and its

inverse $\mathcal{F}^{-1}_{(\tau,\omega)}$, given by

$$\begin{aligned}\tilde{f}(\omega) &= \mathcal{F}_{(\tau,\omega)} f(\tau) = \int f(\tau) e^{-i\omega\tau} d\tau \\ f(\tau) &= \mathcal{F}^{-1}_{(\tau,\omega)} \tilde{f}(\omega) = \frac{1}{2\pi} \int \tilde{f}(\omega) e^{i\omega\tau} d\omega.\end{aligned} \tag{2.4}$$

The frequency-domain expression $\tilde{f}(\omega)$ is the signal's spectral representation.

With these definitions, the temporal profile from Eqn. 2.1 can be written as an inverse Fourier transform given by

$$E(\tau) = \frac{1}{2\pi} \int_{-\infty}^{\infty} \tilde{E}(\omega) e^{i\omega\tau} d\omega = \frac{1}{2\pi} \int_{-\infty}^{\infty} \sqrt{\tilde{I}(\omega)} e^{-i\phi(\omega)} e^{i\omega\tau} d\omega. \tag{2.5}$$

The phase of the spectral amplitude $\phi(\omega) = -\arg\{\tilde{E}(\omega)\}$ is that frequency component's relative delay and is typically described as a Taylor expansion around the central frequency as

$$\phi(\omega) = \phi_0 + \sum_{n=1}^{\infty} \tfrac{1}{n!} \phi_n (\omega - \omega_0)^n. \tag{2.6}$$

Each term of this expansion has a physical interpretation and has different effects on the temporal profile of the pulse. The first two terms, the phase delay ϕ_0 and the group delay ϕ_1, affect only the phase of the fast oscillating electric field and the time when pulse occurs, respectively, but do not change the envelope shape. However, for pulses shorter than ∼10 fs the phase between the fast field and the envelope is of critical importance. It will be shown that the quadratic term, ϕ_2, stretches the pulse and causes a linear frequency chirp in the time domain. Spectral phase terms become increasingly difficult to conceptualize above the quadratic term. The cubic term, ϕ_3, increases the pulse width and also adds temporal asymmetry to the pulse's intensity profile. Depending on the values of ϕ_2 and ϕ_3 the pulse may have a profile that never crosses zero or may exhibit pre- or post-pulses, smaller pulses of light that precede or follow the main laser pulse when it is compressed.

Temporal Profile

A pulse's temporal profile is intimately linked to its spectrum and spectral phase by a Fourier transform as

$$E_t(\tau) = \sqrt{I_t(\tau)} e^{i\omega_0\tau + i\theta(\tau)} = \mathcal{F}_{\tau,\omega}\left(\tilde{E}_t(\omega)\right) = \mathcal{F}_{\tau,\omega}\left(\sqrt{\tilde{I}_t(\omega)} e^{-i\phi(\omega)}\right)$$

Considering the pulse's time dependence at $z = 0$ is conventional and will be done for the remainder of the Chapter, except where noted. The spatial dependence can be recovered by substituting $t \to \tau$. For this reason, the subscript t on the electric field temporal profile will be dropped. The intensity of the pulse is given by $I(t) = \langle |E(t)|^2 \rangle$ where $\langle\,\rangle$ denotes averaging

over the fast oscillations around frequency ω_0 while the spectrum is given by $\tilde{I}(\omega) = |\tilde{E}(\omega)|^2$. The instantaneous frequency of the pulse is given by

$$\omega(t) = \omega_0 + \frac{\partial\theta(t)}{\partial t}. \tag{2.7}$$

Gaussian Pulses with Spectral Phase

Gaussian temporal profiles have useful properties, and often, even if a laser pulse is not exactly a Gaussian, it is useful to model it as such. Consider a laser whose intensity profile and spectrum are defined by

$$\begin{aligned} I(t) &\equiv I_0 e^{-2\left(\frac{t}{T_0}\right)^2} = \langle |E(t)|^2 \rangle \\ \tilde{I}(\omega) &\equiv \tilde{I}_0 e^{-2\left(\frac{\omega-\omega_0}{\Omega}\right)^2} = |E(\omega)|^2. \end{aligned} \tag{2.8}$$

At time $t = \pm T_0$ and $\omega = \omega_0 \pm \Omega$ the temporal and spectral profiles will have dropped by $1/e^2$ of their peak values, respectively.

Assuming a flat spectral phase ($\phi(\omega) = 0$) reveals a relationship between pulse length and spectrum. From the definition of the inverse Fourier transform

$$\begin{aligned} E(t) =& \frac{1}{2\pi}\int_{-\infty}^{\infty} E(\omega) e^{i\omega t} d\omega \\ =& \frac{1}{2\pi}\int_{-\infty}^{\infty} \sqrt{\tilde{I}_0} e^{-\left(\frac{\omega-\omega_0}{\Omega}\right)^2} e^{i\omega t} d\omega \\ =& E_0 e^{-\frac{1}{4}\Omega^2 t^2} e^{i\omega_0 t} \end{aligned}$$

where $E_0 \equiv (\Omega/2)\sqrt{\tilde{I}_0/\pi}$. Comparison with Eqn. 2.8 shows that $T_0 = 2/\Omega$. It is easier to measure the full width at half maximum, which for a Gaussian is given by

$$T_{\mathrm{FWHM}} \equiv T_0\sqrt{2\log 2} = 2\sqrt{2\log 2}/\Omega = 4\log 2/\Omega_{\mathrm{FWHM}} \tag{2.9}$$

A non-flat spectral phase will modify the temporal profile of a laser pulse. An example of particular interest is a quadratic phase $\phi(\omega) = \frac{1}{2}\phi_2(\omega - \omega_0)^2$. This Fourier transforms as

$$\begin{aligned} E(t) =& \frac{1}{2\pi}\int_{-\infty}^{\infty} \sqrt{\tilde{I}_0} \exp\Big\{-\left(\tfrac{\omega-\omega_0}{\Omega}\right)^2\Big\} \exp\big\{-\tfrac{i}{2}\phi_2(\omega-\omega_0)^2\big\} e^{i\omega t} d\omega \\ =& \frac{2}{T_0^2\alpha^2}\left(1 - \frac{2i\phi_2}{T_0^2}\right)\sqrt{\frac{\tilde{I}_0}{\pi}} e^{i\omega_0 t} \exp\left\{-\frac{t^2}{T_0^2\alpha^2}\right\} \exp\left\{i\frac{2\phi_2}{T_0^4\alpha^2}t^2\right\} \\ \equiv& E_0 e^{-\frac{t^2}{T^2}} e^{i\omega_0 t} e^{i\theta(t)} \end{aligned} \tag{2.10}$$

where $\alpha^2 = 1 + 4\phi_2^2/T_0^4$.

The form of the electric field is defined in the last line to be a Gaussian consistent with the definitions in Eqns. 2.2 and 2.8. Two results can immediately be seen from this inverse Fourier transform. First, the pulse length in the presence of quadratic spectral phase the pulse

$$T = T_0\alpha = T_0\sqrt{1 + \frac{4\phi_2^2}{T_0^4}} \tag{2.11}$$

is strictly greater than or equal to the pulse length set by the spectrum's bandwidth, T_0. Second, the instantaneous frequency given by Eqn. 2.7 is no longer a constant. Instead, it is

$$\omega(t) = \omega_0 + \frac{\partial\theta(t)}{\partial t} = \omega_0 + \frac{4\phi_2}{T_0^4\alpha^2}t. \tag{2.12}$$

The second term is called the temporal chirp, and as seen here it is linear for a Gaussian with purely quadratic spectral phase.

Chirped Pulse Amplification

The limiting factor in scaling up the peak power of laser systems is damage to the laser amplifier components and transport optics. Damage occurs when the fluence (energy per unit area) of laser light exceeds a threshold value that depends on the material and pulse length. For pulses longer than ∼20 ps, the threshold fluence for damage to occur scales as $T^{1/2}$, although for shorter pulses the critical fluence is higher than this scaling predicts [20]. The fluence and risk of damage can be reduced by expanding the laser pulse spatially, reducing its fluence, or by stretching the laser pulse in time, increasing the threshold fluence for material damage. Practically, it is difficult and costly to make arbitrarily large optics so stretching of the laser pulse is used to keep the laser from damaging optics. This is the principle of chirped pulse amplification (CPA): the intensity of the pulse is reduced by adding chirp with frequency-dispersive elements in the laser system, so the stretched pulse can be further amplified without exceeding the damage threshold of the optics [21].

Optical Stretching

In a typical CPA system, pulses are stretched from 10s fs to 100s ps, by adding relative phase between the different spectral components. Positive dispersion, the frequency dependence of most materials, delays shorter wavelengths relative to longer wavelengths (*i.e.*, $dv/d\omega < 0$). Pulses in CPA systems are stretched by positive dispersion, rather than negative dispersion, because a pulse with positive dispersion will be further stretched by lenses or other transmissive optics, moving away from the direction of damage.

A frequency-dispersive element is needed to add spectral phase. Spectral phase can be added by propagating the laser through a material whose the phase velocity depends on frequency. However, spectral phase added by passing through a dispersive material is not simply quadratic and requires adding or removing material from the laser path to adjust. An

alternative method to adjust the spectral phase and length of a short laser pulse is to disperse the laser spectrum, add a relative delay between the color components, and recombine them. Separating the spectrum of a laser pulse via a dispersive element is the physical analogue of a Fourier transform. Likewise, combining the many color components of the spectrum to form a single pulse is analogous to an inverse Fourier transform. At low intensities, the spectral dispersion can be done with prisms or transmissive diffraction gratings, but at high laser powers nonlinear optical effects in the glass become problematic. Reflective diffraction gratings have no intensity-dependent nonlinearities, and for this reason high-peak-power laser systems such as BELLA are stretched and compressed with reflective diffraction gratings.

Stretching is accomplished via a setup like that shown in Figure 2.1(a), although several designs exist. The angle of light from a diffraction grating is given by the grating equation:

$$\sin\theta_{in} + \sin\theta_d = mN\lambda \tag{2.13}$$

where θ_{in} and θ_d are the incoming and diffracted angles, respectively, $m = \ldots, -1, 0, 1, 2\ldots$ is the diffraction order, $\lambda = 2\pi c/\omega$ is the wavelength, and N is the number of diffraction grooves per unit length. Different frequency components travel different path lengths before being recombined, with shorter wavelengths traveling further. The added phase delay from a double-pass stretcher like that shown in Figure 2.1(a) is given [22] by an expansion around the central frequency as

$$\begin{aligned}\phi = &-\frac{2\omega_0 L_{eff}}{c}\cos\theta_0(\cos\theta_0 + \cos\theta_{in}) - \frac{2L_{eff}}{c}[1+\cos(\theta_{in}-\theta_0)](\omega-\omega_0) \\ &+ \frac{1}{2!}\left(\frac{L_{eff}N^2\lambda_0^3}{\pi c^2\cos^2\theta_0}\right)(\omega-\omega_0)^2 + \ldots\end{aligned} \tag{2.14}$$

where L_{eff} is the effective separation of the gratings which depends on the lenses and geometry of the stretcher [23–25] and θ_0 is the diffraction angle (relative to the grating normal) for the central frequency $\omega_0 = 2\pi c/\lambda_0$. The factor in parentheses in the third term is the group delay dispersion.

Optical Compression

Once the pulse is amplified, the highest-possible intensity is usually desired for the interaction point. To achieve high intensity after amplification, a negative dispersion element is used to add the opposite phase to the various color components. After this negative dispersion is added and the frequency components are recombined, all the color components will arrive simultaneously producing the highest possible intensity. To achieve this optical compression effect, a configuration like that shown in Figure 2.1(b) is used. Again, the different color components of the ultrashort pulse travel different path lengths, but to add negative dispersion the longer wavelengths travel the larger distance. By changing the distance between the gratings in the compressor, the group delay dispersion (*i.e.*, the change in delay versus frequency) can be changed. In this way, the compressor can be adjusted to cancel out an arbitrary linear dispersion.

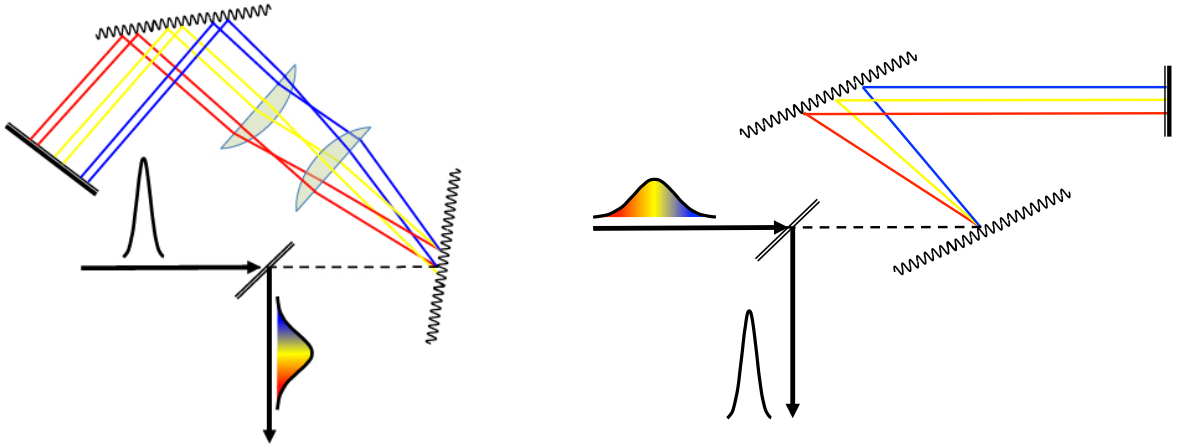

(a) double-pass two-grating optical stretcher (b) double-pass two-grating optical compressor

Figure 2.1: Schematic of (a) an optical stretcher and (b) an optical compressor. In the stretcher, blue light travels a greater distance than red light, while in the compressor red light travels further, adding negative spectral dispersion.

The phase from a double-pass optical compressor like the one show in Figure 2.1(b) at a particular wavelength [26, 27] is

$$\begin{aligned}\phi =& \frac{2\omega L_{eff}}{c}\cos^2\theta_0 + \frac{2L_{eff}}{c}[1+\sin\theta_{in}\cos\theta_0](\omega-\omega_0) \\ & - \frac{1}{2!}\left(\frac{L_{eff}N^2\lambda_0^3}{\pi c^2\cos^2\theta_0}\right)(\omega-\omega_0)^2 + \ldots\end{aligned} \tag{2.15}$$

θ_d is the diffraction angle for the wavelength (relative to the grating normal), θ_0 is the diffraction angle for the central frequency ω_0, L is the perpendicular distance between the gratings, and $L_{eff} = L/\cos\theta_0$ is the grating separation along the path of the central wavelength. Note that group delay dispersion (GDD) from the compressor is the same as that from the stretcher in Eqn. 2.14 with opposite sign.

Other Sources of Spectral Phase

The phase given in Eqns. 2.14 and 2.15 for a stretcher or compressor, respectively, assumes that the gratings are identical and perfectly parallel and that the retro-reflecting mirror, which offsets the incoming and outgoing beams, is perfectly aligned. If the gratings are not identical or any misalignment is present in the compressor then the added phase delay will have additional nonlinear terms which will not be canceled out by the phase from the stretcher [27].

An additional source of spectral phase is self-phase modulation. At high intensities, the index of refraction of a material can become dependent on the intensity of the light. This causes a shift in the instantaneous frequency of the laser pulse. A 1D plane wave propagating in a material with a uniform index of refraction η is described by

$$E = Ae^{i\omega_0\tau + i\Theta(z,t)} = Ae^{i\omega_0 t - ik_0\eta z}$$

where $\tau = t - z/c$ is the position in the wave, $k_0 = \omega_0/c$, and $A = A(\tau)$ is the slowly varyling longitudinal envelope. The temporal phase is thus

$$\Theta(z,t) = (1-\eta)\omega_0\frac{z}{c}.$$

If the index of refraction, η, varies with position, z, then the wave's instantaneous frequency is given by Eqn. 2.7 as

$$\omega(z,t) = \omega_0 + \frac{\partial\Theta}{\partial t} = \omega_0, \tag{2.16}$$

so although the local wavelength is changes to $\lambda = 2\pi\eta/k_0$ the frequency does not change. If instead the index of refraction varies with position in the pulse τ then this is

$$\omega(z,t) = \omega_0 + \frac{\partial\Theta}{\partial\tau} = \omega_0\left(1 - \frac{\mathrm{d}\eta}{\mathrm{d}\tau}z\right) \tag{2.17}$$

which is no longer a constant but depends on the local gradient in index of refraction, as well as how far the wave has propagated in z. When this shift in frequency occurs because a laser pulse is ionizing the gas it propagates through, the effect is called ionization blue shifting.

The index of refraction is proportional to the phase velocity of light in a material, and self-phase modulation can be understood as a gradient in the phase velocity in a coordinate frame that moves with the pulse. In the example of ionization blue shifting the front of the laser is propagating through neutral gas and has a phase velocity of $\sim c$. Because the pulse is ionizing the gas however, the rear of the pulse propagates through a partially or completely ionized plasma, and the phase velocity in plasma is superluminal ($> c$). This means that the light at the rear of the pulse travels faster than light at the front, and so the phase fronts must be squeeze together in the ionizing region as the pulse propagates. This causes a shorter wavelength and higher frequency.

2.2 Measurement of Temporal Profile/Spectral Phase

Laser pulse temporal profile plays an important role in controlling the laser-plasma interaction so accurate diagnostics of pulse length and pulse shape important. There are several methods available to characterize the temporal structure of an ultrafast laser pulse. These include autocorrelation [28], Frequency-Resolved Optical Gating (FROG) [28–30], and Spectral Phase Interferometry for Direct Electric-field Reconstruction (SPIDER) [31].

Intensity Autocorrelation

Autocorrelation determines the length of a pulse by referencing an ultrafast signal to itself with a varying delay. The intensity autocorrelation of a laser pulse is given by

$$S(t') = \int_{-\infty}^{\infty} |E(t)E^*(t-t')|^2 \, dt = \int_{-\infty}^{\infty} I(t)I(t-t')dt \tag{2.18}$$

as a function of t', the delay between the pulse and the reference. This is realized experimentally as in Figure 2.2 by overlapping a pulse with a delayed copy of itself inside of a second harmonic generating (SHG) crystal. The nonlinear optical properties of the crystal combine one photon from each beam to create a frequency-doubled photon. The intensity of the light from the SHG crystal has exactly the form of $S(t')$ as a function of pulse delay. The autocorrelation signal can be isolated from the two input pulses by a filter or by combining the two signals at an angle, in which case the frequency-doubled light will be produced along the angle bisector. The second order autocorrelation function gives the pulse duration if the functional form of the temporal profile is known or assumed [28]. Adding a second SHG crystal to the path of the delayed pulse before creating the autocorrelation signal creates a third order autocorrelator, whose signal contains information about temporal asymmetry in the pulse.

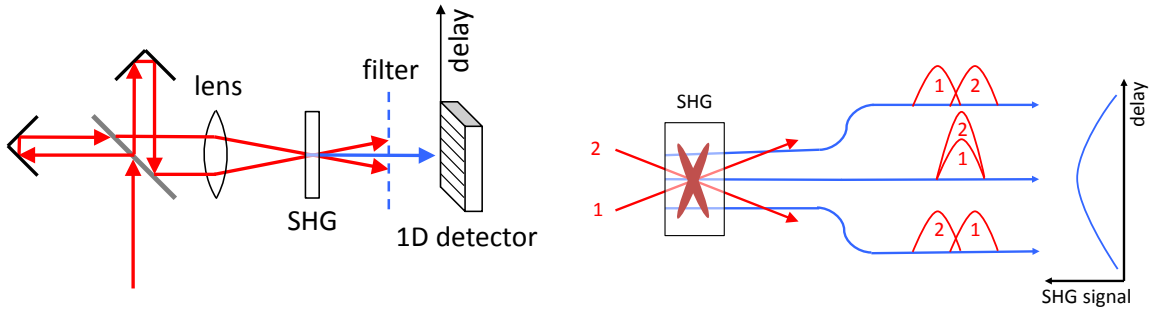

(a) Schematic of an intensity autocorrelator

(b) Schematic of the SHG crystal of a single-shot autocorrelator

Figure 2.2: (a) Single shot autocorrelator consists of second harmonic light generation from two copies of an input pulse that cross at a large angle; (b) the large crossing angle causes delay between the pulses to depend on transverse position within the SHG crystal.

Single Shot Autocorrelation

Because the delay between the two arms of the autocorrelator needs to be scanned, traditional autocorrelation requires many laser pulses and assumes that they are identical. It cannot, therefore, be used to diagnose the shot-to-shot variation on a system. It also cannot be

used for the low repetition rates at which many high peak power lasers operate. These disadvantages can be overcome by a technique called single shot autocorrelation (SSA).

In a single shot autocorrelator, two copies of the input laser pulse are combined at a large angle ($\sim 10°$) in a second harmonic generating (SHG) crystal as in Figure 2.2(b). Because the angle is large, there is a temporal offset between the beams that depends on transverse position in the SHG crystal [32]. Imaging the SHG radiation from the thin crystal onto a detector simultaneously gives the intensity autocorrelation for a range of relative delays can be recorded. This means that the temporal profile of a laser pulse can be characterized with a single pulse, which allows the SSA technique to resolve shot-to-shot fluctuations in pulse duration. The functional form of the temporal profile still must be known or assumed.

FROG and GRENOUILLE

Frequency Resolved Optical Gating (FROG)

A small addition to the single shot autocorrelator dramatically expands its ability to characterize ultrafast laser pulses. Imaging the SHG crystal onto a spectrometer instead of a simple photodetector gives access to the autocorrelation of the pulse as a function of delay and frequency, since the SHG signal is now spectrally dispersed. This technique is called Frequency Resolved Optical Gating (FROG) [29, 30]. The corresponding setup is shown in Figure 2.3(a), although for simplicity the schematic omits two cylindrical optics between the SHG crystal and the detector. This device can fully characterize the temporal profile of the laser pulse without assuming a functional form for the temporal profile. The light signal generated by the SHG FROG is given [30] by

$$S(\omega, t') = \left|\mathcal{F}_{t,\omega}\left\{E(t)E^*(t-t')\right\}\right|^2 \tag{2.19}$$

where $\mathcal{F}_{t,\omega}$ is a Fourier transform from time t to frequency ω. Defining R and $\tilde{R}$ by

$$\tilde{R}(t,t') = E(t)E^*(t-t') = \mathcal{F}_{\omega',t'}\{R(t,\omega')\}$$

the signal from the FROG given in Eqn. 2.19 becomes

$$S(\omega, t') = \left|\mathcal{F}_{t,\omega}\left\{\tilde{R}(t,t')\right\}\right|^2 = \left|\mathcal{F}_{t,\omega}\left\{\mathcal{F}_{\omega',t'}\left\{R(t,\omega')\right\}\right\}\right|^2.$$

It can be shown that $E(t) = R(t, \omega' = 0)$ [30] so recovering the complex-valued function $R(t,\omega')$ completely characterizes the temporal profile of the pulse, including its phase, duration, etc. The problem of recovering a complex signal of two variables ($R(t,\omega')$) from the magnitude of its 2D Fourier transform ($S(\omega,t')$) is known as the "2D Phase Retrieval Problem" and is well-studied.

GRENOUILLE

The FROG setup can be simplified considerably by using a thick (several mm) SHG crystal, shown in Figure 2.3(b). The phase-matched bandwidth in the thick SHG varies with angle

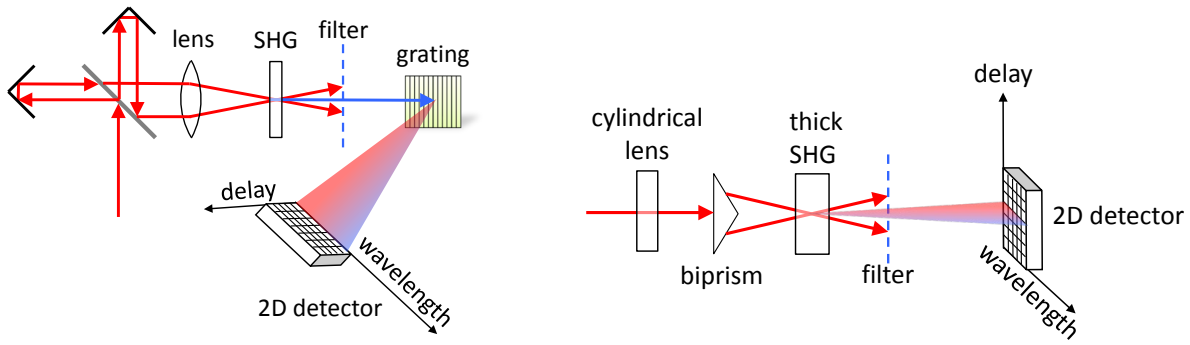

(a) Frequency Resolved Optical Gating (FROG)

(b) GRating Eliminated No-nonsense Observation of Ultrafast Incident Laser Light E-fields (GRENOUILLE)

Figure 2.3: Schematic of (a) a FROG and (b) a GRENOUILLE, with imaging optics before the detector omitted in both schematics.

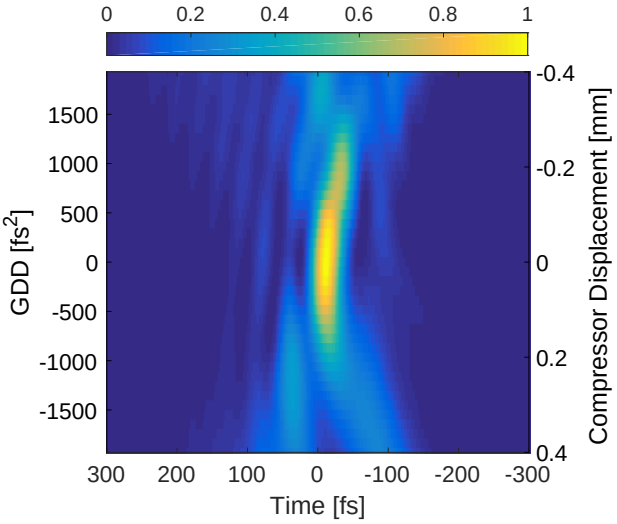

Figure 2.4: Normalized temporal intensity profiles vs group delay dispersion (GDD). Each horizontal line represents the intensity profile vs time at a fixed grating spacing. The residual GDD is caused by displacing the compressor gratings.

which performs the function of the grating or prism of the spectrometer, so the SHG signal is produced and spectrally dispersed at the same time. Further simplification is accomplished by splitting the pulse laterally with a Fresnel biprism and interfering the two sides, rather than making two copies of the entire pulse with a beamsplitter which need to be overlapped with a delay stage. The resulting simplified FROG apparatus is a GRating Eliminated No-nonsense Observation of Ultrafast Incident Laser Light E-fields (GRENOUILLE) [33]. For simplicity, this schematic also omits two cylindrical optics after the SHG crystal.

Phase Measurement for Experiment

The temporal intensity profile and phase of the BELLA laser was characterized [18] on the day of the experiment for a range of GDD values (compressor grating spacings) using a GRENOUILLE located after the main focus of the laser. Together with a model of the spectral phase added by the compressor [18, 27], these measurements were used to create a model of the spectral phase of the laser as a function of GDD. The corresponding temporal intensity profile of the laser for a range of GDD values is shown in Figure 2.2.

2.3 Spatial Profile Determination

With suitable attenuation, the intensity profile of the laser is readily measured by cameras. The near field profile measured at the first optic after the laser focus is shown in Figure 2.5(a) and is close to a 10^{th} order radial super-Gaussian. The image has been corrected for imaging aberrations and for a hole in the optic, and these corrections will be discussed in depth in Chapter 6. Although some high-frequency structure is visible in the near field intensity, the fluctuations are small relative to the absolute intensity of the beam as illustrated by the same image plotted on a logarithmic color scale in Figure 2.5(c). The far field profile shown in Figure 2.5(b) which corresponds to this near field profile consists of a central spot which contains most of the pulse energy and several concentric rings. Although only one concentric ring is readily visible on a linear color scale image, additional rings with significant azimuthal structure are visible in a logarithmic scale view of the far field intensity, shown in Figure 2.5(d).

The spatial profile of the laser near focus determines the laser's vacuum propagation and must be specified for simulations. For the INF&RNO simulations of blue shifting discussed in the previous section the laser profile at focus was an Airy pattern given by Eqn. 5.1, corresponding to a circular "top hat" laser mode of constant intensity in the near field. This is a reasonable approximation considering the uniformity of the intensity and sharpness of cut-off in the near field mode in Figure 2.5(c). Comparing Eqns. 2.2 and 5.1, the changing sign of the Bessel function $J_1(kr/w_0)$ corresponds to a step-wise spatial phase term $\exp\{\pi/2 \pm \pi/2\}$ which switches sign at each zero of the Bessel function at focus. However, the measured beam profile in Figure 2.5(d) has azimuthal as well as radial structure.

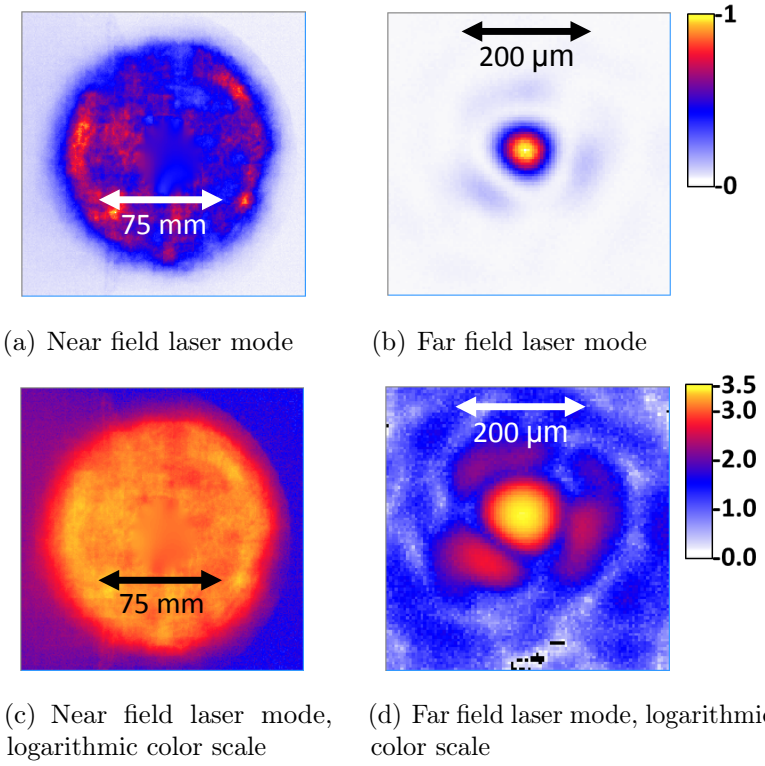

(a) Near field laser mode

(b) Far field laser mode

(c) Near field laser mode, logarithmic color scale

(d) Far field laser mode, logarithmic color scale

Figure 2.5: Near and far field laser modes measured in the experiment.

The Airy pattern model of the laser mode near focus fails to capture several features of the measured laser propagation. The intensity profile of the laser measured near focus is plotted in Figure 2.6(a) as a function of distance to the focal position. Each plot is 500×500 µm. The laser mode is not symmetric on either side of focus, and qualitatively the azimuthal asymmetry in the mode at focus increases with distance from the focal location. In contract, the modeled Airy pattern shown in Figure 2.6(b) is has perfect symmetry in its intensity distribution azimuthally and with respect to focus position.

A more realistic model of the laser mode and propagation was necessary for high-power simulations, in which the spatial mode can affect the evolution of the laser through self-focusing and the acceleration of particles in the LPA (both discussed in Chapter 4). As mentioned in §2.2, the mathematical problem of determining a complex function from it's magnitude and constraints on it's Fourier transform is the 2D Phase Retrieval Process, and several solutions exist [34–36]. The algorithm presented below was applied to a series of images of the laser taken near the vacuum focus, a subset of which are shown in Figure 2.6(a). The resulting estimated wavefront at focus was decomposed into complex-valued Laguerre-Gaussian (LG) modes. The purpose of this decomposition was to remove high-frequency noise and quantitatively characterize the result of the phase retrieval algorithm. A wavefront was calculated from the 420 LG modes ($l \in [-10, +10]$ and $m \in [0, 19]$) of the decomposed

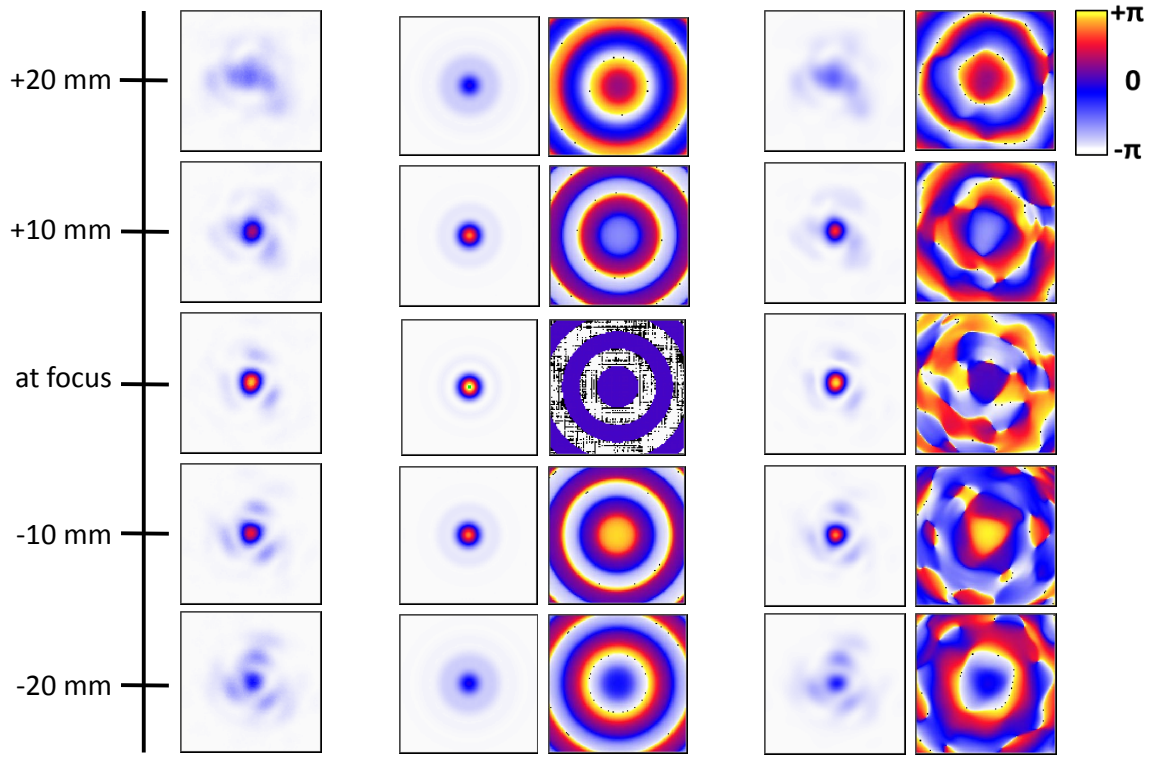

(a) Measured intensity at various distances to focus

(b) Intensity and phase propagated from an Airy pattern

(c) Intensity and phase from retrieved wavefront

Figure 2.6: (a) Measurements of the laser intensity profile have significant non-axisymmetric mode content, despite being a good match near focus to (b) the intensity profile of an Airy pattern, which corresponds to a near-field flat top distribution. (c) The intensity and phase of the laser determined by phase retrieval reproduce the non-axisymmetric laser structure away from focus and allow calculation of the intensity distribution between the locations measured in (a).

estimated wavefront, and this reconstructed wavefront was propagated using Eqn. 2.20 to the locations of each of the measured intensities. The results are shown in Figure 2.6(c).

The approach taken here was a modification of the iterative method of [37]. In that work, the authors determined the best fit complex-valued electric field wavefront $E(x, y, z = \text{fixed}) = \sqrt{I(\vec{r})}\exp\{i\theta(\vec{r})\}|_{z=\text{fixed}}$ to a series of laser intensity images taken through the focal volume. Their method essentially bootstraps a two-image phase retrieval algorithm to create a many-image phase retrieval algorithm. The many-image best fit determination was made by dividing the sequence into pairs of nearest nearest neighbor images, as in Figure 2.7(a), and performing phase retrieval on each image pair via the Gerchberg-Saxton (GS) iterative phase retrieval algorithm [38]. The result from a single image pair is the wavefront that gives the measured intensity at both locations when propagated from one to the other. To create a multi-image phase retrieval algorithm, the wavefront from one image pair was used at the starting point of the GS algorithm for the next pair, resulting in an improving approximation to the true wavefront. This was continued for all intensity images in the sequence, reversing direction until no further improvement in the predicted intensity was observed. The output of the modification was the final guess ("Guess 4" in Figure 2.7(a)).

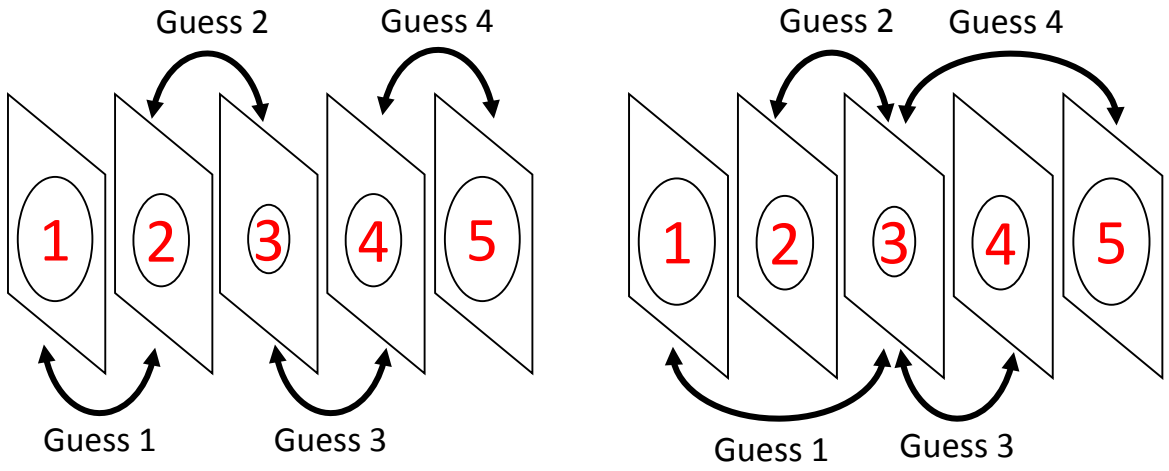

(a) Image comparison order from previous work [37] (b) Image comparison order used in this work

Figure 2.7: The phase retrieval algorithm presented in [37] was improved by changing the order of comparing laser modes from (a) nearest neighbor comparison [37] to (b) comparing the mode at each position with the mode at focus.

In the phase retrieval algorithm used in this work, three modifications were made to the iterative algorithm discussed in [37]. First, rather than sequentially comparing images to their nearest neighbors as in Figure 2.7(a), each image in the sequence was compared to a single reference image, the intensity closest to focus, shown in Figure 2.7(b). The near-focus image had the best signal-to-noise ratio, and this comparison scheme was found to have better convergence properties than the order used in the previous work. Second, a modification of

the Hybrid Input-Output iterative algorithm [39, 40] was used to obtain the wavefront from each pair of images rather than using the GS algorithm. Third, the output of the many-image algorithm was the average complex-valued wavefront from all image pairs, rather than the wavefront from the last image pair to be calculated.

A schematic of the two-image algorithm used here is shown in Figure 2.8 and consists of four steps, each represented by a grey block with a dashed border in the schematic: 1) Magnitude correction at $z = 0$; 2) Propagation from $z = 0$ to $z = \Delta z$; 3) Magnitude correction at $z = \Delta z$; and 4) Inverse propagation from $z = \Delta z$ to $z = 0$. A solution consists of an estimated complex-valued wavefront (magnitude and phase) at $z = 0$ which agrees with the measured intensity at $z = 0$ and with the measured intensity at $z = \Delta z$ when propagated to that location. A consequence of this solution condition is that a solution remains substantially unchanged by further iterations of the two-image algorithm.

The propagation steps of the algorithm are performed via the vacuum propagation operator, which acts on a function of position $\vec{r}$ and is given by

$$\mathcal{P} \star f(\vec{r}) : 0 \rightarrow \Delta z = \mathcal{F}^{-1}\left\{\mathcal{F}\{f(\vec{r})\}e^{ik\Delta z}\right\} \tag{2.20}$$

where $k = \sqrt{\omega/c - k_x^2 - k_y^2} \approx -c(k_x^2 - k_y^2)/2\omega$ is the wavevector in the propagation direction z and k_x and k_y are the coordinates of the Fourier transformed intensity. This assumes the wave is monochromatic with frequency ω, which is a valid approximation provided the feature dimensions of the intensity profile are much larger than the wavelength so $k_x, k_y \ll k$.

The correction steps of the algorithm force the estimated field magnitude toward a value consistent with the measured intensities at both locations but allow the complex phase of the estimated wavefront to vary freely. In general, a new magnitude is calculated via a forcing function $E_{new}(x, y) = f_z(E_{prop}(x, y), I_{meas}(x, y))$ from the propagated wavefront E_{prop} and measured intensity I_{meas}. In the GS algorithm, the corrections consist of replacing field magnitude with $E_{meas} \equiv \sqrt{I_{meas}}$ at each location so the forcing function for the GS algorithm is the trivial function $f_z(E_{prop}(x, y), E_{meas}(x, y)) = E_{meas}(x, y)$. In the Iterative Projection Algorithm in [40], the forcing function is given by $f_z(E_{prop}(x, y), E_{meas}(x, y)) = W_z(x, y)E_{meas}(x, y) + (1 - W_z(x, y))E_{prop}(x, y)$ where $W(x, y)$ is a binary function of position at each location. It is noted in [40] that the algorithm can be extended to functions $W(x, y)$ that take an arbitrary value from 0 to 1. The purpose of the function $W(x, y)$ is to extend the algorithm to situations where $I_{meas}(x, y)$ is not known for all x and y and to incorporate non-magnitude-based constraints. The approach in this work is similar to this weighting-based forcing function except that the relative weighting depends on the field magnitudes instead of just the coordinate positions. Correction with this new weighting scheme was found to give better agreement between the predicted and measured intensity profiles, based on their root-mean-square error, for the intensity measurements discussed here. Dropping the explicit dependance on x and y, the forcing function used in this work is given by

$$E_{new} = f(E_{prop}, E_{meas}) = \left[|E_{prop}| + \text{sign}\{\Delta E\}\frac{\Delta E^2}{|\Delta E| + \epsilon}\right] \tag{2.21}$$

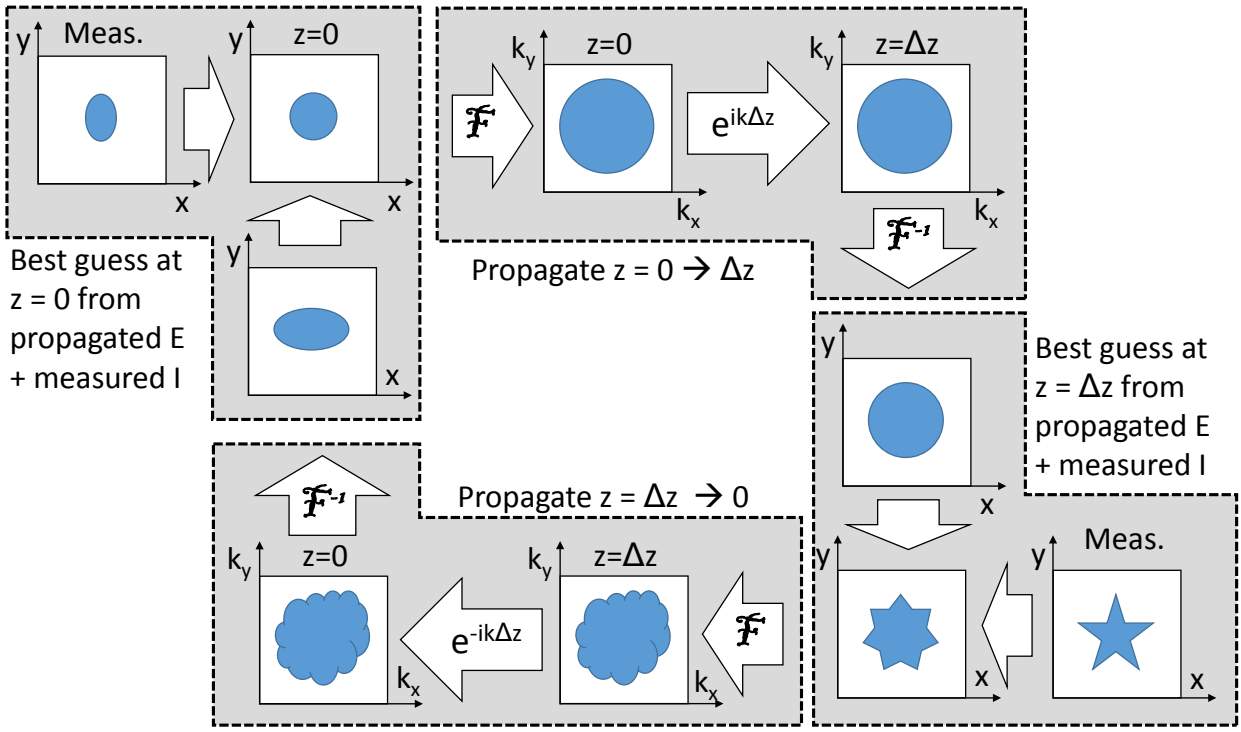

Figure 2.8: The steps in the phase retrieval algorithm to determine the wavefront phase from the measured intensity at two locations.

where $E_{meas} \equiv \sqrt{I_{meas}}$ is the field magnitude associated with the measured intensity, $\Delta E = |E_{meas}| - |E_{prop}|$ is the difference from the field magnitude that is propagated to the location (*i.e.*, the current best guess), and $\epsilon \approx \sqrt{I_{\text{noise}}}$ is an estimate of the noise background level. The form of the forcing function is such that if $|\Delta E| \gg \epsilon$ then the $E_{new} \rightarrow E_{meas}$ as in the GS algorithm, but if $|\Delta E| \lesssim \epsilon$ then the magnitude of the estimated field E_{new} remains approximately the same as predicted by the previous guess E_{prop}.

2.4 Spatiotemporal Coupling

In both a stretcher and compressor the spectrum of a laser pulse is spatially separated and then recombined. Since several optics are involved in these devices, there is a possibility that their alignment and the recombination process is not perfect. One possibility is the color components of the laser may be overlapped spatially but propagate at slightly different directions when they are recombined. This flawed recombination results in angular chirp, where the instantaneous frequency depends on angle. Another possibility is the color components of a laser pulse may be recombined with a small frequency-dependent spatial offset, so the instantaneous frequency of the compressed laser depends on transverse position which is

spatial chirp. In these cases, the decomposition in Eqn. 2.1 is no longer valid since the profile of the laser cannot be separated into functions only of $\vec{r}$ and only of τ. Mixing of the spatial and temporal profiles of a laser pulse is called spatiotemporal coupling. In the pulse front tilt experiments in this thesis, the spatiotemporal coupling of a high-peak-power laser was modified by adjusting the final optical compressor of the BELLA laser plasma accelerator system.

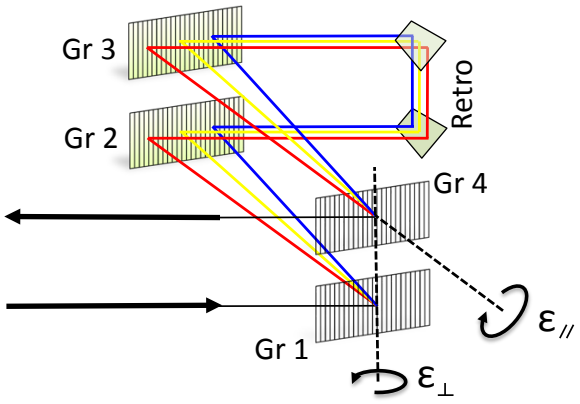

Figure 2.9: Schematic of the final BELLA optical compressor.

An optical compressor with non-parallel gratings will introduce angular dispersion from one grating that is not cancelled out by the other, so the compressed pulse will have residual angular chirp. A simplified schematic of the BELLA compressor is shown in Figure 2.9. As indicated, the first (G1) and fourth (G4) gratings rotate together in the dispersion plane while the fourth grating can be independently rotated about it's surface normal. If G1 and G4 are rotated by a small angle $\epsilon_\perp$ from their ideal orientation around the dispersion plane normal, an angular dispersion of

$$\frac{\mathrm{d}\varphi_x}{\mathrm{d}\lambda} = 2\epsilon_\perp N \frac{\tan\theta_0}{\cos\theta_{in}} \tag{2.22}$$

is added to the compressed laser pulse. Note that φ_x,the horizontal angle of a particular spectral component, is unrelated to the temporal phase, ϕ. If G4 is instead rotated by $\epsilon_{/\!/}$ about it's surface normal, which lies in the dispersion plane, a vertical angular dispersion of

$$\frac{\mathrm{d}\varphi_y}{\mathrm{d}\lambda} = \epsilon_{/\!/} N \tag{2.23}$$

is added to the compressed pulse.

Pulse Front Tilt from Angular Chirp

Angular chirp is a type of spatiotemporal coupling where the propagation direction varies for different spectral component of the laser. The colors of the laser pulse can be angularly

dispersed if the gratings of the optical compressor are not perfectly parallel or if the laser passes through a prism or wedged optic.

To understand the effect of adding angular chirp [41], first assume that $E(\vec{k},\omega) = E(k_x,k_y,k_z,\omega)$ is some distribution that is symmetric in k_x and k_y but strongly peaked in k_z and ω. One example is a product of Gaussians like

$$E(k_x,k_y,k_z,\omega) = E_0 e^{-(k_x/k_0)^2} e^{-(k_y/k_0)^2} e^{-(k_z/k_0-1)^2} e^{-(\omega/\omega_0-1)^2} \tag{2.24}$$

but the specific functional form of the distribution is not important. Next, consider the addition of a frequency-dependent offset to k_x

$$E(k_x,k_y,k_z,\omega) \longrightarrow E(k_x+p\omega,k_y,k_z,\omega) \tag{2.25}$$

where p is a constant so the distribution is no longer symmetric in k_x and the location of the peak varies with frequency ω. This is now a distribution with angular chirp in the xz-plane. For any particular frequency ω, the direction of that spectral component where the $\vec{k}$-distribution peaks has an explicit ω-dependence. Applying the Fourier shift identities

$$\begin{aligned} E(k+\delta k) =& \mathcal{F}_{(x,k_x)}(E(x)e^{-ix\delta k}) \\ E(x+\delta x) =& \mathcal{F}^{-1}_{(x,k_x)}(E(k)e^{ik_x\delta x}) \end{aligned}$$

to the right-hand side of Eqn. 2.25 gives

$$E(k_x+p\omega,k_y,k_z,\omega) = \mathcal{F}_{(\vec{r},\vec{k})}\{E(\vec{r},\omega)e^{-ixp\omega}\} = \mathcal{F}_{(\vec{r},\vec{k})}\left\{\mathcal{F}_{(t,\omega)}\{E(\vec{r},t+px)\}\right\}. \tag{2.26}$$

This expression shows that adding angular chirp creates a temporal offset in the beam that depends on transverse position, as in Figure 2.10. In other words, the arrival time of the beam at a particular z-location varies with transverse position x, so the intensity front of the beam is tilted with respect to the propagation direction. This is pulse front tilt: the existence of an angle between the intensity envelope normal and the propagation direction, as shown in Figure 2.10.

The pulse front tilt angle Θ of the laser in Eqn. 2.26 is given by [42]

$$\tan\Theta = \frac{\mathrm{d}z_0}{\mathrm{d}x} = pc \tag{2.27}$$

where z_0 is the peak intensity at a given transverse offset x. Its angular dispersion (the dependence of propagation angle on frequency) is

$$\beta = \frac{\mathrm{d}\varphi_x}{\mathrm{d}\omega} = \frac{\mathrm{d}}{\mathrm{d}\omega}\left(\frac{k_x}{k}\right) \approx \frac{1}{k_0}\frac{\mathrm{d}k_x}{\mathrm{d}\omega} = p/k_0 \tag{2.28}$$

but it is more convenient to express the angular dispersion as

$$\psi = \frac{\mathrm{d}\varphi_x}{\mathrm{d}\lambda} = -\frac{2\pi c}{\lambda_0^2}\beta = -\frac{pc}{\lambda_0} \tag{2.29}$$

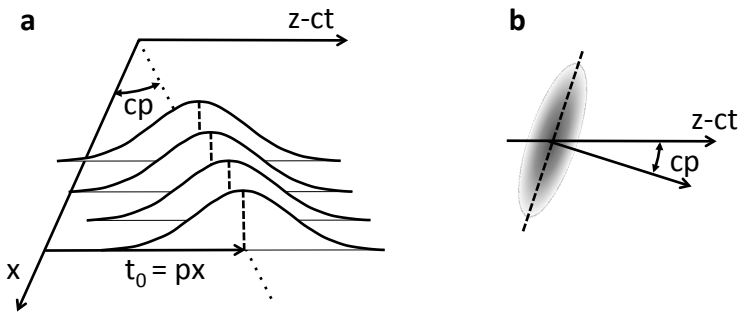

Figure 2.10: (a) Angular chirp causes a temporal offset that depends on transverse position. (b) The angle between the intensity envelope normal and the propagation direction is the pulse front tilt angle, given by pc in the paraxial approximation.

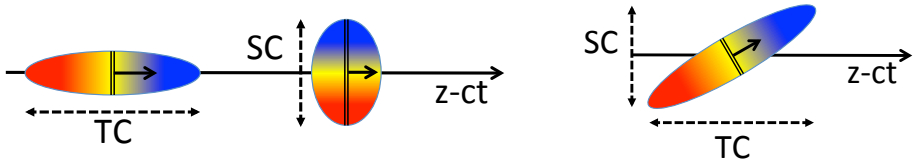

(a) Temporal chirp (TC) and spatial chirp (SC) stretch the laser pulse along and orthogonal to the propagation direction, respectively.

(b) Together, SC and TC stretch the pulse at an arbitrary angle and tilt the intensity front.

Figure 2.11: Spatial chirp stretches the pulse transversely and temporal chirp stretches the pulse longitudinally. Together they cause pulse front tilt.

Pulse Front Tilt from Spatial Chirp

Angular chirp is sufficient to cause pulse front tilt, but it is possible to have pulse front tilt even when no angular chirp is present. A combination of spatial and temporal chirp will also result in pulse front tilt, as illustrated in Figure 2.11(b). Recall that temporal chirp is defined as dependence of a laser's instantaneous frequency on longitudinal position, and its effect is to increase the laser pulse length, as in Figure 2.11(a). Likewise, spatial chirp is dependence of a laser's instantaneous frequency on transverse position. A (linear) temporal chirp is quantified by its GDD ϕ_2 while spatial chirp is described by $\zeta = dx_0/d\omega$, so a wave packet centered at $\omega_0 + \omega$ would be transversely offset and centered at $x_0 = \zeta\omega$. Spatial chirp can be caused by misalignment in an optical compressor or by passing through a thick optic at an angle. In the presence of both spatial and temporal chirp as in Figure 2.11(b), the laser pulse is stretched along an arbitrary direction causing pulse front tilt. The pulse front tilt

from spatial and temporal chirp for a Gaussian pulse is given by [42]

$$p = \phi_2 \nu \tag{2.30}$$

where ν is the transverse frequency gradient, which is given by

$$\nu = \frac{\zeta}{\zeta^2 + \frac{1}{4} w^2 T_0^2} \tag{2.31}$$

where w is the transverse spot size and T_0 is the pulse length if $\phi_2 = 0$ (*i.e.*, the minimum pulse length).

Effect of Focusing and Propagation

As a pulse with pulse front tilt propagates, its angular, spatial, and temporal chirps change. This can be seen for spatial chirp immediately from the dependence of Eqn. 2.31 on spot size $w = w(z)$. The changing spectral dispersion of the pulse results in a changing pulse front tilt angle, given by Eqn. 2.27, as a function of propagation distance. For a Gaussian pulse propagating in z, the initial angular dispersion β_0, initial GDD $\phi_{2,0}$, and initial spatial chirp ζ_0 specified at $z = 0$ evolve as [42]

$$\begin{aligned} \beta(z) =& \beta_0 = \text{constant} \\ \zeta(z) =& \zeta_0 + \beta_0 z \\ \phi_2(z) =& \phi_{2,0} - k_0 \beta_0^2 z. \end{aligned} \tag{2.32}$$

The appearance of spatial chirp with propagation, even if the pulse initially had none, can be understood as a consequence of angular chirp. Each color component moves in a slightly different direction, causing the colors to spread out in the direction of angular dispersion and leading to spatial chirp. The evolution of the pulse described by Eqns. 2.32 leads to an evolving pulse front tilt of

$$p(z) = k_0 \beta_0 + \phi_2(z) \nu(z) \tag{2.33}$$

where $\nu(z)$ is given by Eqn. 2.31 using the propagated values of $\zeta = \zeta(z)$ and $w = w(z)$.

If a pulse with spectral and/or temporal dispersion is focused by a lens or curved mirror, the angular dispersion, spatial chirp, and GDD are changed focusing. One interesting example of this is that near field angular chirp causes spatial chirp at focus because the angle of light before a focusing optic shifts the transverse position of focus. This effect is shown in Figure 2.12(a), which also illustrates why angular dispersion enlarges the focal spot in the direction of angular dispersion. Spatial chirp before focusing causes angular chirp at focus for similar reasons, but because all the color components focus to the same position, albeit at slightly different angles, no change in focus spot size is seen for near field spatial chirp. The conversions from near field values before the focusing optic of focal length f to values at

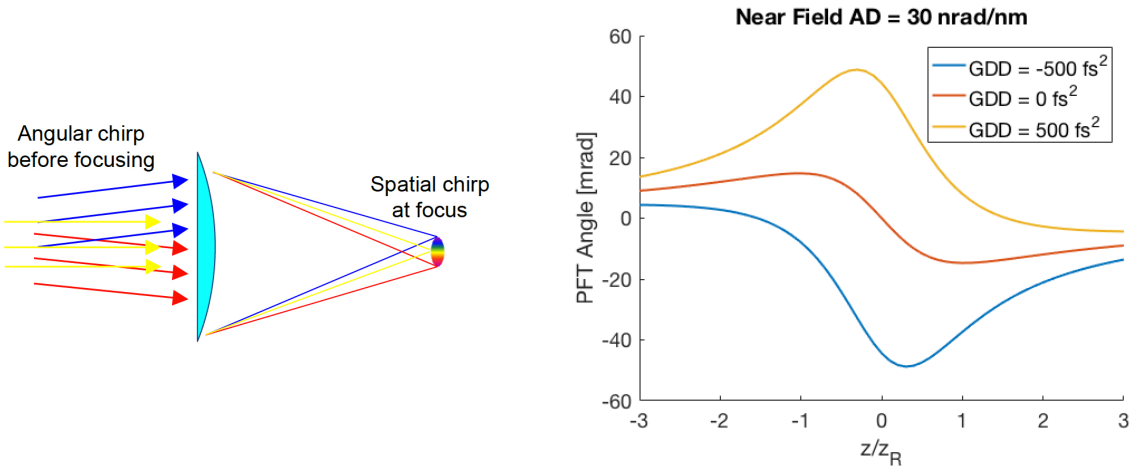

(a) Angular chirp causes spatial chirp at focus

(b) Evolution of pulse front tilt angle with propagation near focus for three values of GDD.

Figure 2.12: Focusing of a pulse with near field angular chirp leads to spatial chirp at focus, so the pulse front tilt angle near focus is sensitive to temporal chirp (GDD).

focus (marked with primes) are given by [43]

$$\begin{aligned} \beta' =& \beta - \frac{\zeta}{f} \\ \zeta' =& \beta f \\ \phi_2' =& \phi_2 - k_0 \beta^2 f + 2 k_0 \zeta \beta. \end{aligned} \tag{2.34}$$

An important consequence of the conversions given in Eqns. 2.34 is that the pulse front tilt angle of a focusing laser with only angular chirp depends on GDD. For a collimated beam, this is not true since the pulse front tilt cause by angular chirp, given by Eqns. 2.27 and 2.28, has no GDD dependence. However the focusing causes spatial chirp which peaks at focus. The effect on the pulse front tilt angle for a Gaussian pulse is plotted in Figure 2.12(b).

2.5 Measurement of Pulse Front Tilt

The angular and spatial chirp of the BELLA laser system were characterized [18] as a function of grating rotation in the dispersion plane ($\epsilon_\perp$ in Figure 2.9) and grating clocking about the grating surface normal ($\epsilon_{/\!/}$ in Figure 2.9). The absolute location of minimum angular chirp was determined by rotating/clocking the gratings and measuring the focal spot elongation due to spatial chirp at focus, as illustrated in Figure 2.12(a). The horizontal focal spot size as a function of grating rotation is shown in Figure 2.13(a), and the vertical focal spot size is plotted as a function of grating clocking in Figure 2.13(b), with the measured spot sizes plotted as black points. In both cases, a blue parabolic fit to the measured focal spot

size yields a minimum (red cross) that defines the zero-point of angular dispersion. The angular dispersion added from rotating or clocking the grating was measured using the GRENOUILLE, which is capable of measuring both spatial chirp and pulse front tilt [42]. An independent metric (the focal spot elongation) is required to determine the zero point of angular dispersion, however, because an internal misalignment of the GRENOUILLE would shift the data points in Figures 2.13(c) and 2.13(d) without affecting their slope. The angular chirp determined by GRENOUILLE measurements of pulse front tilt is plotted in Figures 2.13(c) and 2.13(d) as a function of grating rotation and clocking, respectively. The red lines are a linear fit, with the shaded region representing a 95% confidence region. The blue line is the theoretical curve with slope given by Eqns. 2.22 and 2.23, and it agrees with the red fit to within the confidence region.

Spatial chirp was also measured, and it was found to be negligible for all grating rotations and for grating clockings ≤ 20 µrad (angular dispersion ≤ 26 nrad/nm). This is shown in Figure 2.14 where the pulse front tilt from spatial chirp if GDD = 1000 fs^2 is plotted against the pulse front tilt caused by angular chirp at each value of grating rotation and clocking. In both cases, the quoted pulse front tilt is the value just before the OAP. The spatial chirp contribution only becomes significant at the largest clocking values (the three rightmost blue points in Figure 2.14), and even for GDD = 1000 fs^2 it is still significantly less than the pulse front tilt contribution from angular chirp. For these reasons simulations of laser propagation and laser-plasma acceleration will neglect the small contribution from near field spatial chirp and model only the pulse front tilt resulting from near field angular chirp and GDD.

2.6 Concluding Remarks

In the description of the laser given in this chapter, the laser structure consists of its spatial profile, its temporal profile (equivalently, it's spectrum and spectral phase), and the spatiotemporal coupling between the two. These aspects of the structure of the BELLA laser have been determined by the techniques introduced in this chapter, and their experimental control (*i.e.*, changing pulse length by translating the optical compressor diffraction gratings) has also been discussed. In sum, this chapter has explicated the laser-side of laser plasma interaction.

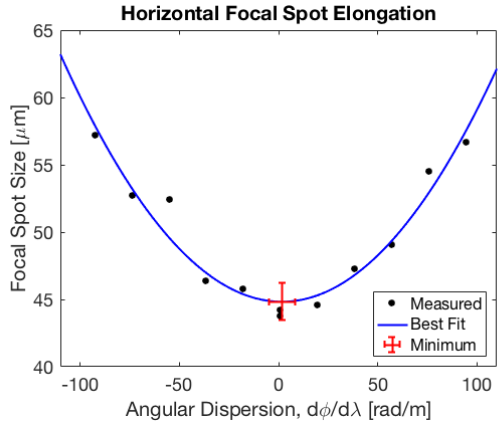

(a) Focal spot enlargement due to grating rotation

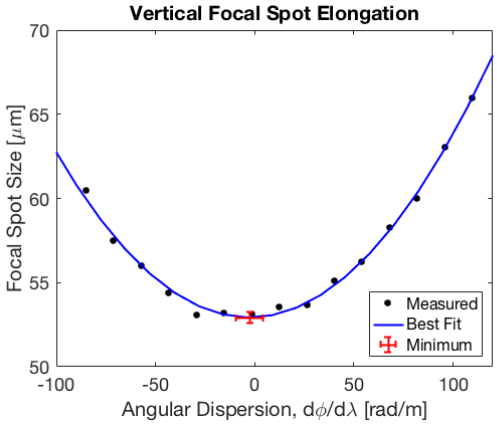

(b) Focal spot enlargement due to grating clocking

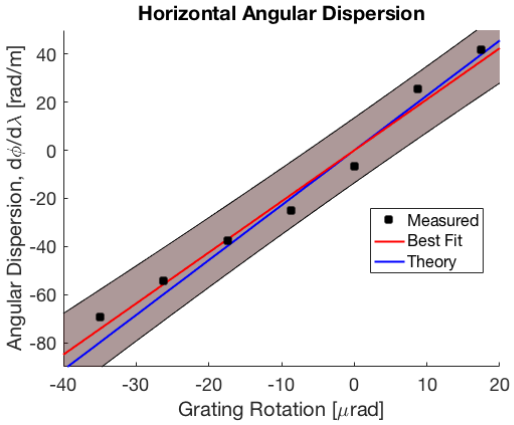

(c) Measured angular dispersion (black), theory (blue), and fit (red with shaded 95% confidence interval) for grating rotation

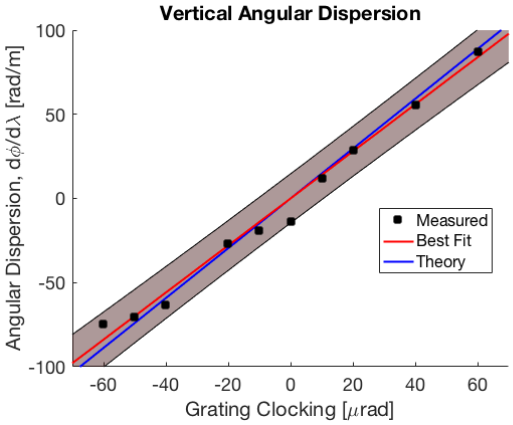

(d) Measured angular dispersion (black), theory (blue), and fit (red with shaded 95% confidence interval) for grating clocking

Figure 2.13: Calibration of the angular dispersion from grating adjustments by GRENOUILLE and focus spot size measurements.

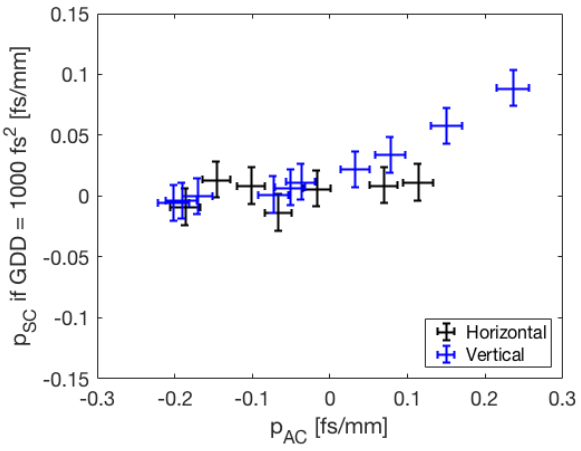

Figure 2.14: Pulse front tilt from spatial chirp (at GDD = 1000 fs^2) plotted against pulse front tilt from angular chirp for the same grating rotation/clocking, showing that spatial chirp can be neglected for most values of grating rotation/clocking.

Chapter 3

Gas Jet Density Characterization

Together with the driving laser pulse, the properties of a laser plasma accelerator are determined by the profile of the plasma through which the laser propagates. In this chapter, the full three-dimensional density distribution of the helium gas jet target used in these experiments is determined. Several important density scaling relationships are also determined. Based on this distribution and the alignment of the jet to the laser axis, the density profile experienced by the drive laser is calculated. The uncertainty in the alignment is used to set limits of the transverse density gradients along the laser path, which can cause deflection of the laser pulse.

Plasma density is one of the key parameters that determines how the laser-plasma interaction occurs. Because of its importance, many diagnostics of plasma density have been developed, such as plasma interferometry [44], Raman spectroscopy [45], and laser wake imaging [46]. In these experiments, the non-axisymmetric density profile of the gas jet target was characterized offline via neutral gas interferometry. This approach has the advantage of characterizing the complete three dimensional density profile of the gas target. In addition to the density profile along the laser propagation axis, the full three dimensional profile can be used to determine the transverse density gradients, which can deflect the laser. The magnitude and uncertainty of the density profile along the laser axis in the experiment was determined from the jet position and angle. The calculated density profile was checked by comparing the measured redshifted laser spectra with simulated laser propagation [15–17] through the density profile for a range of vacuum focal locations.

Two types of interferometry were taken to characterize the gas jet: parameter scans and multi-angle, tomographic scans. For the parameter scans, the viewing angle remained fixed along the jet's long axis while some parameter (e.g. pressure, timing) was varied to determine the relative scaling of the jet density. An electromechanical model of the gas jet was developed to explain the measured scalings. For the tomographic scans, the jet was operated in a steady-state mode and the viewing angle was rotated to allow computational reconstruction of the three-dimensional absolute density profile.

3.1 Gas Jet Operation

The gas target used in these experiments, shown in Figure 3.1(a), was a solenoid gas valve (Alameda Applied Science Corporation) [47, 48], fitted with a supersonic nozzle of rectangular cross section. The output size of the nozzle was 15 mm long by 3.5 mm wide. The valve is sealed by an 0.6 cm diameter o-ring at the end of an aluminum plunger rod with a wide plate near its base. The plunger is held shut by a 250 lb/in spring. A cross section showing the components of the jet is shown in Figure 3.1(b).

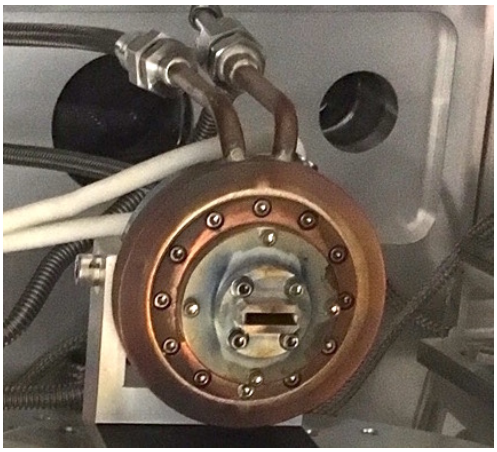

(a) The 1.5 cm slit jet in the BELLA target chamber.

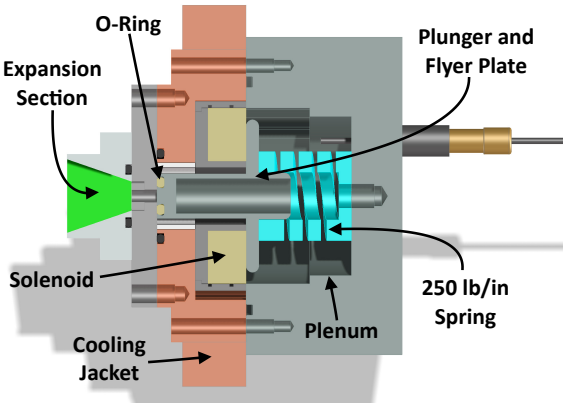

(b) Labeled cross section view of the gas jet.

Figure 3.1: View and schematic of the gas jet with attached nozzle used in these experiments.

The jet is opened when a current pulse is provided by the jet driver. The jet driver consists of a pair of parallel high-voltage $185 \pm 10\%$ µF capacitors, a variable high-voltage supply to charge the capacitors, a diode to ensure the current only flows in one direction, and a switch to discharge the capacitors through the solenoid in the jet. Once triggered, the high side of the solenoid inside the jet plenum is connected in series with the capacitors. The low side of the solenoid is grounded to the jet body, which is connected to a return lead to the jet driver. The current through the solenoid initially rises and then falls to zero, at which point it is blocked by the diode in the jet driver. The rising magnetic field from the solenoid induces eddy currents in the wide plate of the plunger, resulting in an initially repulsive force which repels the plunger rod from the solenoid and opens the value. The magnetic field begins dropping after the peak of the solenoid current which reverses the direction of the eddy currents and causes the force between the plate and the solenoid to become attractive. The spring and the gas pressure also provide restoring force to reseal the valve.

3.2 Density Scaling

Interferometry

A direct method of gas density measurement is interferometry. An interferometer records the relative delay of rays of light traveling through a distribution of transparent matter in a finite volume. If a number of parallel rays travel through a distribution of gas, the rays which propagate through more gas will experience a phase delay relative to those that pass through less gas or through vacuum, due to the difference in phase velocity from the material. After propagating though the region containing gas, there will be a fractional phase shift in the light given by

$$\frac{\Delta\lambda}{\lambda} = \frac{1}{\lambda}\int_0^L (\eta - 1)dz \approx \frac{2\pi\alpha}{\lambda}\int_0^L n_{atomic}\, dz \tag{3.1}$$

where η is the index of refraction, α is the atomic polarizability, and λ is the probe laser wavelength. The last step is an approximation to the Clausius-Mossotti relation which is valid for $\eta - 1 \ll 1$. An important caveat is that the rays must not significantly refract from parallel to the z-axis. If significant refraction does occur, the integral over z must instead be taken over the optical path length for each ray.

To extract the phase information, the laser is interfered with a reference copy of itself which has only gone through vacuum or homogenous gas. The interference pattern between the two lasers reveals the phase shift as a function of position in the beam. The density measurement setup can be simplified by using a wavefront sensor [44]. Since the sensor can directly determine the local spatial phase of the laser, a reference copy of the initial beam is not needed.

The system used here to measure the gas jet density distribution was an interferometer consisting of a 1.2 mW frequency-stabilized helium-neon laser (vacuum wavelength = 632.991 nm), a wavefront sensor (model SID4, Phasics S.A.), two expanding telescopes, a singlet lens to reduce the beam size, and an imaging optic. The setup is shown in Figure 3.2, which is approximately to scale. The first expanding telescope increased the laser beam size to the clear aperture of the vacuum window and the second telescope further enlarged it to larger than the gas jet density distribution. The singlet lens reduced the laser size below the size of the vacuum chamber window and created a virtual image of the gas jet. The final imaging optic, either an f=75 mm planoconvex singlet lens or a multi-lens f=75 mm adjustable-focus television objective, imaged this virtual image onto the wavefront sensor. The wavefront sensor and final imaging optic were mounted on a sliding carriage on a 1 meter rail. The HeNe laser and laser path are shown in red. Light grey areas indicate optical breadboard while the dark grey rectangle near the top represents the vacuum chamber where interferometry was performed. The laser enters and exits the vacuum chamber via thick windows (white rectangles, thickness not to scale). The gas jet target is mounted on an in-vacuum rotation stage mount (purple circle with an "X") after the second laser expander and before the final mirror.

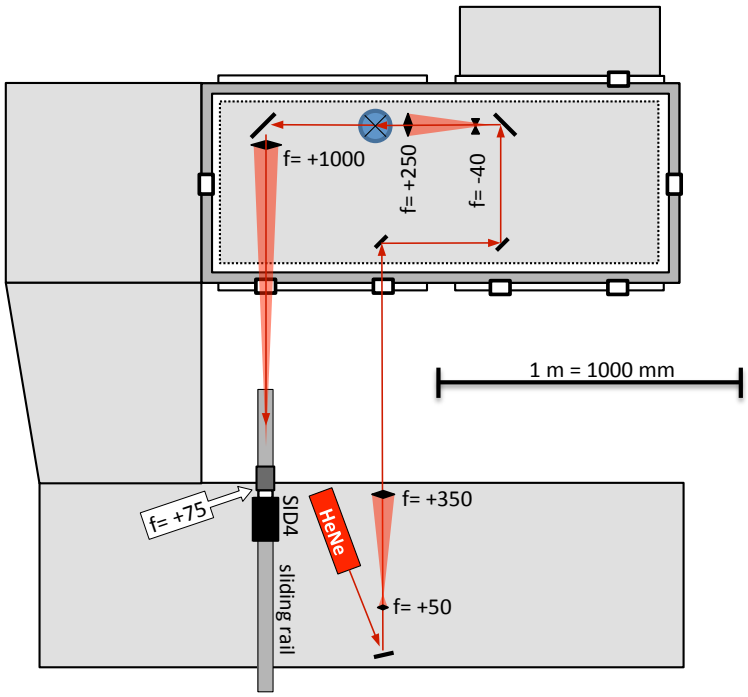

Figure 3.2: Interferometry setup schematic. Scale is approximate.

Operating Voltage and Backing Pressure

The effect of backing pressure on the density profile from the gas jet was studied so a single set of absolute density measurements could be extrapolated to a range of operating pressures. According to inviscid supersonic flow theory [49], the gas density should be linearly proportional to the backing pressure. This linear scaling would allow tomographic measurements done at high pressure (300 psia), maximizing the signal-to-noise ratio of the interferometer, to be scaled to the experimental conditions (55 psia) needed for laser plasma accelerator (LPA) operation.

The peak phase (in fractions of wavelength) measured 10 mm above the gas jet outlet is shown in Figure 3.3(a) as a function of pressure. The fractional phase is related to the integrated density along the gas jet by Eqn. 3.1. The error bars in Figure 3.3(a) and the subsequent plots in this chapter represent the lower and upper quarter percentiles of measurements a particular value. When the jet is operated at 350 V or 400 V, the phase scales linearly with backing pressure, in agreement with inviscid supersonic theory. However, when the operating voltage is reduced to 300 V as in the experiment, a roll-off in the density occurs at high pressures. The integrated density scaling for 300 V operation as a function of backing pressure P in psia is given by

$$\frac{\Delta\lambda}{\lambda_0} = (0.0746 \pm 0.0009) P \exp\left\{-(P/(266 \pm 1))^{3.2\pm0.1}\right\}. \tag{3.2}$$

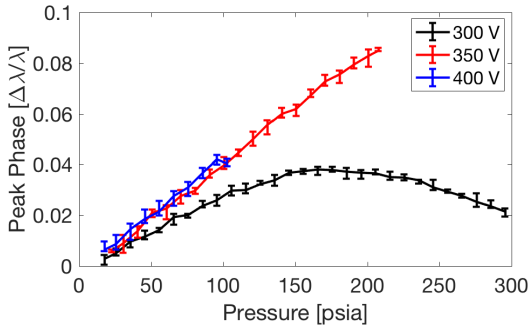

(a) Effect of voltage and pressure at fixed 410 µs.

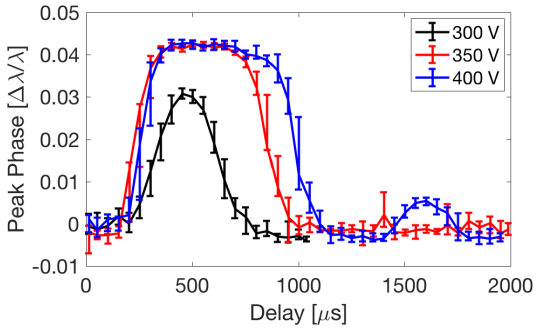

(b) Effect of voltage and timing for fixed 100 psia backing pressure.

Figure 3.3: Effect of voltage on phase (phase $\propto$ integrated gas jet density).

The reason for this nonlinearity can be inferred from Figure 3.3(b), a plot of the peak phase as a function of time between the jet trigger and the phase measurement. For high operating voltages, the jet fully opens as evidenced by a plateau region in the phase time profile. At 300 V operation, the phase never reaches a plateau state, which suggests the jet is never in a steady open state. This will be validated by comparison with an electromechanical model of jet operation. All the measurements in Figure 3.3(a) were done at fixed 410 µs timing, which was the timing delay between the jet trigger and the main laser arrival in the experiment.

Transient Effects

A long-term (minutes) time dependence of the density was discovered while investigating the gas jet scaling. Characterizing this time-dependence is an important component of the density calibration because the gas jet was turned off intermittently during these experiments. The gas output of the jet was found to drop exponentially after the jet begins firing before settling down to a steady state value. The drop in gas output is evident in the integrated phase along the jet's long axis, show in Figure 3.4(a) at both 1 Hz and 0.5 Hz. Along with the gas output, the current drawn by the gas jet shown in Figure 3.4(b) also drops after the jet is first turned on before leveling off. The normalized phase drop when operating the gas jet with 80 psia helium at 1 Hz is well fit by the following exponential function (red curve in Figure 3.4(a)):

$$\frac{\Delta\lambda}{\lambda_0} = (0.835 \pm 0.005) + (0.165 \mp 0.005)e^{-t/(56\pm11\text{ s})}. \tag{3.3}$$

The decay in gas jet density and current is consistent with heating of the actuating solenoid, causing increased electrical resistance and reduced opening displacement. The current drawn by the jet is initially $\sim$ 435 A independent of repetition rate. Evidence in support of this hypothesis is that the jet body temperature shows a slow by measurable

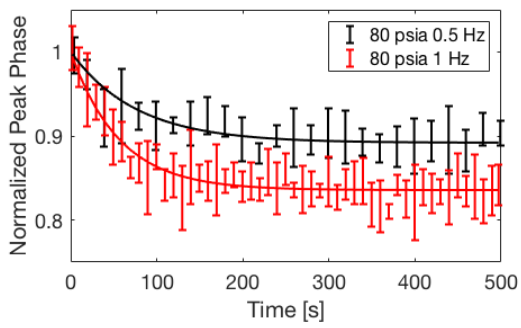

(a) Drop in phase shift, normalized to start at unity, after jet turn on

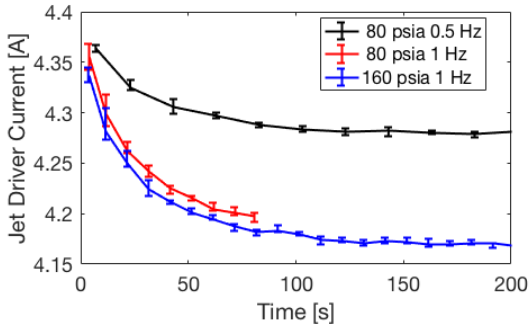

(b) Corresponding drop in driver current

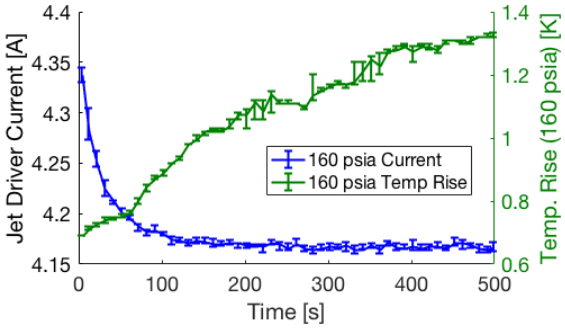

(c) Jet body temperature vs dropping current

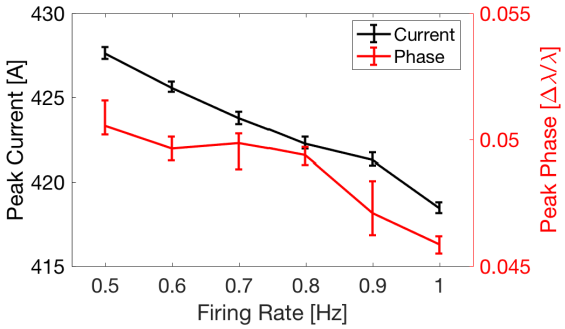

(d) Dependence of plateau current and fractional phase shift on jet repetition rate.

Figure 3.4: Time dependence of the gas jet density/phase after starting jet operation.

increase in temperature as the jet is fired correlated with a drop in current, shown in Figure 3.4(c), and in gas output indicated by measured phase shift. In addition, the current drawn by the gas jet increases with decreasing repetition rate of the gas jet, as in Figure 3.4(d). This can be explained since the cooling rate is fixed by the water flow around the jet but the rate of heat deposition is set by how often the jet is fired.

The time dependence of the jet density after turn on in Eqn. 3.3 can be incorporated into a density calibration provided that it is reproducible. The reproducibility of the jet was studied by looking at the current and integrated phase after pausing the jet's operation for various lengths of time (Figure 3.5). The gas jet was started after initially being off for >10 minutes. After the first 100 measurements, the gas jet's operation was paused for 30 s. After another 100 measurements, its operation was paused for 1 min. Then after each 100 measurements it was paused for an additional minute, with the final pause being 5 min long. After a turn off time of 3 min, the initial current drawn by the jet no longer rises significantly with additional cooling time. The initial phase, which is proportional to gas jet density, does rise with additional cooling time, but based on the approximately linear increase with cooling

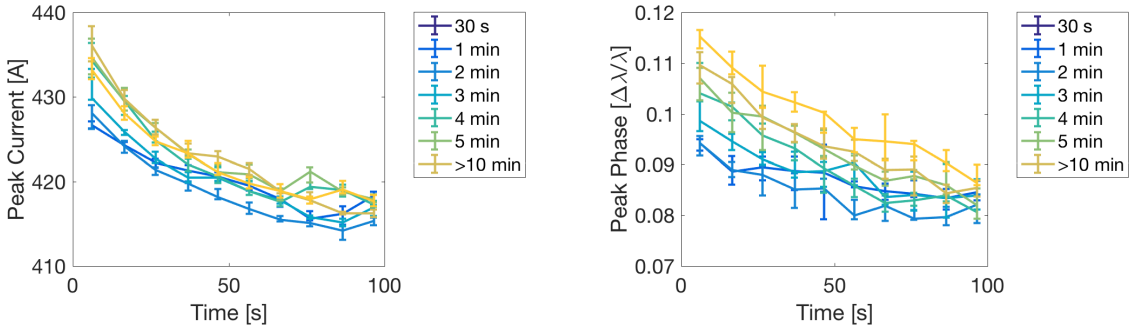

(a) Peak current drawn by gas jet

(b) Phase shift proportional to jet output

Figure 3.5: Recovery of the gas jet density/phase after various length pauses.

time the phase after 6 min of cool down will agree with the steady state measurement, to well the shot-to-shot fluctuations. This means that the jet has cooled to its initial temperature after 6 min.

Explanation of Measured Scalings

An electrical model of gas jet operation was created and used to determine its internal motion. Details of the model are given in Appendix A. The model is able to explain several of the observed gas jet density scalings. In particular, when the jet is operated at 300 V, the phase (which is proportional to the integrated density) measured at a fixed delay scales nonlinearly with backing pressure, as shown in Figure 3.6(a). Based on the electromechanical model, increasing the backing pressure shortens the gas jet opening time, seen in Figure 3.6(b). The decrease in opening time is due to the increased gas force on the plunger. Because the phase measurements in Figure 3.6(a) were all taken at 410 µs after the jet trigger signal, the shortening of the phase time profile appears as a roll off in density at higher backing pressures. It is thus necessary for the experimental density to be characterized at the same voltage, pressure, and relative timing as the experiment, because at 300 V all three factors affect the gas jet's operation.

The time-dependence in the measured integrated phase after initially turning off the jet can also be explained by the model. As the solenoid wire heats up, its resistance increases linearly with the temperature. This results in an almost-linear decrease in the peak current as well as a decrease in the peak phase 10 mm above the jet. The simulated current for a backing pressure of 160 psia of helium is shown in Figure 3.7 as a function of temperature rise. The simulated peak phase 10 mm above the gas jet at a fixed 410 µs delay is also plotted. Comparison with the 160 psia helium plot in Figure 3.4(a) shows that the initial decay in gas output from the jet corresponds to a 23 K temperature rise of the solenoid. The argon plot corresponds to a 53 K temperature rise.

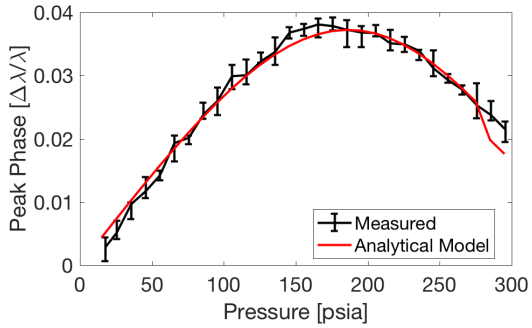

(a) Measured and modeled phase measurement as a function of pressure.

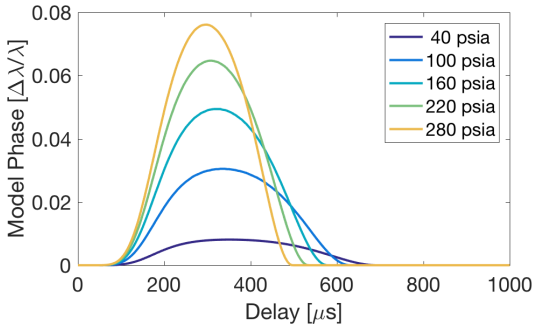

(b) Phase vs timing from model for various pressures.

Figure 3.6: Nonlinear density vs. pressure relationship of the gas jet is reproduced by the jet electromechanical model and explained by a pressure-dependent opening time.

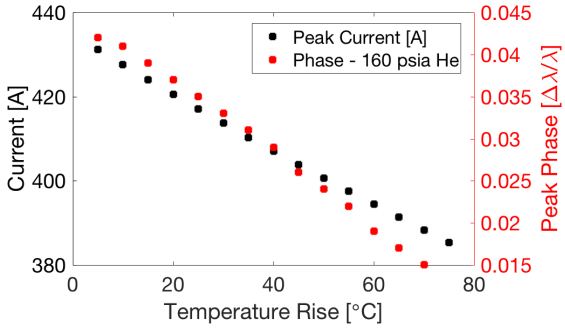

Figure 3.7: Both peak current and fixed-timing phase from jet model decrease with temperature rise of solenoid, which increases solenoid resistance.

3.3 Tomography

The slit jet target is rectangular and so lacks rotational symmetry. As a result, the three dimensional gas profile cannot be determined from any single interferometric measurement. By measuring the integrated density from many angles, it is possible to determine the three dimensional gas density profile without relying on assumptions about symmetry as in an Abel transform.

Tomographic Reconstruction

The technique of determining an arbitrary distribution from integrated measurements (projections) of the distribution is called tomography [50] and is well-studied, particularly for its applications in medical imaging such as MRI and CT diagnostics. A simple example is shown in Figure 3.8(a), where the two dimensional distribution x is integrated along the 90° and 0°

directions to get the projections b_1 and b_2, respectively. The distribution and the projections are related by a matrix:

$$\mathbf{A}\vec{x} = \vec{b} \tag{3.4}$$

where $\vec{x}$ is the columns of the distribution and $\vec{b}$ is the projections, as in Figure 3.8(b). The projection matrix $\mathbf{A}$ integrates the distribution along a number of directions and can be readily calculated by ray tracing. In a tomographic problem, the projections $\vec{b}$ and the projection angles are known, but the distribution $\vec{x}$ is not. Here, the problem is to determine the unknown distribution of gas at each height above the jet outlet from the phase measurements, which are projections of refractive index (see Eqn. 3.1).

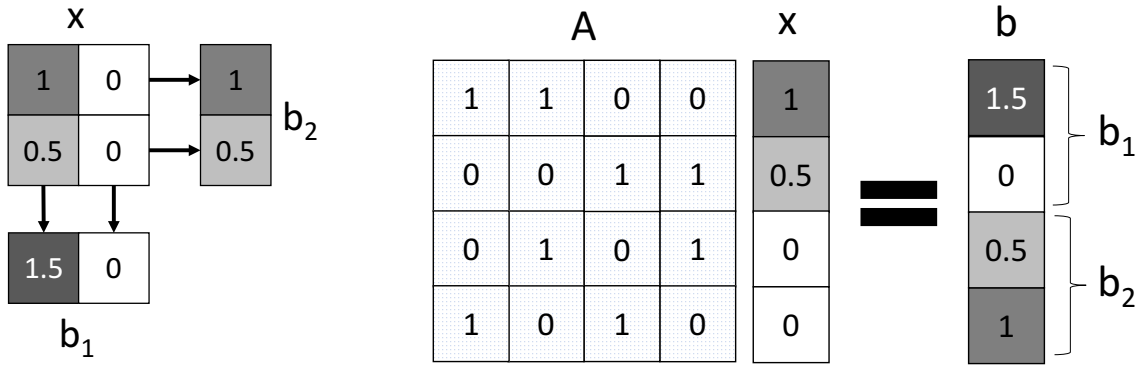

(a) A four pixel distribution projected in two directions.

(b) The matrix representation of the projection operation.

Figure 3.8: Simple example of a distribution, its projections, and their matrix relationship.

Many methods [50, 51] have been developed to reconstruct the unknown solution $\vec{x}$ to the inhomogeneous linear algebra problem: $\mathbf{A}\vec{x} = \vec{b}$. The simplest approach is to invert the projection matrix $\mathbf{A}$. However, an inverse is not guaranteed to exist. In fact, the matrix is only square if the number of projections equals the number of pixels are taken at each height, and if an inverse exists finding $\mathbf{A}^{-1}$ may be computationally difficult. For example, the wavefront sensor used in these measurements has a horizontal resolution of 160 pixels. If 160 projections were measured with this resolution, satisfying the requirement for a square matrix, the sparse matrix $\mathbf{A}$ would be $25,600 \times 25,600$. The various tomographic reconstruction algorithms have the ability to incorporate an arbitrary number of projections, as well as additional advantages such as incorporation of a priori knowledge about the solution and tolerance to noise.

The fundamental scheme for tomographic imaging is filtered back projection [50]. Since the matrix $\mathbf{A} : X \mapsto B$ maps possible distributions (X) to projections (B), its transpose $\mathbf{A}^T : B \mapsto X$ maps projections to distributions, and its action is referred to as "back projection." This corresponds to spreading each projection across the distribution domain along the projection direction. Projection of a known distribution followed by back projection

has the effect of spatially averaging the distribution. In filtered back projection, the projections (phase measurements) are back projected onto the distribution domain, and then a high-pass filter with a windowing function is applied to counteract the spatial averaging effect. This two-step operation results in an approximate solution to the tomographic problem. However, filtered back projection requires many angles (100s-1000s) to accurately recreate the source distribution [50].

More accurate reconstructions can be achieved with less angular resolution by algebraic reconstruction techniques which iteratively improve the reconstructed distribution. These solutions to the tomographic problem consist of repeatedly projecting a hypothesized distribution, comparing those projections with the measured projection data, and back projecting a correction. This many be done for each of the N projection angles iteratively or all the projections simultaneously. One such algorithm is Cimmino's method, where the k^{th} iteration $\vec{x}_k$ is related to the next iteration $\vec{x}_{k+1}$ by

$$\vec{x}_{k+1} = \vec{x}_k + \lambda \mathbf{A}^T \mathbf{M}^{-1} (\vec{b} - \mathbf{A}\vec{x}_k) \tag{3.5}$$

where λ is a forcing parameter and the weight matrix $\mathbf{M} = \vec{a}^T \mathbf{I} \vec{a} / \operatorname{Tr}\{\mathbf{I}\}$. Here, $\mathbf{I}$ is the identity matrix and the elements of $\vec{a}$ are the diagonal elements of $\mathbf{A}^T\mathbf{A}$ (*i.e.*, each element of $\vec{a}$ is the length of the corresponding row vector of $\mathbf{A}$). This algorithm was used for tomographic reconstruction of the gas jet density profile.

Effect of Gas Species

The effect of gas species was investigated because although helium was used in the electron acceleration experiments it has a very low atomic polarizability, which determines the phase shift per atom as in Eqn. 3.1. Argon has $\sim 8\times$ the atomic polarizability of helium and the same ratio of specific heats, $\gamma = c_p/c_v$, which determines the flow properties in isentropic, compressible flow [49]. The tomographic reconstruction of the density 10 mm above the gas jet (the distance of the laser in the LPA experiment) operated with high pressure (310 psia) argon gas at 370 V is shown in Figure 3.9(a). This reconstruction was determined using 166 different projection angles. Additional angles close to the jet axis were excluded from the analysis due to excessive lensing from the gas.

Significant differences were found in gas distribution when using argon as opposed to helium. The reconstructed density profile from the same height above the gas jet when operated with 100 psia helium at 350 V is shown in Figure 3.9(b). Comparing this with the argon reconstruction in Figure 3.9(a), the width of the argon distribution is markedly larger (transverse FWHM $\approx$ 3.7 mm vs. 7.3 mm, resp.). In addition to gas species, the two tomographic reconstructions have different backing pressures and a small difference in voltage. However, the large change in jet width between the helium and argon jets cannot be explained by these latter factors. In Figure 3.10, the full width at half maximum (FWHM) width of the gas jet using helium for various voltages and backing pressures is shown, based on interferometry along the jet axis. The width of the helium jet is independent of voltage

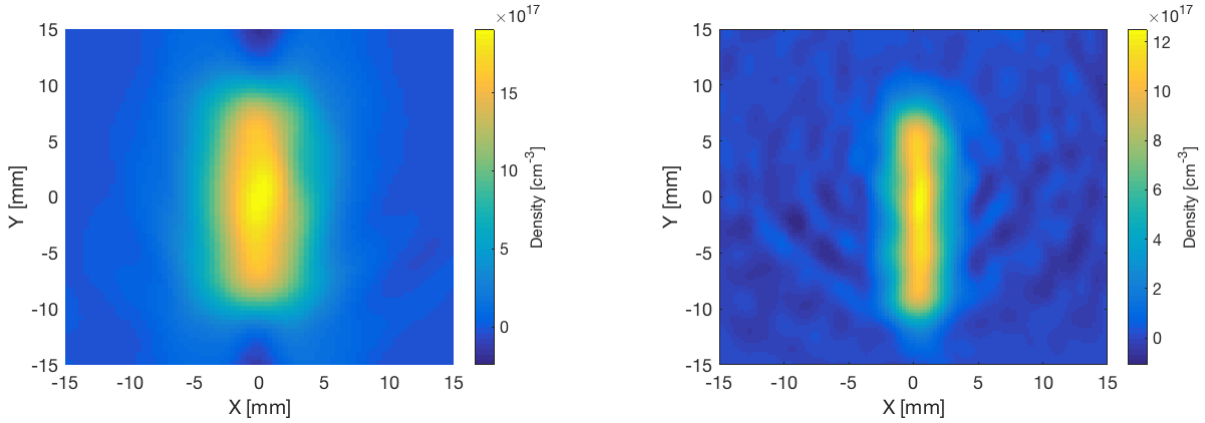

(a) Tomographic reconstruction of the argon atomic density 10 mm above gas jet with a backing pressure of 310 psia operated at 370 V.

(b) Tomographic reconstruction of the helium atomic density 10 mm above gas jet with a backing pressure of 100 psia operated at 350 V.

Figure 3.9: Tomographic reconstruction of argon atomic density and comparison with fit.

in the 350-400 V range and does not change with increasing pressure above $\sim$ 80 psia. The difference in jet performance when backed with argon or helium is possibly due to the formation of a boundary layer at the wall of the expansion section of the jet (highlighted green in Figure 3.1(b)) [52]. Because of this boundary layer, the effective area and opening angle of the expansion section would be reduced depending on the gas viscosity (2.1×10^{-5} Pa s for Ar vs. 1.87×10^{-5} Pa s for He, both at 0°C). For these reasons, the density measurements were performed using helium.

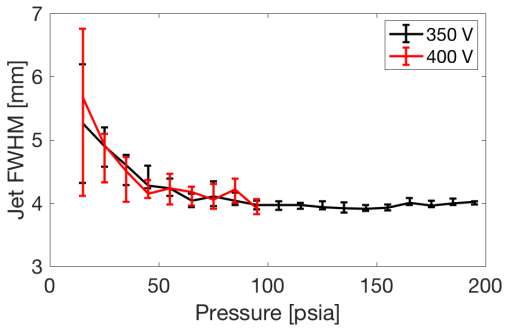

Figure 3.10: Helium gas jet width (FWHM) at 10 mm height from interferometry at 350 V and 400 V is constant above backing pressures of $\sim$ 80 psia

Tomography at Experimental Conditions

Tomographic measurements were taken with helium with the gas jet operating under the same conditions as the experiments. For the experiment, the gas jet was operated at 300 V with a backing pressure of 55 psia and a trigger sent 410 µs before the laser. The laser was fired 10 mm away from the jet outlet so the density at that height is of interest for the LPA experiment. Under these conditions, the phase shift from the helium gas distribution was comparable to the background fluctuations of the interferometry setup (compare Figures 3.11(a) and 3.11(b)).

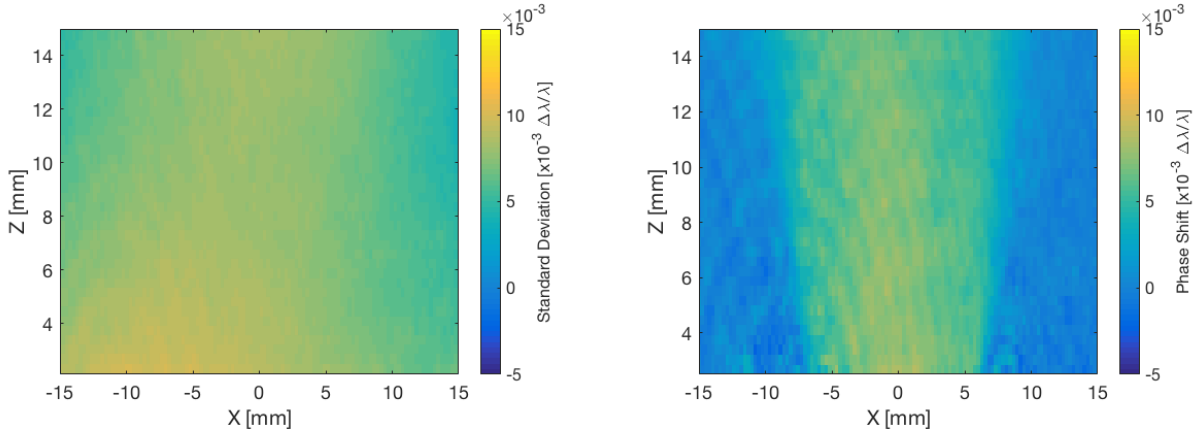

(a) Standard deviation of background fluctuations from 50 images without gas jet firing

(b) Phase shift from jet along short axis (average of 50 measurements) after subtracting background

Figure 3.11: Comparison of signal level to standard deviation of background fluctuations.

Investigation of background fluctuations found that the laser wavefront had a long-term drift as well as shot-to-shot fluctuations, both of which consisted of low-spatial-frequency variation of the laser spatial phase. To address the long-term drift, a set of reference measurements without the jet was taken after each 5 sets of angular measurements of the jet. Each set of reference measurements was averaged to remove shot-to-shot fluctuations and get a single reference wavefront. The reference wavefronts were interpolated pixel-by-pixel to the approximate time of the jet measurements and subtracted, thus removing the long-term trend in laser wavefront drift. The shot-to-shot fluctuations were addressed my two approaches: averaging many measurements at each angle and removing a bicubic background fit to a region outside the jet plume from each measurement. Although 50 measurements were taken at each angle, fluctuations of the background were still present in the averaged wavefront (see Figure 3.11(b)). For this reason, a bicubic background subtraction based on the region outside the jet was also subtracted from each image. This was tested on wavefront measurements without jet and resulted in significantly reduced background without introducing a bias to the background.

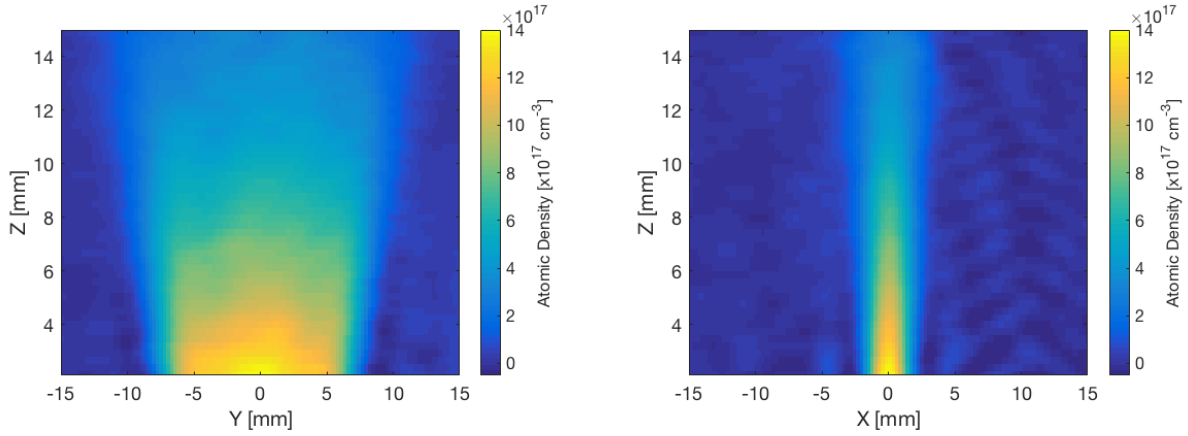

(a) Reconstructed density profile of the gas jet plume along the laser axis

(b) Reconstructed density profile of the gas jet plume transverse to the laser axis

Figure 3.12: Reconstructed helium atomic density profile of the gas jet for a range of heights.

The reconstructed density profile of the laser is shown in Figure 3.12. At each height, the profile is well fit ($R^2 \approx 0.96$-0.99 for the range for heights plotted) with a two dimensional super-Gaussian distribution, defined by

$$n(x,y) = n_0 e^{-\ln(2)\left|\frac{2x}{L_x}\right|^{d_x}} e^{-\ln(2)\left|\frac{2y}{L_y}\right|^{d_y}} \tag{3.6}$$

where n_0 is the plateau atomic density, L_x and L_y are the full widths at half maximum (FWHM) of the distribution in their respective directions, and d_x and d_y are the rank or order of the distribution in each respective direction. The root-mean-square (RMS) of density in the region outside the jet plume in the reconstruction was $\sim 1.3 \times 10^{16}$ cm^{-3}. This is slightly larger than the RMS difference between the reconstruction and the super-Gaussian fit and gives an estimate of the statistical error from the tomographic reconstruction.

3.4 Density Profile along Laser Axis

The physics of the laser-plasma interaction are determined by the density profile along the one dimensional laser axis through the gas jet. Since the three dimensional profile of the gas jet density distribution is well characterized, the one dimensional profile can be determined from the gas jet's relative location and orientation to the laser axis. A detailed discussion of the jet alignment is given in Appendix B. The laser height was 10 ± 0.25mm above the gas jet outlet. The angle of the long axis of the gas jet to the laser axis was determined to be $\theta_{jet,exp} = -0.1^\circ \pm 1.1^\circ$ and the offset in transverse position was $\Delta y = 50 \pm 200$ µm.

The tomographic results together with the jet alignment relative to the laser axis yield the density profile along the laser axis. The density profile along the laser axis was well fit by a super-Gaussian of the form

$$n(z) = n_0 e^{-\ln(2)\left|\frac{2z}{L}\right|^d} \tag{3.7}$$

where n_0 is the plateau atomic density, L is the full width at half maximum (FWHM) of the distribution ,and d is the order of the distribution. The parameters of the one dimensional density profile are given in Table 3.1 together with the uncertainty in each quantity. The source(s) of uncertainty in each quantity are listed in the third column.

Quanitity	Value	Uncertainty	Source
n_0 [cm^{-3}]	5.1×10^{17}	0.45×10^{17}	SC, JA, TR
L [mm]	18.2	1.5	SC, JA
d	6.2	0.2	JA

SC = Spatial Calibration, JA = Jet Alignment,
TR = Tomographic Reconstruction

Table 3.1: Super-Guassian density distribution and associated uncertainties at experimental conditions.

Profile Uncertainty and Transverse Gradients

The tomographic reconstruction at a height of 10 mm above the nozzle is shown in Figure 3.13(a) along with a two dimensional super-Gaussian fit to the distribution, defined by Eqn. 3.6. The same fit was performed at a range of heights above the gas jet, and the resulting fit amplitudes $n_0(z)$ are plotted in Figure 3.13(b) along with a $1/(z - z_0)^2$ fit, which is the asymptotic solution to a supersonic two dimensional jet at distances much larger than the jet throat. As noted, the uncertainty in the reconstruction estimated to be $\sim 1.3 \times 10^{16}$ cm^{-3}. The uncertainty in height coupled with this fall-off in density as a function of height gave an additional 1.3×10^{16} cm^{-3} uncertainty in the density. There is a 5% uncertainty in the spatial calibration of the wavefront sensor. Together, these three sources of uncertainty give the quoted error in Table 3.1.

The density gradient along the laser axis was also determined based on the tomographic results and the jet alignment. The gradient along the direction of gas flow was estimated in Figure 3.14 based on the results in Figure 3.13(b). The red curve indicates the derivative of the fit in the latter. Based on the jet alignment, the transverse gradient in density along the laser profile shown in Figure 3.14(a) along with a shaded uncertainty region based on the error quoted in determining the jet angle and transverse position relative to the laser axis..

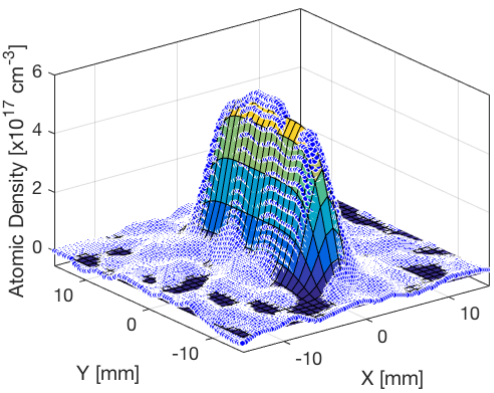

(a) Tomographic reconstructed atomic density profile (points) and super-Gaussian fit (surface) of the experimental conditions.

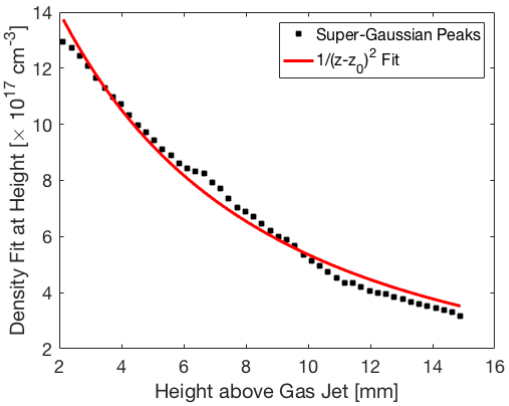

(b) Super-Gaussian fit results at each height above gas jet and a $1/r^2$ fit vs. height.

Figure 3.13: Tomographic reconstruction at the laser height and plateau atomic density, based on super-Gaussian fits, at a range of heights above the gas jet.

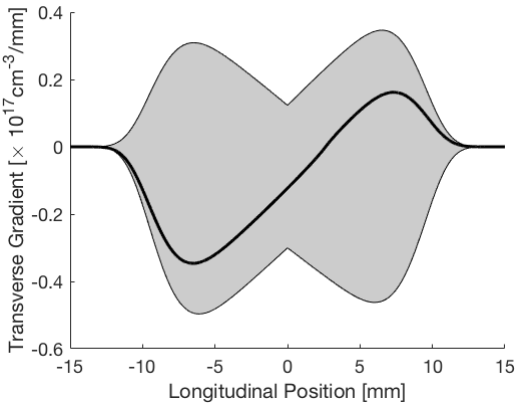

(a) Transverse density gradient (normal to the direction of gas flow) along the laser with uncertainty.

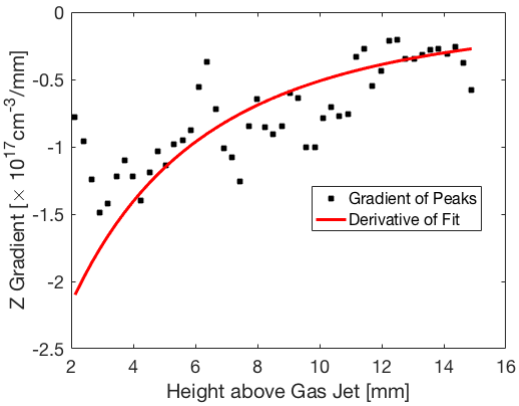

(b) Density gradient in direction of gas flow and derivative of fit from Figure 3.13(b)

Figure 3.14: Density gradients transverse to laser propagation based on jet orientation and tomography results.

3.5 Concluding Remarks

The density profile along the laser axis determined in this chapter together with the laser measurements presented in Chapter 2 is sufficient to characterize the operation of the BELLA LPA for these experiments. These will be used as inputs for three-dimensional simulations, presented in Chapter 6, used to explain the dependence of measured laser and electron properties on laser pulse front tilt. Verification of the density profile determined here will be presented in Chapter 5 using measurements of the laser spectral modulation and simulations of the laser-plasma interaction.

Chapter 4

Laser-Plasma Interactions

The components of the BELLA laser plasma accelerator (LPA) were detailed in the previous two chapters, and here the theory of their interaction is presented. This theory is extended by deriving an expression to predict the effect of pulse front tilt on a Gaussian laser pulse, which is validated by comparison to two-dimensional simulations. A complimentary model of electron steering and deflection is also developed. This chapter provides the theoretical framework for explaining the experiments presented in Chapter 5 and Chapter 6.

A laser plasma accelerator (LPA) consists of a high-intensity laser pulse traveling through a plasma with a pulse length close to the plasma wavelength [7]. The laser displaces the electrons in its path via the ponderomotive force (the gradient in radiation pressure), and this results in a wave of displaced electrons behind the laser pulse (the plasma wake). The wake has a large electric field (10-100 GV m^{-1}) which can accelerate particles. To resonantly excite electron motion, a driver with a similar timescale to the plasma period (the reciprocal of the plasma frequency) is needed [8]. For typical high-density laboratory plasmas with densities corresponding to a few percent of an atmosphere this is on the order of 10-100 fs. For this reason, LPA physics is closely connected with the science of ultrafast (ps to fs) lasers.

4.1 Plasma Formation and Blue Shifting

In these experiments and in typical LPA schemes which do not utilize preformed plasma channels, a compressed laser pulse is focused through a neutral gas target with a peak focal intensity much higher than the ionization threshold, I_{thresh}, of the target gas [8]. The laser intensities relevant for laser plasma acceleration ($\sim 10^{18}$ W/cm^2) are several orders of magnitude higher than the threshold intensity to ionize hydrogen or helium ($I_{thresh} \approx 2.8 \times 10^{14}$ W/cm^2 for H_2 [53]). The ionization threshold can be defined as the intensity where the ionization rate, such as given by the ADK (Ammosov-Delone-Krainov) tunneling ionization model [54], goes from exponential to linear as a function of intensity. LPA simulations therefore typically neglect the plasma formation since the front edge of the laser ionizes the neutral gas and the bulk of the laser propagates through a fully ionized

plasma. At lower intensities, however, ionization has important effects. Variation in plasma density transverse to the laser propagation can lead to ionization defocusing and longitudinal variation can modulate the laser spectrum. The output spectrum of an ionizing laser pusle is thus a complex function of the input laser pulse's temporal structure (envelope and chirp), its focusing ($I_{peak}(z)$), and the density profile of the ionizing gas [55, 56].

Ionization causes a locally varying index of refraction within the pulse, which leads to spectral blue shifting. Because the ionization occurs within the laser, the front of the pulse travels through a lower plasma density than the rear of the pulse (Figure 4.1), and the phase velocity increases (and the index of refraction η decreases) toward the rear. In general, a gradient in phase velocity in the co-moving frame of a laser pulse causes a shift in frequency proportional to the gradient. This results from phase fronts with different speeds moving closer together or further apart, depending on the sign of the gradient, as the pulse propagates. In an unmagnetized, underdense plasma, the phase front speed is

$$v_{phase} = c/\eta = c\left(1 - \omega_p^2/\omega^2\right)^{-1/2} \tag{4.1}$$

where η is the index of refraction, ω is the laser's instantaneous frequency and $\omega_p \propto n_{plasma}^{1/2}$ is the plasma frequency which is a function of plasma density, n_{plasma}. The plasma density, and therefore plasma phase velocity, increases in the ionizing region from unionized gas in the front of the pulse ($v_{phase} \sim c$) to the final ionization fraction in the rear ($v_{phase} > c$), causing the phase fronts to compress and shifting the spectrum in that region toward shorter wavelengths (i.e. blue shifting). The gradient in the plasma density inside an ionizing laser leads to a change in instantaneous frequency of

$$\frac{\partial \omega}{\partial z} = -\frac{\omega_p}{\omega}\frac{\partial \omega_p}{\partial \xi} \tag{4.2}$$

at position $\xi = z - ct$ in the pulse [8, 57].

If the instantaneous frequency of the laser varies with position as a result of spectral phase, the location of the ionization front is recorded in the blue shifted spectrum since the shifted region of the spectrum would correspond to a longitudinal position. The spectral shift of an ionizing laser thus contains information about the instantaneous frequency at the ionization front, which is related to the complex spectrum by Eqns. 2.1 and 2.7. Referring to Eqn. 4.2, the magnitude of the spectral shift is proportional to the gradient in plasma density, so a higher density target will give a larger spectral shift. Knowledge of high-order spectral phase is of interest because it limits laser pulse compression and is the cause of temporal asymmetry and nonlinear chirp in the compressed pulse, which affect electron acceleration [8, 58]. Even in a CPA laser that is optimally compressed, the laser pulse typically has residual nonlinear chirp due to high-order dispersion in the amplifier and transport optics.

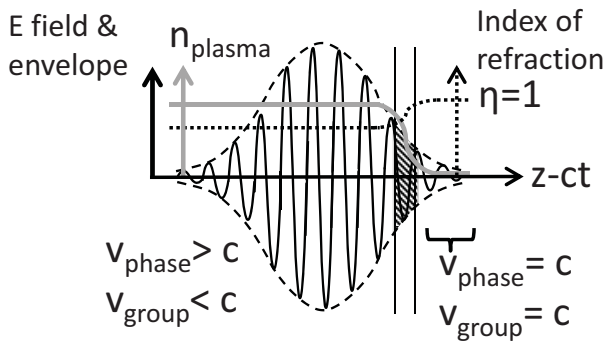

Figure 4.1: Schematic of an ionizing pulse propagating through an initially unionized gas. The shading indicates the frequency blue shifted section of the pulse where most ionization occurs. Propagation is from left to right.

4.2 Laser-Driven Plasma Waves

The Ponderomotive Force

The force of the laser field a single electron is given by the Lorentz force equation

$$\frac{\mathrm{d}\vec{p}}{\mathrm{d}t} = -e[\vec{E} + (\vec{\beta} \times \vec{B})] \tag{4.3}$$

where $\vec{\beta} = \vec{v}/c$ is the normalized velocity of the electron, e is the magnitude of the electron's charge, and $\vec{p} = \gamma m \vec{v}$ is the electron momentum in terms of its mass m, velocity $\vec{v}$, and relativistic gamma factor $\gamma = 1/\sqrt{1-\beta^2}$. The laser electric field $\vec{E}$ and magnetic field $\vec{B}$ can be described in terms of the laser vector potential $\vec{A}$ as

$$\vec{E} = -\nabla\varphi - \frac{\partial \vec{A}}{\partial ct} \qquad \vec{B} = \nabla \times \vec{A} \tag{4.4}$$

The potentials are not uniquely determined so an additional constraint (the gauge condition) is required. The Coulomb gauge is defined by

$$\nabla \cdot \vec{A} = 0 \tag{4.5}$$

and will be used in this text. It is assumed here and throughout that the laser is linearly polarized so $\vec{E} = E\hat{x}$ since the BELLA laser used in these experiments has a fixed linear polarization. It is convenient to normalize the vector potential as

$$\vec{a} \equiv \frac{e\vec{A}}{m_e c^2} \tag{4.6}$$

and normalize the electron's momentum as

$$\vec{u} \equiv \frac{\vec{p}}{m_e c} = \gamma\vec{\beta}. \tag{4.7}$$

With these definitions, the equation of motion for an electron in a laser field can be written [8] as

$$\frac{\mathrm{d}\vec{u}}{\mathrm{d}ct} = \frac{\partial\vec{a}}{\partial ct} - \frac{1}{\gamma}\,\vec{u}\times(\nabla\times\vec{a}). \tag{4.8}$$

To leading order in velocity with $u \ll 1$, this is solved by $\vec{u} = \vec{a}$, which is oscillation in the polarization direction called quiver motion [59]. Allowing a small perturbation in momentum, $\vec{u} = \vec{a} + \delta\vec{u}$ gives

$$\frac{\partial}{\partial ct}\delta\vec{u} = -\frac{1}{\gamma}\,[(\vec{a}\cdot\nabla)\vec{a} + \vec{a}\times(\nabla\times\vec{a})] = -\frac{1}{\gamma}\nabla(a^2/2) \tag{4.9}$$

which is a force (the "ponderomotive" force) directed away from the gradient of the intensity $I \propto a^2$ [7]. This perturbative expansion is only valid if $u \approx a \ll 1$.

The one-dimensional ponderomotive force for $a \gtrsim 1$ can be derived by considering the effect of a linearly-polarized plane wave (*i.e.*, $\vec{a} = a(z-ct)\hat{x}$) [60]. If the electron starts from rest, then its normalized momentum at any point is $\vec{u} = u_x\hat{x} + u_z\hat{z}$, since the geometry is symmetric with respect to y. With this momentum and driving force, Eqn. 4.8 is

$$\frac{\mathrm{d}\vec{u}}{\mathrm{d}ct} = \frac{\partial a}{\partial ct}\hat{x} - \frac{1}{\gamma}\vec{u}\times(\nabla\times\vec{a}) = \hat{x}(\frac{\partial a}{\partial ct} + \frac{1}{\gamma}u_z\frac{\partial a}{\partial z}) + \hat{z}(-\frac{1}{\gamma}u_x\frac{\partial a}{\partial z}). \tag{4.10}$$

The components of Eqn. 4.10 are

$$\begin{aligned}\frac{\mathrm{d}u_x}{\mathrm{d}ct} &= \frac{\partial a}{\partial ct} + \frac{u_z}{\gamma}\frac{\partial a}{\partial z} = \frac{\partial a}{\partial ct} + \beta_z\frac{\partial a}{\partial z} = \frac{\mathrm{d}a}{\mathrm{d}ct}\\ \frac{\mathrm{d}u_z}{\mathrm{d}ct} &= -\frac{u_x}{\gamma}\frac{\partial a}{\partial z}\end{aligned} \tag{4.11}$$

where $\beta_z = \partial z/\partial ct$. The equation for the transverse electron motion for an electron starting from rest is solved by $u_x = a(z-ct)$ which again shows the transverse motion of the electron is the quiver motion (*i.e.*, linear motion in the polarization direction).

The work done on an electron by an electromagnetic field is

$$\mathcal{E} - \mathcal{E}_0 = \gamma mc^2 - \gamma_0 mc^2 = -\int e\vec{E}\cdot d\vec{r} = -\int e\vec{E}\cdot\vec{v}dt \tag{4.12}$$

where $\mathcal{E}_0 = \gamma_0 mc^2$ is the initial energy of the electron and $\vec{r}$ is its position. Taking the time derivative of this gives the energy evolution equation

$$\frac{\mathrm{d}\gamma}{\mathrm{d}ct} = -\frac{e}{mc^2}\frac{\vec{v}}{c}\cdot\vec{E} = -\frac{\vec{u}}{\gamma}\cdot\frac{\partial\vec{a}}{\partial ct} \tag{4.13}$$

which is true without assumptions on the laser driver. For the plane wave driver then

$$\frac{\mathrm{d}u_z}{\mathrm{d}ct} = -\frac{\mathrm{d}\gamma}{\mathrm{d}ct} = \frac{u_x}{\gamma}\frac{\partial a}{\partial ct} = -\frac{a}{\gamma}\frac{\partial a}{\partial z} = -\frac{1}{\gamma}\frac{\partial}{\partial z}\frac{a^2}{2} \tag{4.14}$$

using the solution $u_x = a(z - ct)$ and the implicit assumption that a does not evolve (*i.e.*, of $a = a(z - ct)$ so $\partial a/\partial z = -\partial a/\partial\, ct$). This is the same ponderomotive force from Eqn. 4.9 but with no perturbative expansion or assumptions on the magnitude of a.

Plasma Motion

A plasma consists of ions and electrons which interact individually by collisions and collectively by the electromagnetic force [61]. It is useful to describe the ions and electrons as two fluids with independent intrinsic properties such as number density and temperature Although they are interacting, in many situations the coupling is slow compared to the phenomena of interest. For example, in common fluorescent lightbulbs the electron temperature is significantly higher than the ion temperature, because the electrical and optical processes all occur on much faster timescales than those on which the ions are capable of reacting [62].

The electrons can be displaced from the ions and the electrostatic force between them will pull the two back together since they are oppositely charged. The ion motion in restoring electrostatic equilibrium can typically be neglected because $m_{electron}/m_{ion} \lesssim 1/2000$. Ion motion becomes important if a strong magnetic field is present or the timescale of the separating force is much longer than the characteristic time of the electron motion. The movement of the electrons to restore equilibrium has a characteristic frequency, the plasma frequency, given by [8, 63]

$$\omega_p = 2\pi f_p = \sqrt{\frac{4\pi n_e e^2}{m_e}} \approx 5.64 \times 10^4 \text{ s}^{-1}\sqrt{n_e} \tag{4.15}$$

where n_e is the electron number density in cm^{-3}, e is the fundamental charge (4.8×10^{-10} esu), and m_e is the electron mass (9.11×10^{-28} g). This is the dispersion relation for plasma waves (Langmuir waves) in a cold ($T \sim 0$), non-magnetized plasma: $\omega = \omega_p$. Because they oscillate independently, any phase relationship between neighboring oscillating fluid elements is set by the driving force behind their oscillation. This means that the wave does not propagate ($v_{group} \equiv d\omega/dk = 0$ since there is no k-dependence). The phase velocity of the plasma wave is set by the group velocity of the driving force. For a laser-driven plasma wave, this is the laser group velocity $v_{g,laser} \approx c$ so it is possible to define a plasma wavelength $\lambda_p = 2\pi v_{g,laser}/\omega_p \approx 2\pi c/\omega_p$.

The single electron motion results can be extended to the collective motion of the plasma electrons by modeling a fluid volume of fixed infinitesimal size as a single particle [64]. However, unlike a single electron, the mass and charge of the fluid volume can change because individual electrons can enter and exit. In this description, the electrons are treated as a

continuous fluid and the ions are treated as a fixed uniform background. The change in the number of particles in the fluid volume is given by the continuity equation

$$\frac{\mathrm{D}n}{\mathrm{D}t} = -n\nabla \cdot \vec{v} \tag{4.16}$$

where n is the number density of electrons in the fluid volume and

$$\frac{\mathrm{D}}{\mathrm{D}t} \equiv \frac{\partial}{\partial t} + (\vec{v} \cdot \nabla) \tag{4.17}$$

is the total (or convective) derivative. The distinction between the total derivative and the single particle full time derivative is that the velocity $\vec{v}$ is now that of the electron fluid in the fluid volume, which can enter or leave the infinitesimal volume element. The equation of motion or momentum equation is

$$mn\frac{\mathrm{D}\vec{v}}{\mathrm{D}t} = \vec{f} - \nabla p \tag{4.18}$$

where $\vec{f}$ is an externally applied force per unit volume, p is the fluid pressure, and n is the number density of particles with mass m. In the context of modeling the fluid element as a single particle, the term ∇p represents the forces from adjacent elements (*i.e.*, internal fluid forces). This set of equations is closed when taken together with an equation of state. For fully ionized plasmas such as this experiment, the electrons behave like an ideal gas so the appropriate equation of state is

$$p = nk_B T. \tag{4.19}$$

In the cold fluid approximation, $T \sim 0$ so the pressure term in the momentum equation can be dropped. This is appropriate when the applied force $\vec{f} \gg \nabla p$ the gradient in pressure from local changes in density and/or temperature, as is the case with any plasma wave driven to appreciable amplitude.

Linear Plasma Waves

If the laser field amplitude satisfies $a \ll 1$ then the density and velocity fields will remain close to their initial values like $n = n_0 + \delta n$ and $\vec{v} = 0 + \vec{\delta v}$ assuming the plasma is initially at rest ($\vec{v_0} = 0$). Keeping only first order terms, the equations of motion become

$$\frac{\mathrm{D}\delta n}{\mathrm{D}t} = \frac{\partial \delta n}{\partial t} = -n_0 \nabla \cdot \vec{\delta v} \tag{4.20}$$

$$mn_0 \frac{\mathrm{D}\vec{\delta v}}{\mathrm{D}t} = mn_0 \frac{\partial \vec{\delta v}}{\partial t} = \vec{f} \tag{4.21}$$

The force under consideration is the Lorentz force so Eqn. 4.21 is the same as Eqn. 4.3 which means its solution is $\vec{\delta v} = c\vec{a}$ to first order in a. To get the density it is helpful to rearrange

Eqns. 4.20 and 4.21 into

$$\frac{1}{c^2}\frac{\partial^2}{\partial t^2}\delta n = -\frac{1}{mc^2}\nabla\cdot\vec{f} = \frac{en_0}{mc^2}\nabla\cdot\left(\vec{E}+\frac{\vec{\delta v}}{c}\times\vec{B}\right). \tag{4.22}$$

The first term is

$$\frac{en_0}{mc^2}\nabla\cdot\vec{E} = -\omega_p^2\delta n/c^2$$

by application of Poisson's equation $\nabla\cdot\vec{E} = -4\pi e(n-n_0) = -4\pi e\delta n$. The second term can be rewritten using the first-order result $\vec{\delta v} = c\vec{a}$ as

$$\begin{aligned}\frac{en_0}{mc^2}\nabla\cdot\frac{\vec{\delta v}}{c}\times\vec{B} =& n_0\nabla\cdot[\vec{a}\times(\nabla\times\vec{a})]\\ =& n_0\nabla\cdot\left[\nabla a^2/2 - (\vec{a}\cdot\nabla)\vec{a}\right]\\ =& n_0\nabla^2 a^2/2\end{aligned} \tag{4.23}$$

since $\nabla\cdot((\vec{a}\cdot\nabla)\vec{a}) = 0$ because of the gauge condition $\nabla\cdot\vec{A} = 0$. Thus Eqn. 4.22 is

$$\left(\frac{\partial^2}{\partial t^2}+\omega_p^2\right)\frac{\delta n}{n_0} = c^2\nabla^2 a^2/2. \tag{4.24}$$

The vector potential has a fast oscillation and a slower envelope. Writing this as $a = \bar{a}e^{i\omega t}$ with ω the laser frequency, Eqn. 4.24 can be averaged over a cycle of the fast oscillation to yield

$$\left(\frac{\partial^2}{\partial t^2}+\omega_p^2\right)\frac{\delta n}{n_0} = c^2\nabla^2\bar{a}^2/4 \tag{4.25}$$

which is solved by

$$\frac{\delta n_e}{n_0} = \int_{-\infty}^{t}\omega_p dt'\sin[\omega_p(t-t')]\frac{1}{k_p^2}\nabla^2\bar{a}^2/4 \tag{4.26}$$

Poisson's equation for the electrostatic potential [65] associated with the wake is

$$\nabla^2\Phi = -\nabla\cdot\vec{E} = 4\pi e\delta n \tag{4.27}$$

or in normalized units with $\phi = e\Phi/m_e c^2$

$$\frac{1}{k_p^2}\nabla^2\phi = -\frac{1}{k_p}\nabla\cdot\vec{E}/E_0 = \frac{\delta n}{n_0} \tag{4.28}$$

where $E_0 = m_e c\omega_p/e$ is the cold wave-breaking field limit [7, 8] which is the electric field strength if $\delta n/n_0 = 1$ in the linear approximation. Plugging this result into Eqn. 4.26 and integrating with the boundary condition that the potential goes to zero very far away gives the plasma potential

$$\phi = \int_{-\infty}^{t}\omega_p dt'\sin[\omega_p(t-t')]\,\bar{a}^2/4. \tag{4.29}$$

and the electric field associated with this wake which is used to accelerate particles

$$E/E_0 = -\frac{1}{k_p}\nabla\phi = -\int_{-\infty}^{t} \omega_p dt' \sin[\omega_p(t-t')]\frac{1}{k_p}\nabla\bar{a}^2/4. \tag{4.30}$$

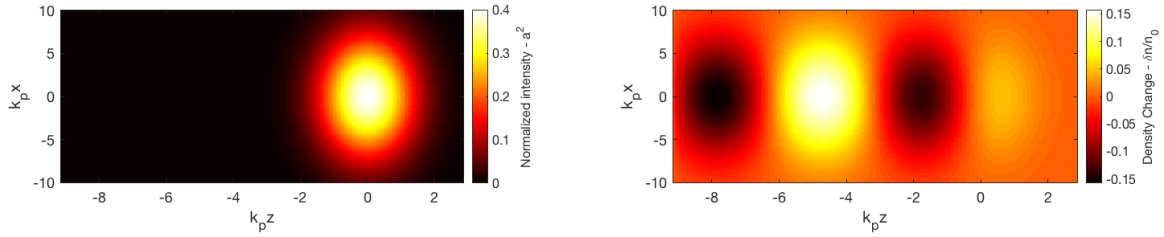

(a) Intensity of a right-propagating laser pulse (b) Density perturbation (laser wake)

Figure 4.2: Laser intensity and associated wake for $a_0^2 = 0.4$ and $k_p L = 2$

The solutions to these equations are a longitudinally sinusoidal plasma potential, electric field, and density perturbation provided the spot size of the laser satisfies $k_p w_0 \gg 1$ so it is large compared to the length scale of the plasma [59]. If this condition is satisfied the wake amplitude depends only on the longitudinal profile of a and wake radial dependence is proportional to $\bar{a}^2$. The solutions for a Gaussian pulse with $1/e^2$ pulse length $L = 2/k_p$ and spot size $w_0 = 5L$ are plotted in Figure 4.2 in normalized coordinates. The normalized intensity of the right-moving pulse (Figure 4.2(a)) creates a density wave in its wake (Figure 4.2(b)).

4.3 Laser Guiding from Plasma Interaction

Linear Regime Self-Focusing

The index of refraction of a plasma [60]

$$\eta = \frac{\omega}{ck} = (1 - \omega_p^2/\omega^2)^{-1/2} \approx 1 - \frac{\omega_p^2}{2\omega^2} \tag{4.31}$$

follows immediately from the dispersion relation for light in a cold unmagnetized plasma $\omega^2 = \omega_p^2 + c^2k^2$ [64]. The approximation is valid so long as $\omega \gg \omega_p$. However, the factor ω_p depends on the electron mass so if the quiver motion of the electrons in the light field becomes relativistic a correction is needed

$$\eta = 1 - \frac{1}{2\gamma}\frac{\omega_p^2}{\omega^2}. \tag{4.32}$$

The factors γ and ω_p in this equation can both lead to self-focusing of the laser pulse [8]. The laser intensity is at maximum on-axis for a pulse with a typical Gaussian or Bessel radial

profile so the factor $1/\gamma$ is minimum there. The laser also creates a plasma wake given by Eqn. 4.26 for $a \ll 1$ whose amplitude varies as $\bar{a}^2$, so it too leads to a minimum on axis.

Assuming $a \ll 1$ and so the local electron density n is close to n_0, Eqn. 4.32 can be rewritten [8, 60] to first order in envelope $\bar{a}$ and wake plasma density n as

$$\eta \approx 1 - \frac{\omega_{p,0}^2}{2\omega^2}\left(1 - \frac{\bar{a}^2}{4} + \frac{n}{n_0}\right). \tag{4.33}$$

The term that depends on a comes from the factor $1/\gamma \approx 1/\gamma_\perp \approx 1 - \bar{a}^2/4$ where $\gamma_\perp$ is the relativistic factor of the quiver motion alone.

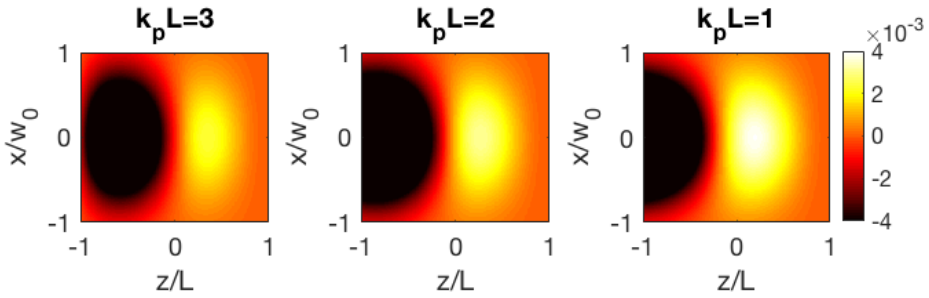

Figure 4.3: Comparison of the normalized wake density change ($\delta n/n_0$) inside the pulse for different values of k_pL.

Assuming the laser transverse profile is a Gaussian, Bessel function, or some other function that is peaked on axis, then the term $\bar{a}^2/4$ will be maximum and index of refraction will be minimum on axis. A radially rising index of refraction corresponds to focusing, and it can be shown [66] that above a critical power this focusing effect will be stronger than diffraction. The critical power is given by

$$P_c = 2c(m_e c^2/e)^2(\omega/\omega_p)^2 \approx 17.4\,\mathrm{GW}(\omega/\omega_p)^2. \tag{4.34}$$

If $P \lesssim P_c$ the laser diffracts with an effectively longer Rayleigh length Z_R but if $P > P_c$ the pulse with continue to focus until other nonlinearities limit its collapse.

However, this result is limited to laser pulses with lengths $L > \lambda_p$. The reason can be seen in (Figure 4.3) which plots normalized wake density inside the pulse. As the pulse length is shortened relative to the plasma length scale $1/k_p$ while keeping a_0 fixed, the density becomes more and more strongly peaked on axis. This means the term $n/n_0 = 1 + \delta n/n_0$ in Eqn. 4.33 becomes increasingly defocusing as the pulse is shortened.

Bubble Regime Self-Focusing

If the ponderomotive force on the plasma is sufficiently strong, all of the electrons behind the laser can be pushed aside by the laser pulse resulting in an empty bubble of electron

density behind the laser pulse [8, 67]. This regime of LPA operation is called the "bubble" or "blow out" regime. The wake amplitude does not rise linearly with intensity a_0^2 and is not sinusoidal as a function of longitudinal position. Eqn. 4.26 already suggests this since an arbitrarily large a_0 would result in a sinusoid solution with amplitude $\delta n/n_0 > 1$ (*i.e.*, the density became negative at the trough of the laser wake, which is nonphysical). The condition for bubble formation [8, 67] with a linearly polarized laser is

$$\frac{k_p w_0}{2} \lesssim \frac{a_0}{(1+a_0^2/2)^{1/4}} \approx \begin{cases} \sqrt{a_0} & a_0 \gg 1 \\ a_0 & a_0 < 1 \end{cases} \tag{4.35}$$

Because the ions remain fixed on the time scale of electron oscillations, the bubble is filled with uniform positive charge. The solution to this electrostatic problem is an axial electric field that is linear with z and zero at the bubble center as well as a focusing field that is linear with distance from the laser propagation axis [67, 68].

The large transverse density gradient at the front of the bubble causes a focusing force from the n/n_0 term in Eqn. 4.33, and if the laser intensity satisfies $k_p w_0 \approx 2\sqrt{a_0}$ and $a_0 \gtrsim 2$ [69] this focusing force balances out diffraction for most of the laser pulse and can keep the laser at high intensity for an extended propagation distance. The transverse and longitudinal size of the bubble are then given approximately by $k_p R_b \approx k_p w_0 \approx 2\sqrt{a_0}$ [69]. Extensive simulations [70] of a laser satisfying $k_p w_0 \approx 2\sqrt{a_0}$ show the size and shape of the bubble actually have a weak linear dependence on a_0.

Steering from Pulse Front Tilt

If a laser has pulse front tilt, the plasma wake it forms will be asymmetrical and so the self-channeling effect will both focus and steer the laser. Each part of the pulse will be steered by the local gradient in plasma density, so the steering of the pulse as a whole is the intensity-weighted average of the the ray deflection formula [71]

$$\frac{\mathrm{d}\Theta}{\mathrm{d}z} = \frac{\partial \eta}{\partial x} \tag{4.36}$$

over the pulse volume. Here, Θ is the angle of the propagation direction of a small volume of the laser pulse in the xz-plane. The ray deflection formula can be applied because the length scale of the wake $\lambda_p \gg \lambda$ the wavelength of the laser. To describe the laser and wake, it is useful to define normalized variables

$$\begin{aligned} \nu &= \sqrt{2}x/W \qquad & \mu &= \sqrt{2}z/L \\ \varrho &= \sqrt{2}y/W \qquad & q &= pcW/L \end{aligned}$$

and the co-moving variable

$$\xi = z - c(t + px).$$

Here it is assumed that the group velocity of the pulse is $v_g \approx c$. The normalized laser vector potential of a Gaussian with pulse front tilt p is

$$a(x,\xi) = \bar{a}(x,\xi)\cos(k_0(z-ct)+\theta(x,z)). \tag{4.37}$$

with the slowly varying envelope

$$\bar{a}(x,\xi) = a_0 e^{-\frac{x^2+y^2}{W^2}} e^{-\frac{\xi^2}{L^2}} = a_0 e^{-\nu^2/2} e^{-(\mu-q\nu)^2/2}. \tag{4.38}$$

At fixed time $t = 0$

$$\mu - q\nu = \frac{\sqrt{2}z}{L} - \frac{pcW}{L}\frac{\sqrt{2}x}{W} = \frac{\sqrt{2}\xi}{L}$$

Eqn. 4.29 for the normalized plasma potential can be rewritten as

$$\begin{aligned}\phi =& \frac{\omega_p}{4}\int_{-\infty}^{t} dt' \sin[\omega_p(t-t')]\bar{a}(x,\xi')^2 \\ =& \frac{-k_p}{4}\int_{\xi}^{\infty} d\xi' \ \sin[k_p(\xi-\xi')]\bar{a}(x,\xi')^2.\end{aligned} \tag{4.39}$$

The plasma wavenumber is defined as $k_p = \omega_p/c = 2\pi/\lambda_p$. The normalized plasma wake density is related to this by

$$\frac{n}{n_0} = 1 + \frac{1}{k_p^2}\nabla^2\phi \tag{4.40}$$

The plasma index of refraction for an undercritical plasma ($n_0 \ll n_c$)

$$\eta = \frac{v_p}{c} \approx 1 - \frac{1}{2\gamma}\left(\frac{\omega_p}{\omega}\right)^2 \approx 1 - \frac{1}{2}\frac{n_0}{n_c}\left(1 + \frac{n}{n_0} - \frac{\bar{a}^2}{4}\right). \tag{4.41}$$

The plasma critical density n_c is proportional to light frequency ω squared. The plasma local density n is proportional to the plasma frequency ω_p squared and is equal to the plasma background density n_0 before the laser arrives and far from the interaction. The relativistic factor associated with the electron's motion in the laser field is $\gamma \approx \gamma_\perp$ to leading order in a, where $\gamma_\perp$ is factor associated with the electron's quiver motion in the laser field and is related to the field envelope by $\gamma_\perp = (1+\bar{a}^2/2)^{1/2}$.

Starting from Eqns. 4.38 and 4.39, the plasma potential is given by

$$\begin{aligned}\phi =& \frac{-k_p}{4}\int_{\xi}^{\infty} d\xi' \ \sin[k_p(\xi-\xi')]\bar{a}(x,\xi')^2 \\ =& \frac{-k_p a_0^2}{4} e^{-2\frac{x^2+y^2}{W^2}} \operatorname{Im}\left\{ e^{ik_p\xi}\int_{\xi}^{\infty} d\xi' \ e^{-\frac{2}{L^2}\xi'^2} e^{-ik_p\xi'} \right\}\end{aligned} \tag{4.42}$$

The exponent in the integral can be rewritten as

$$\begin{aligned}\frac{2}{L^2}\xi'^2 + ik_p\xi' &= \left(\frac{\sqrt{2}}{L}\xi' + \frac{ik_pL}{2\sqrt{2}}\right)^2 + \frac{(k_pL)^2}{2} \\ &= \left(\mu - q\nu + \frac{ik_pL}{2\sqrt{2}}\right)^2 + \frac{(k_pL)^2}{8}\end{aligned} \tag{4.43}$$

so the normalized plasma potential is given by

$$\begin{aligned}\phi =& \frac{-k_p}{4}a_0^2 e^{-\frac{(k_pL)^2}{8}} e^{-2\frac{x^2+y^2}{W^2}} \operatorname{Im}\left\{e^{ik_p\xi}\int_\xi^\infty d\xi'\ e^{-(\frac{\sqrt{2}}{L}\xi' + \frac{ik_pL}{2\sqrt{2}})^2}\right\} \\ =& \frac{-k_p}{4}a_0^2 e^{-\frac{(k_pL)^2}{8}} e^{-2\frac{x^2+y^2}{W^2}} \operatorname{Im}\left\{e^{ik_p\xi}\int_\chi^\infty \frac{L}{\sqrt{2}}d\chi'\ e^{-\chi'^2}\right\} \\ =& \frac{-k_pL}{8}a_0^2\sqrt{\frac{\pi}{2}} e^{-\frac{(k_pL)^2}{8}} e^{-2\frac{x^2+y^2}{W^2}} \operatorname{Im}\left\{e^{ik_p\xi}\left[1 - \operatorname{Erf}(\chi)\right]\right\}\end{aligned} \tag{4.44}$$

where $\chi'(\xi') = \frac{\sqrt{2}}{L}\xi' + \frac{ik_pL}{2\sqrt{2}}$ so $d\xi' = \frac{L}{\sqrt{2}}d\chi'$.

This expression for ϕ can be written at $t = 0$ in dimensionless variables as

$$\phi|_{t=0} = \frac{-k_pL}{8}a_0^2\sqrt{\frac{\pi}{2}} e^{-\frac{(k_pL)^2}{8}} e^{-(\nu^2+\varrho^2)} \operatorname{Im}\left\{e^{i(k_pL/\sqrt{2})(\mu-q\nu)}\left[1 - \operatorname{Erf}(\chi)\right]\right\} \tag{4.45}$$

where $\chi = \frac{\sqrt{2}}{L}\xi + \frac{ik_pL}{\sqrt{2}} = \mu - q\nu + \frac{ik_pL}{\sqrt{2}}$. The shape of the linear wake potential (normalized to -1) can then be written as a function of only unitless parameters given by

$$\beta(\mu,\nu,q,k_pL) = \frac{1}{2}e^{-(\nu^2+\varrho^2)} \operatorname{Im}\left\{e^{i(k_pL/\sqrt{2})(\mu-q\nu)}\left[1 - \operatorname{Erf}(\mu - q\nu + \frac{ik_pL}{2\sqrt{2}})\right]\right\} \tag{4.46}$$

where $k_p\xi = (k_pL/\sqrt{2})(\mu - q\nu)$. The plasma potential is then

$$\phi|_{t=0} = \frac{-k_pL}{4}a_0^2\sqrt{\frac{\pi}{2}} e^{-\frac{(k_pL)^2}{8}}\beta(\mu,\nu,q,k_pL). \tag{4.47}$$

The wake density can be rewritten in terms of these unitless functions as

$$\begin{aligned}\frac{n}{n_0} &= 1 + \frac{1}{k_p^2}\nabla^2\phi = 1 + \frac{1}{k_p^2}\left(\frac{\partial^2\phi}{\partial z^2} + \frac{\partial^2\phi}{\partial x^2} + \frac{\partial^2\phi}{\partial y^2}\right) \\ &= 1 + \frac{1}{k_p^2}\left(\frac{2}{L^2}\frac{\partial^2\phi}{\partial\mu^2} + \frac{2}{W^2}\frac{\partial^2\phi}{\partial\nu^2} + \frac{2}{W^2}\frac{\partial^2\phi}{\partial\varrho^2}\right) \\ &= 1 - \frac{pc}{2}k_pWa_0^2\sqrt{\frac{\pi}{2}} e^{-\frac{(k_pL)^2}{8}} \times \\ &\qquad \frac{1}{q}\left(\frac{1}{(k_pL)^2}\frac{\partial^2\beta}{\partial\mu^2} + \frac{1}{(k_pW)^2}\frac{\partial^2\beta}{\partial\nu^2} + \frac{1}{(k_pW)^2}\frac{\partial^2\beta}{\partial\varrho^2}\right)\end{aligned} \tag{4.48}$$

where $1/q = L/pcW$. The derivative of the laser intensity envelope with respect to ν is given by

$$\begin{aligned}\frac{\partial}{\partial\nu}\bar{a}^2 =&\frac{\partial}{\partial\nu}\left(a_0^2 e^{-\nu^2} e^{-(\mu-q\nu)^2}\right)\\ =&2[q\mu-\nu(1+q^2)]\bar{a}^2.\end{aligned} \tag{4.49}$$

Combining these terms, the ray deflection from Eqn. 4.36 can be written using the index of refraction from Eqn. 4.41 as

$$\begin{aligned}\frac{\mathrm{d}\Theta}{\mathrm{d}z} =&\frac{\partial\eta}{\partial x} = \frac{\sqrt{2}}{W}\frac{\partial\eta}{\partial\nu} = \frac{\sqrt{2}}{W}\frac{\partial}{\partial\nu}\left[1-\frac{1}{2}\frac{n_0}{n_c}\left(\frac{n}{n_0}-\frac{\bar{a}^2}{4}\right)\right]\\ =&\frac{1}{4\sqrt{2}W}\frac{n_0}{n_c}\frac{\partial}{\partial\nu}\bar{a}^2 - \frac{1}{\sqrt{2}W}\frac{n_0}{n_c}\frac{\partial}{\partial\nu}\left(\frac{n}{n_0}\right).\end{aligned} \tag{4.50}$$

The deflection of the pulse is the intensity weighted average of the ray deflection, defined by

$$\left\langle\frac{d\Theta}{dz}\right\rangle = \iiint \frac{d\Theta}{dz}\bar{a}(x,z)^2 dx\,dy\,dz \Big/ \iiint \bar{a}(x,z)^2 dx\,dy\,dz \tag{4.51}$$

$$=\frac{n_0}{n_c}\frac{k_p}{4}(pc)a_0^2\sqrt{\pi}e^{-\frac{(k_pL)^2}{8}}\left[f+g+h+l\right] \tag{4.52}$$

where the four functions are defined as

$$\begin{aligned}f(q,k_pL) =&\frac{1}{q}\frac{1}{(k_pL)^2}\left\langle e^{-(\nu^2+\varrho^2)}e^{-(\mu-q\nu)^2}\left(\frac{\partial^3\beta}{\partial\nu\partial\mu^2}\right)\right\rangle\\ \approx&\begin{cases}\frac{k_pL}{8}\exp\left\{-\frac{(k_pL)^2}{8}\right\} & \text{2D}\\ \frac{k_pL}{8\sqrt{2}}\exp\left\{-\frac{(k_pL)^2}{8}\right\} & \text{3D.}\end{cases}\end{aligned} \tag{4.53}$$

$$\begin{aligned}g(q,k_pL,k_pW) =&\frac{1}{q}\frac{1}{(k_pW)^2}\left\langle e^{-(\nu^2+\varrho^2)}e^{-(\mu-q\nu)^2}\left(\frac{\partial^3\beta}{\partial\mu^3}\right)\right\rangle\\ \approx&\begin{cases}\frac{3}{4}\frac{k_pL}{(k_pW)^2}\exp\left\{-\frac{(k_pL)^2}{8}\right\} & \text{(2D)}\\ \frac{3}{4\sqrt{2}}\frac{k_pL}{(k_pW)^2}\exp\left\{-\frac{(k_pL)^2}{8}\right\} & \text{(3D)}\end{cases}\end{aligned} \tag{4.54}$$

$$\begin{aligned}h(q,k_pL) =&\frac{1}{q}\frac{1}{(k_pW)^2}\left\langle e^{-(\nu^2+\varrho^2)}e^{-(\mu-q\nu)^2}\left(\frac{\partial^3\beta}{\partial\varrho\partial\mu^2}\right)\right\rangle\\ \approx&\begin{cases}0 & \text{(2D)}\\ \frac{1}{4\sqrt{2}}\frac{k_pL}{(k_pW)^2}\exp\left\{-\frac{(k_pL)^2}{8}\right\} & \text{(3D)}\end{cases}\end{aligned} \tag{4.55}$$

and

$$\begin{aligned} l(q,k_pL) =& \frac{1}{q}\sqrt{\frac{2}{\pi}}\frac{1}{k_pL}e^{\frac{(k_pL)^2}{8}}\left\langle (q\mu-\nu(1+q^2))e^{-2(\nu^2+\varrho^2)}e^{-2(\mu-q\nu)^2}\right\rangle \\ =& 0 \quad \text{(2D \& 3D)} \end{aligned} \tag{4.56}$$

The 2D results come from dropping the dependence on ϱ and are presented for comparison with simulations. The final values for the functions f, g, and h are given as approximate because they were determined by numerical fit. The fourth function h is identically zero when averaged over the pulse because it is antisymmetric with respect to ν and μ.

The solution [71] for the angular deflection of the pulse is then

$$\begin{aligned} \left\langle \frac{d\Theta}{dz}\right\rangle =& \frac{n_0}{n_c}\frac{k_p}{4}(pc)a_0^2\sqrt{\pi}e^{-\frac{(k_pL)^2}{8}}\left[f+g+h\right] \\ =& \frac{n_0}{n_c}\frac{k_p}{16}(pc)(k_pL)a_0^2\sqrt{\pi}e^{-\frac{(k_pL)^2}{4}}\times\begin{cases}\frac{1}{2}+\frac{3}{(k_pW)^2} & \text{(2D)}\\ \frac{1}{2\sqrt{2}}+\frac{4}{\sqrt{2}(k_pW)^2} & \text{(3D)}\end{cases} \end{aligned} \tag{4.57}$$

Theory Comparison with Simulation

Two dimensional simulations were run with the particle-in-cell (PIC) simulation code WARP to check the validity of Eqn. 4.57. In each set of simulations, one parameter was varied while the other parameters listed in Table 4.1 were held fixed. The results are shown in Figure 4.4. The simulations were run with $W \gg L$ so the second term of the laser steering equation could be neglected. The results of the individual simulations are shown as + symbols and the theoretical model of Eqn. 4.57 is shown as a solid line. Figure 4.4(a) shows that the theoretical model quickly diverges from the simulation results as $a \to 1$, which is expected since $a_0 \ll 1$ was one of the assumptions of the derivations.

Table 4.1: Parameters for 2D WARP Simulations

a_0	0.5	n [cm^{-3}]	10^{18}
k_pL	1.44	λ [nm]	800
pc	0.00236	ψ[nrad/nm]	-1.69

If $a \gtrsim 1$ the perturbative expansion in a^2 of the γ factor from Eqn. 4.41 is no longer valid, although it was shown in Eqn. 4.56 the term had no effect on pointing in the regime $a_0 \ll 1$. For high a, the factor $\gamma(a)$ can be estimated with the peak value a_0 as $\gamma_0 = \sqrt{1+a_0^2/2}$. This approximation is also suggested because the amplitude of the wake scales as a_0^2/γ_0 as a increases beyond the linear regime, which reduces to a_0^2 for small a_0 [8]. An additional consideration at high a is that the plasma wavelength elongates. The nonlinear plasma wavelength is given by

$$\lambda_{p,NL} = \lambda_p[1+(3/16)(E_{max}/E_0)^2] \tag{4.58}$$

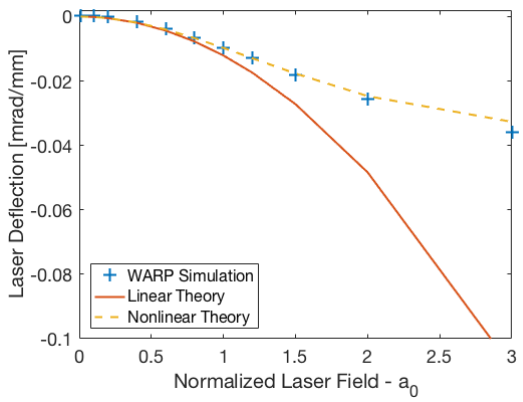

(a) Steering as a function of intensity

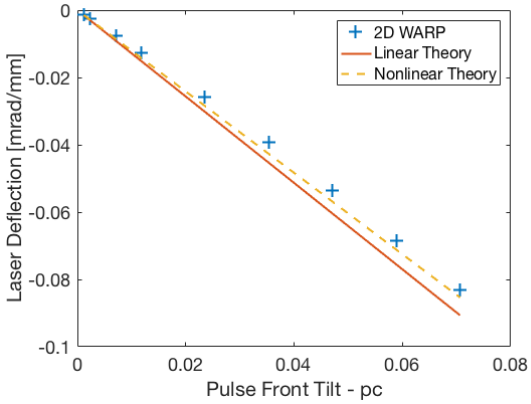

(b) Steering as a function of pulse front tilt

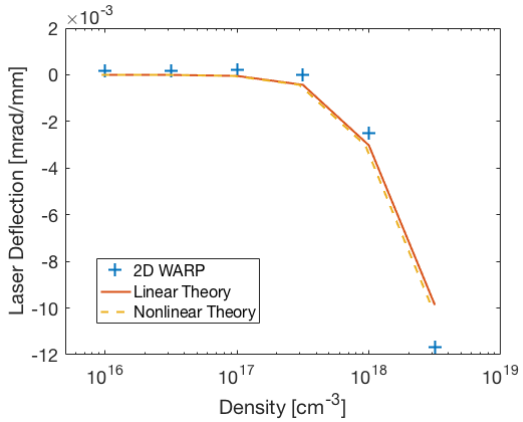

(c) Steering as a function of density

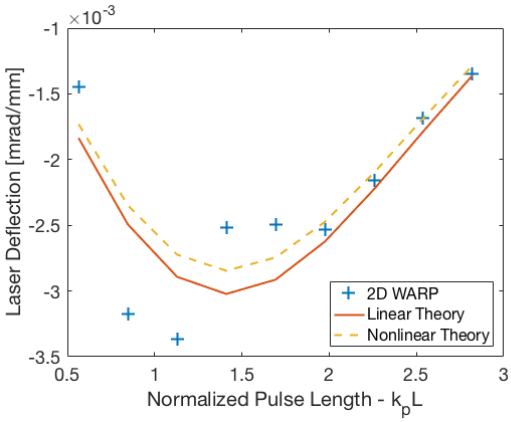

(d) Steering as a function of pulse length or k_pL

Figure 4.4: Comparison of laser deflection scaling for several parameters between 2D WARP simulations and theory.

where $E_{max} \ll E_0$ is the maximum accelerating gradient of the wake. In the linear regime ($a \ll 1$) for a Gaussian laser pulse with linear polarization [8, 59]

$$\frac{E_{max}}{E_0} = \frac{a_0^2}{4}\sqrt{\frac{\pi}{2}}e^{-(k_pL)^2/8} \tag{4.59}$$

where L is the $1/e^2$ length of the laser pulse. This can be approximated for higher a as

$$\frac{E_{max}}{E_0} \approx \frac{a_0^2}{4\gamma_0}\sqrt{\frac{\pi}{2}}e^{-(k_pL)^2/8}. \tag{4.60}$$

Defining $k_{p,NL} = 2\pi/\lambda_{p,NL}$, applying these correction factors to Eqn. 4.57 yields [71]

$$\left\langle \frac{d\Theta}{dz} \right\rangle = \frac{a_0^2}{\gamma_0}\frac{n_0}{n_c}\frac{k_{p,NL}}{16}(pc)(k_{p,NL}L)\sqrt{\pi}e^{-\frac{(k_{p,NL}L)^2}{4}} \times \begin{cases} \frac{1}{2} + \frac{3}{(k_pW)^2} & \text{(2D)} \\ \frac{1}{2\sqrt{2}} + \frac{4}{\sqrt{2}(k_pW)^2} & \text{(3D)} \end{cases} \tag{4.61}$$

which is plotted as dashed lines in Figure 4.4. The plasma wavelength does not elongate in the transverse direction, so the terms k_pW were not substituted with $k_{p,NL}W$. This corrected theory extends the range of agreement with the simulation results to $a \lesssim 2$. It also slightly improves agreement with the pointing predicted as a function of pulse front tilt, shown in Figure 4.4(b). Both theoretical results have a small disagreement with the simulated laser propagation as a function of density, plotted in Figure 4.4(c), which increases with density. This is due to evolution of the laser pulse, which causes the pulse to evolve and become increasingly non-Gaussian by the end of the simulation. The agreement with the final parameter of the theory, the pulse length, is shown in Figure 4.4(d) in which the pulse length is varied by the plasma density is kept fixed at 1×10^{18} cm^{-3}. The theory only agrees with the simulations results for $k_pL \gtrsim 2$. Below this value, the simulations give large oscillations in laser deflection with varying pulse length, while the theory developed here predicts a smooth trend. This discrepancy will be investigated in future work [71].

4.4 Particle Acceleration with Plasma Waves

Acceleration and Transverse Focusing

In addition to the axial electric field of the wake, there is a transverse component which can focus or defocus an accelerating electron bunch. The region of the laser wake that is useful for accelerating particles is where the axial electric field is accelerating and the transverse field is focusing. Such a region is called a bucket, and the buckets are identified by position behind the laser (*i.e.*, 1st bucket, 2nd bucket...).

In the linear regime ($a \ll 1$), the axial electric field, E_z varies sinusoidally with longitudinal position, so the force is accelerating for half of the wave and decelerating for half of the wave. Its magnitude is on the order of the cold wave breaking limit $E_0 = mc\omega_p/e = 30 - 300$ V m^{-1} for high-density laboratory plasmas in the range $n \sim 10^{17} - 10^{19}$ cm^{-3}. The focusing field also varies sinusoidally as a function of k_pz but is $\pi/2$ out of phase with respect to the axial field. The density wake from a Gaussian pulse with $k_pL = 0.75$ and $a_0^2 = 0.4$ is shown in Figure 4.5(a) along with blue vector representing the direction and relative magnitude of force that a test electron would feel if introduced into the wake at that location. The first and second buckets (regions of the wake that are both accelerating and focusing) are highlighted in Figure 4.5(b).

In the bubble regime (Eqn. 4.35), all the electrons are expelled from the wake leaving a bubble of uniform positive charge. The bubble is approximately spherical provided $k_pw_0 \approx 2\sqrt{a_0}$ where w_0 is the laser transverse size [69]. In the rear half of the bubble, where the

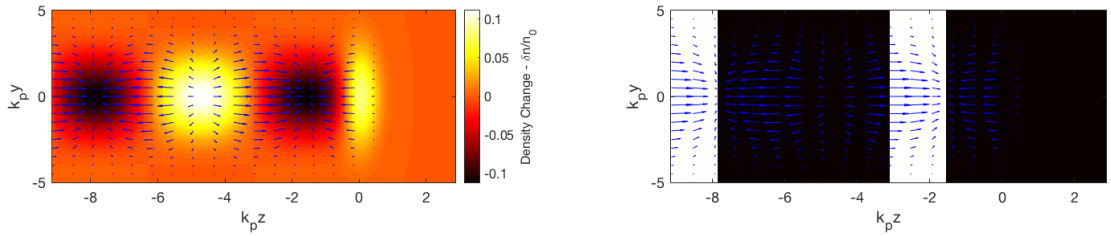

(a) Wake density and associated force on a test electron

(b) Electron forces with accelerating and focusing region highlighted

Figure 4.5: Electron force field resulting from a plasma density wake following a laser centered at $k_p y = k_p z = 0$.

electric field is both accelerating and focusing, the axial field is approximately linear with z rising from 0 in the center of the bubble to $E_0 k_p R_b/2$ where $R_b \approx 2\sqrt{a_0}/k_p$ is the bubble radius [67, 69]. The radial focusing force on an electron in the rear of the bubble scales linearly with distance from the axis. It is given by $-e(E_r - B_\theta) = -eE_0 r/2$ assuming the electron velocity $v_e \approx c$.

Acceleration Limits

If electrons are injected near the rear of the bucket with an initial velocity $v_{e,0} \geq v_{p,wake}$ where $v_{p,wake}$ is the wake phase velocity, they would gain energy from the electric field. Since the laser is moving through material (plasma), it's forward speed is $v_{g,laser} < c$, and injected electrons would slowly move forward relative to the bucket until they entered a region with a decelerating electric field. This dephasing process is a natural limit of how much energy can be gained from a single laser-driven accelerator. The propagation distance before dephasing occurs is given [8] by

$$L_D \approx \frac{\lambda_p^3}{2\lambda^2} \times \begin{cases} 1 & a_0^2 \ll 1 \\ (\sqrt{2}/\pi) a_0/N_b & a_0^2 \gg 1 \end{cases} \tag{4.62}$$

where N_b is the number of the bucket that the electrons are in.

Another limitations on acceleration length is energy loss of the driving laser (*i.e.*, laser depletion), given [8] by

$$L_E \approx \frac{\lambda_p^3}{2\lambda^2} \times \begin{cases} 2/a_0^2 & a_0^2 \ll 1 \\ (\sqrt{2}/\pi) a_0 & a_0^2 \gg 1 \end{cases} \tag{4.63}$$

In addition, the acceleration region is limited to the range over which that laser stays at high intensity. The peak intensity of laser pulse with a transverse Gaussian profile will drop by 1/2 after it has propagated by a Rayleigh length $Z_R = \frac{1}{2} k_0 w_0^2$ from its focus location due to diffraction. Nonlinear optical processes in the plasma which act counter to diffraction to keep the laser at high intensity are discussed in §4.3.

Betatron Motion

Electrons in the wake will oscillate around the optical axis due to the focusing forces of the wake if they are displaced or injected off-axis. This oscillation is called betatron motion and is damped as the electrons gain energy from the wake, increasing their relativistic factor γ_e. The characteristic wavelength associated with betatron motion is $\lambda_\beta = \pi w_0 \sqrt{\gamma_e/\phi_0}$ [72]. Here ϕ_0 is the amplitude of the normalized potential associated with the wake, given by Eqn. 4.29 for the linear regime and w_0 is the $1/e^2$ laser radius. In the bubble regime, this reduces to $\lambda_\beta = \lambda_p \sqrt{2\gamma_e}$ [72].

Electron Steering from Pulse Front Tilt

Pulse front tilt (PFT) in the driving laser pulse creates a plasma structure which is also tilted. In the absence of PFT, injected electrons are kept close to the laser axis by the transverse focusing forces $-eE_x$ and $-e(v_{e,z}/c)B_\theta$ where $v_{e,z}$ is the z component of the electron velocity. In the presence of PFT, the laser focusing forces are non-zero along the laser axis due to the change in the wake structure. Instead, there exists a line through the wake along which the focusing forces are zero, which makes a small angle to the z-axis and goes through the point where $E_z = E_x = 0$ (the center of the wake and front of the bucket).

To determine the angle of that line, the wake is modeled as an ellipsoid with its center shifted along ξ at each height, as in

$$1 = \left(\frac{\xi - pcy}{L_w}\right)^2 + \left(\frac{x}{W_w}\right)^2 + \left(\frac{y}{W_w}\right)^2. \tag{4.64}$$

The $y\xi$ cross section is shown in Figure 4.6(a) where an upright dashed line indicates the plane $\xi = \tan(\theta_{PFT})y$ and the angle of the plane to the y-axis is $\theta_{PFT} = \operatorname{atan}(pc)$. There exists a line in the $y\xi$-plane which cuts the ellipse in half such that at each value of ξ the y-distance from the line to the upper wake boundary and to the lower wake boundary is the same. If the wake ellipsoid has a uniform charge density, then this line is the location where the transverse focusing force is zero. It is shown in Figure 4.6(a) as a dashed line, and its angle to the ξ-axis is labelled θ_w, given [71] by

$$\tan\theta_w = \frac{pcW_w^2}{L_w^2 + (pcW_w)^2} \approx pc\left(\frac{W_w}{L_w}\right)^2 \tag{4.65}$$

where W_w and L_w are the length and width of the wake, respectively. The approximation is valid for $pc \ll 1$.

Electrons injected into the wake will be forced to the θ_w line by the transverse focusing forces, causing a deflection of the electrons in the stationary laboratory frame. Their longitudinal position in the wake ξ_e is fixed in the coordinate system $(x, y, \xi = z - ct)$ because $v_e \approx c$ after the electrons have propagated a distance $z \sim \lambda_p$ while in the accelerating phase of the wake. Their initial longitudinal position is assumed to be the back of the bubble, which

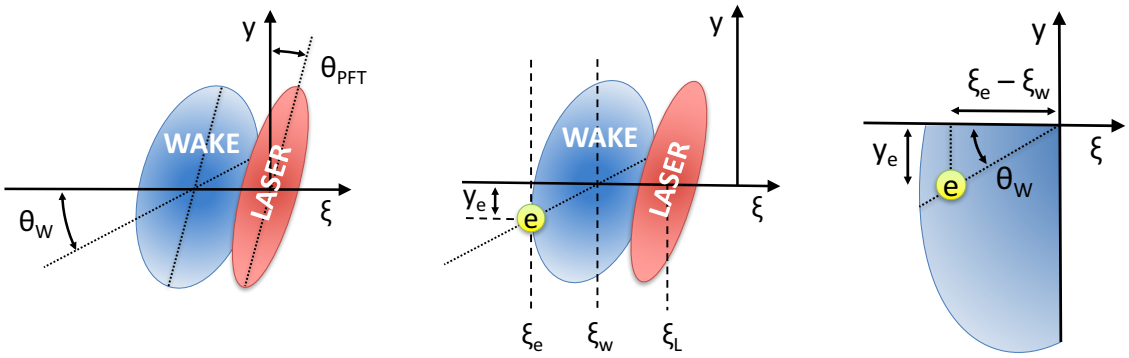

(a) Tilted laser and wake from pulse front tilt angle and resulting wake angle

(b) Positions of electron bunch, wake center, and laser

(c) Relationship between electron longitudinal and transverse positions

Figure 4.6: Ellipsoid model schematic of tilted wake and accelerating electron bunch.

is consistent with both self-injection [70] and density down-ramp [73] injection, both of which are relevant to these LPA experiments. The time and wake length, t_{inj} and L_{inj} respectively, at which the electrons are injected into the wake set the electron location in the coordinate system.

The position of the laser $\xi_L = (v_g - c)t$, however, is not constant since the laser group velocity is $v_g \approx 1 - \omega_p^2/2\gamma\omega^2 < c$. By definition, $\xi_L = 0$ at $t = 0$ as in Figure 4.6(a). Likewise, the wake center position $\xi_w = \xi_L - L_w$ slips backwards relative to the origin and the injected electrons as the laser propagates. These are illustrated in Figure 4.6(b) along with the transverse position of the electrons, y_e. The electrons' transverse position on the wake line is related to its longitudinal position by $y_e = (\xi_e - \xi_w)\tan\theta_w$ as illustrated in Figure 4.6(c). The electron transverse position [71] is thus given by

$$y_e = (\xi_e - \xi_b)\tan\theta_w = [(v_g - c)(t_{inj} - t) - 2[L_{inj} - L_w] - L_w]\tan\theta_w. \tag{4.66}$$

The first term in Eqn. 4.66 is the contribution to the electron deflection from forward movement along the θ_w line. If the PFT angle and bubble size are fixed, this is the only term with a nonzero derivative. It is written in terms of v_g assuming that the laser group velocity is fixed at the value where the electrons are injected. If the group velocity varies for a large fraction of the laser propagation, which is not the case in these experiments, then the first term should be written as the more general expression $\xi_{e,inj} - \xi_e$. The second term is deflection from changing wake size. The final term is deflection from changes in the location of ξ_w and consequently the origin of the θ_w line, caused by evolving pulse front tilt or changing wake length.

The ellipsoid wake model can be applied to both the linear and bubble regimes. In the matched bubble regime where the laser spot size $w_0 \approx 2\sqrt{a_0}/k_p$, the wake dimensions $W_w \approx L_w \approx 2\sqrt{a_0}/k_p$ since the bubble in the absence of PFT is approximately a sphere of

this size with uniform charge. In the linear regime, the charge density of the wake is not uniform, except near the center of the wake/front of the bucket so the ellipsoid model is only applicable to electrons near the center of the wake (*i.e.*, approaching the dephasing limit). In this regime, $W_w = w_0$ since the laser transverse size w_0 sets the transverse size of the wake and $L_w = \lambda_p/\pi = 2/k_p$ since this gives an ellipsoid whose boundary has approximately constant charge density. If the plasma wake is in the bubble regime but the laser driver is not matched to the bubble size, the wake dimensions can be estimated as $W_w \approx w_0$ and $L_w \approx 2/k_{p,NL} = \lambda_{p,NL}/\pi$ where $\lambda_{p,NL}$ is the nonlinear plasma wavelength given by Eqn. 4.58. The factor $E_{z,max}/E_0$ in Eqn. 4.58 can be approximated by Eqn. 4.60 for a Gaussian pulse.

The density wake and resulting electron forces from a Gaussian pulse in the linear regime ($a_0^2 = 0.4$ and $k_pL = 0.75$) with very large PFT ($pc = 0.2$) are shown in Figure 4.7(a). The minimum transverse focusing forces are shown in Figure 4.7(b) with a saturated color scale to highlight the regions with no transverse focusing (dark bands). In blue are the lines $y = \tan\theta_w(\xi - \xi_w)$ for the first and second buckets, centered at $\xi_{w,1} = -(1/4)\lambda_p$ and $\xi_{w,2} = -(5/4)\lambda_p$, respectively. In both cases the theoretical lines agree with the minimum focusing force calculated from Eqn. 4.30.

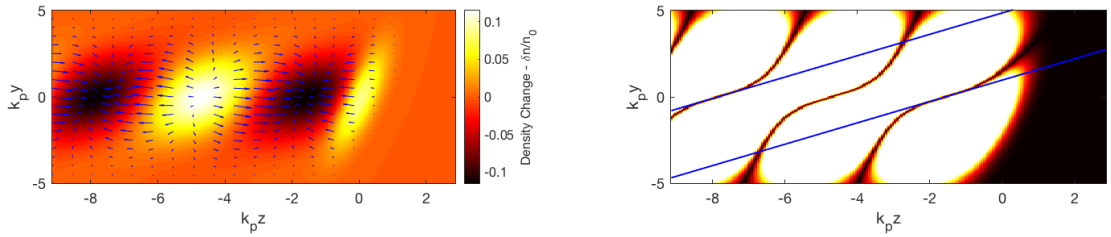

(a) Linear wake density and electron forces from a laser with very large PFT ($pc = 0.2$)

(b) Regions with focusing force $E_y \approx 0$ and lines with slope $\tan\theta_w$ through the first two buckets

Figure 4.7: Linear wake with large PFT and associated focusing forces.

The preceding discussion assumed the electrons were stuck to the wake line with no focusing forces, but this ignores the betatron motion of the electrons. A typical situation is shown in Figure 4.8(a), in which electrons are injected into the wake at $z = 0$ mm and gain ~600 MeV of energy by the end of the plasma region. The transverse position of the wake is plotted in red in Figure 4.8(b), and the transverse position of the electrons due to betatron motion as they attempt to follow the wake line is plotted in black. The pulse front tilt angle of the laser slowly decreases and the intensity remains close to $a_0 \sim 3$. The black curve is the numerical solution to

$$\frac{\mathrm{d}^2 y_\beta}{\mathrm{d}z^2} = \left(\frac{2\pi}{\lambda_\beta}\right)^2 (y_e - y_\beta) \tag{4.67}$$

where y_e is given by Eqn. 4.66 and y_β is the betatron motion of the monoenergetic electrons. This model excludes the mechanisms which damp the betatron motion. At low electron energies and high density (low z) the betatron wavelength is short compared to changes

in y_e so the electrons easily track the laser wake. As density drops and the electrons gain energy, the betatron wavelength increases rapidly resulting in a lag between changes in y_e and matching changes in y_β. At the end of the plasma region ($z \sim 10$ mm), the electrons no longer follow the wake because λ_β has become larger than the length scale over which y_e is changing.

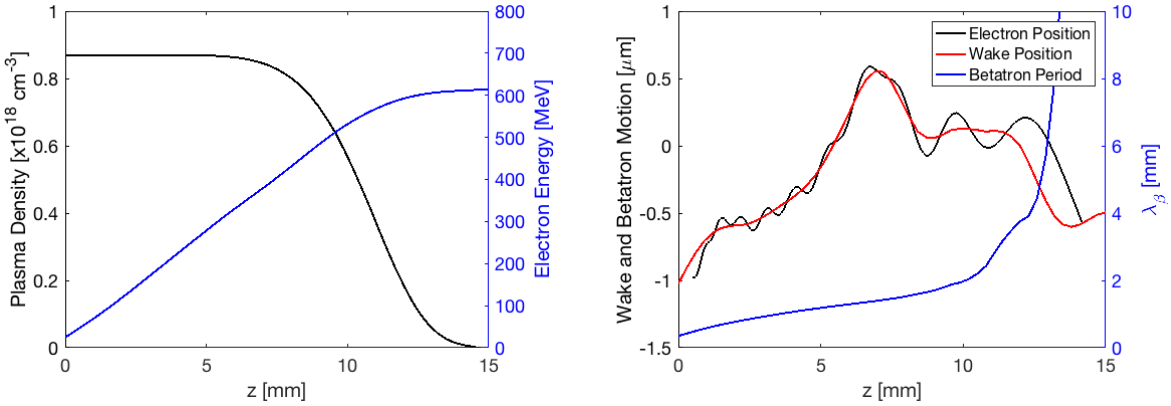

(a) Plasma density and simulated electron energy. (b) Electron and wake position at plasma exit.

Figure 4.8: Simulated betatron motion of an electron exiting a plasma, assuming a linear restoring force.

At the end of a plasma target, electrons accelerated by a drive laser with pulse front tilt will be deflected due to the transition from plasma to vacuum. If changes in the wake angle and size due to the changing density are slow relative to the length scale of betatron motion, the electrons can then be assumed to follow the wake line with zero transverse force and betatron motion can be ignored. Explicitly, this condition is

$$\lambda_\beta \ll \left| \frac{1}{y_e} \frac{\mathrm{d}y_e}{\mathrm{d}z} \right|^{-1} \approx 2n_e \left| \frac{\mathrm{d}n_e}{\mathrm{d}z} \right|^{-1}. \tag{4.68}$$

The approximation assumes the wake angle is changing primarily due to the changing density. Then the output angle of the electrons is given by

$$\theta_e = \theta_l + \frac{\mathrm{d}y_e}{\mathrm{d}z} \tag{4.69}$$

where θ_l is the deflection angle of the laser, if any, since the electron motion is defined relative to the laser propagation axis. If the transition is faster so

$$\lambda_\beta \gtrsim 2n_e \left| \frac{\mathrm{d}n_e}{\mathrm{d}z} \right|^{-1} \tag{4.70}$$

the electrons will make few oscillations in the wake as the density drops. However, $k_\beta \to 0$ as the density drops to zero so this condition is almost always satisfied at the end of a plasma. Intuitively, the model of electrons following the wake line must break down because at some point λ_β grows larger than the remaining plasma length. The exception is when the density drop is instantaneous (e.g. from crossing a supersonic shock). The electrons will gain transverse momentum from the transverse focusing force but will not be able to return to the wake line. In the bubble regime, the transverse focusing force from a small displacement δy off the wake line is given by

$$F_y = -eE_y - eB_\theta = -\frac{e}{2}k_p E_0 \delta y \tag{4.71}$$

and the corresponding change in transverse velocity is given by

$$\delta v_y = \frac{\delta p_y}{\gamma_e m} = \frac{F\delta t}{\gamma_e m} = -\frac{eE_0 k_p}{2\gamma_e m}\delta t \delta y \tag{4.72}$$

where $p_y = \gamma_e m v_y$ is the electron transverse momentum. Rearranging and taking the limit as $\delta y \to 0$ and gives an expression for the changing transverse velocity of the electrons

$$\frac{\mathrm{d}^2 v_y}{\mathrm{d}t^2} = -\frac{eE_0 k_p}{2\gamma_e m}\frac{\mathrm{d}y}{\mathrm{d}t}. \tag{4.73}$$

The variable y represents displacement of the electrons from the wake line. This displacement can be caused by a movement of the wake line $\mathrm{d}y_e/\mathrm{d}t$ relative to the laser propagation axis. As discussed in §4.3, pulse front tilt also causes deflection of the laser driver, and the displacement of the electrons relative to the wake can also be due to this deflection. If laser propagates with a constant angle to the z-axis, there only effect on the final electron angle is a constant offset (the θ_l term in Eqn. 4.69), and the laser propagation has no effect on Eqn. 4.73. A change in the laser propagation angle will cause a corresponding shift in the electron position relative to the wake angle. The shift will be proportional to the rate of change $\mathrm{d}\theta_l/\mathrm{d}t$ and the length-scale over which the electrons react to the displacement λ_β. The second derivative in transverse velocity is thus

$$\frac{\mathrm{d}^2 v_y}{\mathrm{d}z^2} = -\frac{eE_0 k_p}{2\gamma_e mc}\frac{\mathrm{d}y}{\mathrm{d}z} = -\frac{eE_0 k_p}{2\gamma_e mc}\left(\frac{\mathrm{d}y_e}{\mathrm{d}z} + \frac{\mathrm{d}\theta_l}{\mathrm{d}z}\lambda_\beta\right). \tag{4.74}$$

Here the fact that $z = ct$ is used to change the variable of integration. From Eqn. 4.74, the transverse electron velocity can be estimated

$$v_y \approx v_{y,0} + \frac{\mathrm{d}^2 v_y}{\mathrm{d}z^2}\frac{\Delta z^2}{2} = c\frac{\mathrm{d}y_e}{\mathrm{d}z} - \frac{eE_0 k_p}{2\gamma_e mc}\left(\frac{\mathrm{d}y_e}{\mathrm{d}z} + \frac{\mathrm{d}\theta_l}{\mathrm{d}z}\lambda_\beta\right)\frac{\Delta z^2}{2} \tag{4.75}$$

with an appropriate choice of integration distance. The final electron angle is then

$$\theta_e = \theta_l + \frac{v_y}{v_x} \approx \theta_l + \frac{\mathrm{d}y_e}{\mathrm{d}z} + \frac{1}{c}\frac{\mathrm{d}^2 v_y}{\mathrm{d}z^2}\frac{\Delta z^2}{2} \tag{4.76}$$

where the middle term on the right-hand side comes from the initial transverse velocity of the electrons, caused by the moving wake line. The integration length Δz represents how long the transverse focusing force is applied for. An appropriate estimate is the length scale over which the density drops at the end of the gas jet. This yields [71]

$$\theta_e = \theta_l + \frac{\mathrm{d}y_e}{\mathrm{d}z} - \frac{eE_0k_p}{2\gamma_e mc^2}\left(\frac{\mathrm{d}y_e}{\mathrm{d}z} + \frac{\mathrm{d}\theta_l}{\mathrm{d}z}\lambda_\beta\right)\frac{1}{2}\left(\frac{1}{n_e}\frac{\mathrm{d}n_e}{\mathrm{d}z}\right)^{-2}. \tag{4.77}$$

The appropriate location near the end of the plasma to evaluate this is the first z-location that satisfies the condition in Eqn. 4.70. Thus, Eqn. 4.77 should be evaluated at z such that

$$\lambda_\beta = \left|\frac{1}{y_e}\frac{\mathrm{d}y_e}{\mathrm{d}z}\right|^{-1} \approx 2n_e\left|\frac{\mathrm{d}n_e}{\mathrm{d}z}\right|^{-1}. \tag{4.78}$$

Substituting this condition into Eqn. 4.77 yields [71]

$$\theta_e = \theta_l + \frac{\mathrm{d}y_e}{\mathrm{d}z} - \frac{\pi^2}{2}\left(\frac{\mathrm{d}y_e}{\mathrm{d}z} + \frac{\mathrm{d}\theta_l}{\mathrm{d}z}\lambda_\beta\right). \tag{4.79}$$

4.5 Concluding Remarks

The theory of laser-plasma interactions relevant to laser plasma acceleration has been presented. The temporal profile of the laser was shown to affect the spectral modulation of the laser pulse. Linear plasma wake theory was applied to pulses with pulse front tilt to derive an expression for laser deflection of a Gaussian pulse. A complimentary model of electron steering and deflection at the end of the plasma target was developed. The theory of spectral modulation will be applied in Chapter 5 to check the density profile determined in Chapter 3 and to develop a novel laser spectral phase diagnostic. The laser and electron deflection expressions are used subsequently in Chapter 6 to explain the trends observed in BELLA experiments with pulse front tilt.

Chapter 5

Spectral Shifting Experiments

The laser-plasma interaction causes modulation of the laser spectrum because the plasma index of refraction varies within the laser pulse, as discussed in Chapter 4. At the front of the laser where ionization of neutral gas occurs, this results in blue shifting of the spectrum. If the laser pulse drives a plasma wake, the variation in plasma density also causes spectral shifting (primarily red shifting). The modulation of the transmitted laser spectrum provides a sensitive probe of the laser-plasma interaction. In this chapter, techniques based on spectral shifting are introduced to characterize the laser temporal/spectral profile and to confirm the density profile determined in Chapter 3.

5.1 Ionization Blue Shifting as a Laser Diagnostic

The spectral blue shifting resulting from ionization can be used as a diagnostic of laser pulse temporal properties, for pulses with intensities high enough to ionize at focus. This method differs from the methods discussed in Chapter 2 because it probes the temporal profile at the interaction point with a target. This is an advantage because it is the *in situ* properties of the laser that must be determined to understand the laser-target interaction. Typically, a laser diagnostic such as a FROG will be placed at a relay image point of the main laser's focus, which means that the light it probes must typically travel through a vacuum window and one or several imaging lenses. This work was previously published as [19].

By varying the grating spacing in the optical compressor which creates the ionizing pulse, the blue shifted spectra can probe the dependence of nonlinear chirp on pulse compression. The spectral phase can be determined from the variation of nonlinear chirp together with Eqn. 2.15. This variation of chirp with compression is recorded in the morphology of blue shifted spectra versus compressor grating spacing. If the gas distribution of the target is known, then measurements of the blue shifted spectrum can provide an in-situ diagnostic of the pulse's spectral phase near focus using a numerical simulation to understand the complex interaction. Along with a model of pulse compression, the blue shifted spectra thus act as a diagnostic of high-order spectral phase of the laser system (i.e. the phase of the

uncompressed laser). This diagnostic can either be used to verify the spectral phase at focus from an independent measurement of complex spectrum, or test a hypothesized initial phase and then iteratively determine the true spectral phase.

Numerical Simulation of Experimental Setup and Blue Shifting

A version of the 2D-cylindrical laser-plasma interaction simulation code INF&RNO [15–17] was modified to include ionization and simplify the treatment of plasma motion. Plasma motion is typically negligible at these laser intensities and the simplification speeds up the calculations significantly. INF&RNO includes nonlinear laser evolution (e.g., relativistic self-focusing, ionization defocusing) and was used to simulate the ionizing laser's propagation through the neutral gas target and resulting blue shifting. This simulation code has been validated by extensive comparison with experiments [5, 73–76] and is widely used to model the laser-plasma interaction at BELLA.

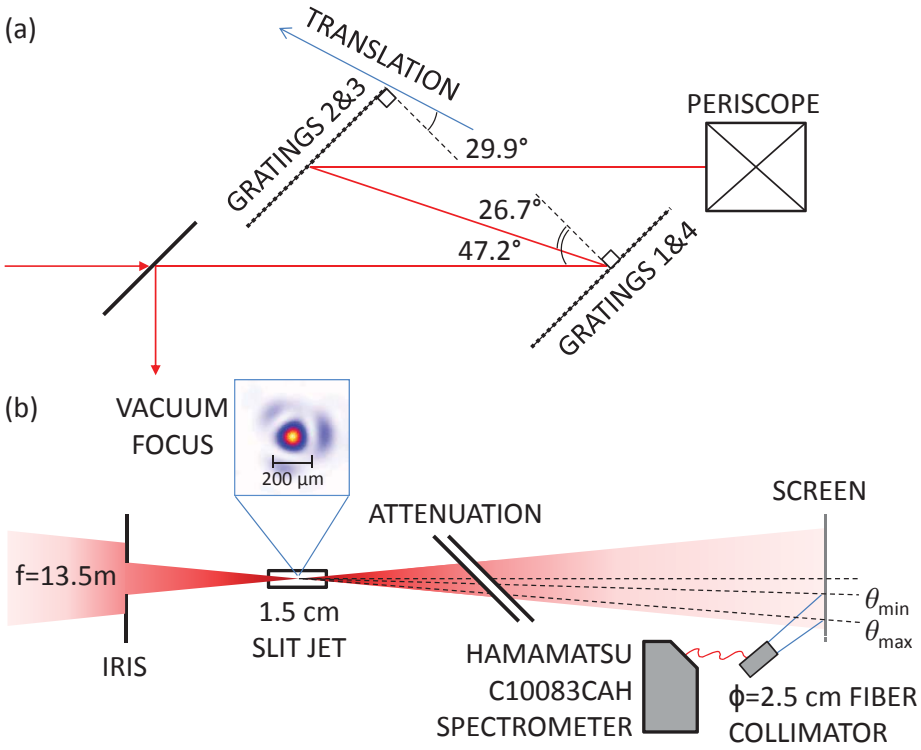

Figure 5.1: Experimental setup modeled in these simulations showing (a) optical compressor with angles of incidence and diffraction on the first and final gratings and (b) target interaction and spectrometer light collection. The minimum and maximum angles of acceptance of the spectrometer are drawn. Note the schematic is not to scale.

The propagation of an intense laser through an ionizing target was simulated for a range

of temporal profiles, resulting in a map of spectral blue shifting as a function of diffraction grating spacing. The morphology of the blue shifted spectra resulting from this series of simulations reveals the initial phase of the laser spectrum. For each simulated optical grating separation, the initial laser profile was calculated from a measured spectrum with a fixed spectral phase specified from measurements or test values. The additional phase contribution from the optical compressor was calculated from a high order model of compression [18, 27, 77]. For these simulations, the BELLA optical compressor was simulated, which consists of four matched 1480 line/mm gold-coated optical gratings arranged as shown in Figure 5.1(a). The measured spectrum with this complex phase was Fourier transformed to yield the pulse's longitudinal profile and nonlinear chirp. These longitudinal profiles, together with the transverse spatial profile, were input into INF&RNO for simulation. The initial radial profile is assumed to be an Airy pattern, corresponding to a top hat near field profile, given by

$$E(r) = 2E_0 \frac{J_1(kr/w_0)}{kr/w_0} \tag{5.1}$$

where J_1 is a first-order Bessel function and $k = 2.5838$. The value k is such that $E(w_0) = e^{-1}(e)_0$. This is an approximation to the measured beam profile shown in Figure 5.1(b).

The resulting electric field after simulated ionization and propagation was transformed into the spectral domain. This can be done by calculating the full 3D electric field and taking a Fourier Transform with respect to each axis. In this work the spectrum was recovered directly from the $r - z$ field data via a Hankel Transform with respect to r and a Fourier transform with respect to z. Conceptually, a Hankel transform is the radial part of a 2D Fourier transform. The blue shifting spectrum depends strongly on angle as a result of ionization defocusing, and the fiber-coupled spectrometer used in these experiments collected an off-axis 2.5 cm diameter portion of the approximately 8.5 cm diameter beam (reduced in size by an aperture indicated in Figure 5.1(b)) from a diffuse scattering screen. The integrated spectrum within the off-axis circular aperture was calculated from the simulated electric field as follows. First, the electric field was transformed into k-space by taking the Fourier Transform (implemented as a Fast Fourier Transform) of the electric field with respect to z and the Hankel transform with respect to r. The k-vectors which enter the angular acceptance window defined by the circular off-axis aperture (θ_{min} and θ_{max} in Figure 5.1(b)) were selected. For each frequency $\omega = ck_z$, the spectral intensity at that frequency was calculated as a weighted sum of the intensities of the selected region of k-space. The transformation to frequency assumes $k_z \gg k_r$, which is accurate for a small detector located far from the target and close to the optical axis. The weighting function illustrated in Figure 5.2 is the length extent of an arc intersecting the aperture and accounts for the varying light collection area at different angles to the optical axis.

INF&RNO includes a self-consistent model of laser pulse propagation, but does not include the linear Kerr effect nor the high order Kerr effect (HOKE) on the front edge of the laser passing through neutral gas. These effects are not strong in the regime under consideration. The linear Kerr effect can be neglected because the beams being simulated have peak intensities in the interaction $I_{peak} \gg I_{thresh}$, and the effect is negligible in comparison

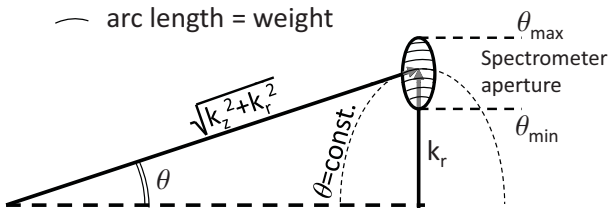

Figure 5.2: A vector in k-space is shown which satisfies the angular limits set by the collection aperture: $\theta_{min} \leq \theta \leq \theta_{max}$. The magnitude squared of the electric field corresponding to this k-vector will be included in the spectral sum for frequency ω, weighted by length of the intersection of the $\theta = \text{const.}$ line and the circular aperture.

with ionization defocusing. As an example of this, consider a transform-limited 80 mJ pulse focused to a 52 μm ($1/e^2$ intensity) Gaussian profile with a 31 fs pulse length (FWHM). This pulse will have a peak intensity of $5 \times 10^{16}\,\mathrm{W/cm^2}$, well above the ionization threshold for both hydrogen and helium. Based on the magnitude of the shift in index of refraction, ionization defocusing [78, 79] becomes more important than the linear Kerr effect when the intensity rises to only $5.5 \times 10^{13}\,\mathrm{W/cm^2}$, so just 4% of the pulse energy is more strongly affected by the Kerr effect. HOKE is not modeled because the effect is negligible for helium and other noble gasses [80].

The importance of ionization defocusing [78, 79] on the pulse propagation and final spectrum can not be overstated. Simulations show that ionization defocusing dominates diffraction in determining the evolution of pulse intensity, at least within a few Rayleigh lengths of focus. Further, the output spectrum has a strong angular dependance as a result of the ionization front's lensing effect, with more blue shifted light having a generally larger deflection. Initial 2D ray tracing simulations which included the phase shift in the laser fields from ionization, but not the effect on pulse propagation, yielded qualitatively different blue shifted spectra. For these reasons, any model of the interaction used for retrieving the spectral phase must include self-consistent laser propagation in the ionizing medium.

The goal of the simulations is to determine the unknown spectral phase from measured blue shifted spectra at various optical compression settings, but inverting the simulation (i.e. going from blue shifted spectra to initial pulse) is complicated by the highly nonlinear propagation of the ionizing pulse. It will be demonstrated that resulting spectra for various initial spectral phases can be accurately modeled, and limits will be set on the technique's sensitivity to each order of phase. Development of an iterative method algorithm to test values of initial spectral phase and compare the resulting spectral morphology with measured results, however, is not addressed in this work.

The pattern of blue shifting is sensitive to initial second, third, and fourth order dispersion and each order of spectral phase affects the structure of blue shifted spectra differently. The blue shifted spectrum is in principle sensitive to higher orders of initial spectral phase as well. The different effects on the compressed pulses simulated blue shifted spectra are shown in

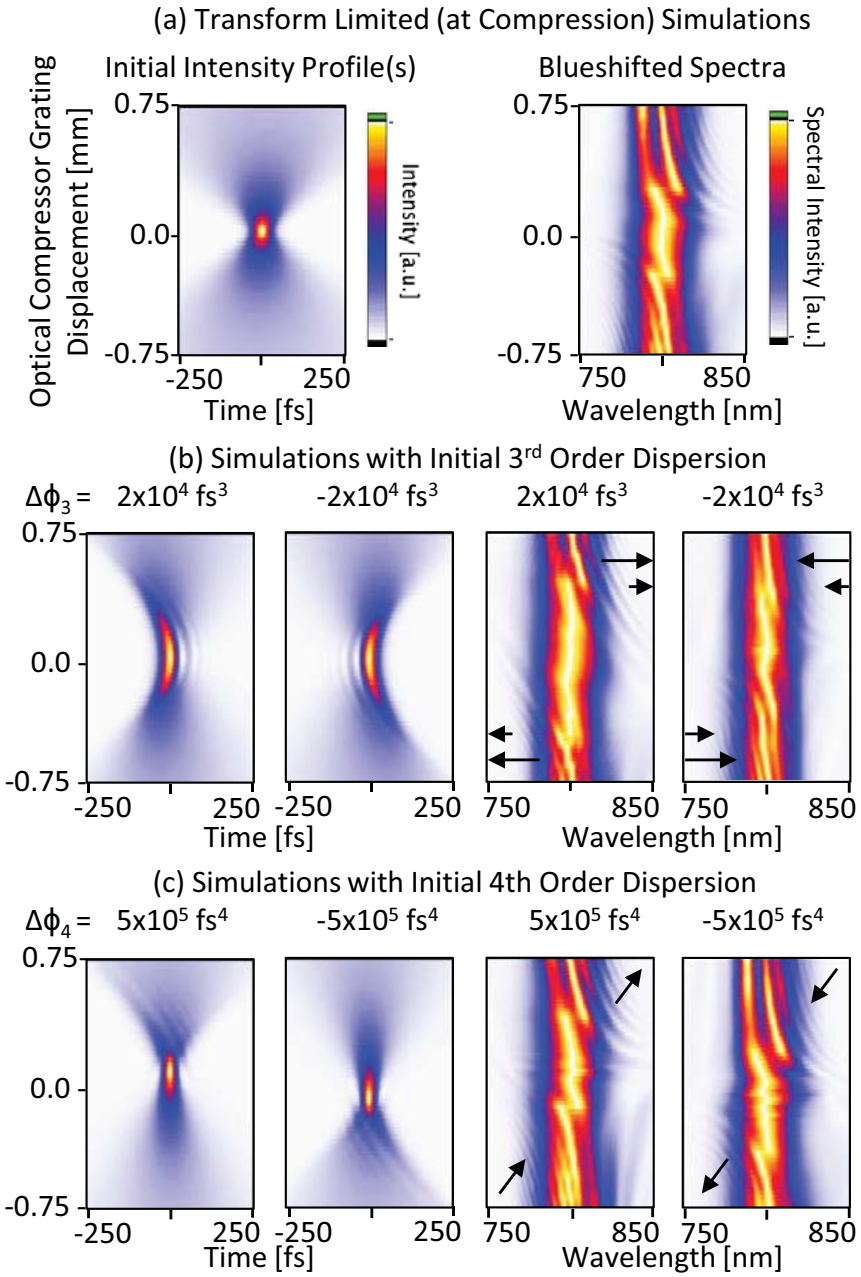

Figure 5.3: Five sets of simulations with various initial phases demonstrating the effect of laser system dispersion on pulse shape and on the morphology of blue shifted spectra and the resulting on-axis spectra. All simulated pulses have 80 mJ initial energy. Note that the initial phase added to the pulse is quoted, but phase after compression varies as a function of compressor grating spacing. Arrows are added to the blue shifted spectra to indicate how the morphology with added initial spectral phase differs from that with no dispersion.

Figure 5.3. In these simplified examples, an 80 mJ pulse is focused to a 52 μm Gaussian vacuum focal spot ($1/e^2$ radius) in the center of a 3 mm long jet of neutral hydrogen gas ($n_{H_2} = 1 \times 10^{18}\,\mathrm{cm}^{-3}$). The displayed spectra are those of the on-axis electric field. The example simulation parameters, which differ from the experimental conditions below, were chosen to make the blue shifting morphology as clear as possible. The initial intensity profiles for different compressor grating spacings are shown on the left and the resulting on-axis blue shifted spectra after propagation through gas are shown on the right. Figure 5.3(a) demonstrates the morphology from pulses which are transform limited at compression. Second order phase ϕ_2 sets the optical compressor position at which the pulse's chirp changes sign. In the temporal profile, this corresponds to the location where the pulse changes from red-first to blue-first, so in the spectral morphology, blue shifting of the spectrum and resulting spectral interference changes sides of the spectrum. For example, if the pulse is positively chirped the front of the pulse will be blue shifted to the same frequency as some location further back, and the temporal phase difference will result in interference in the spectral domain. This is demonstrated in Figure 5.3(a).

Initial third order phase ϕ_3 reduces the chirp of the main pulse and adds pre-/post-pulses to the intensity profile which contain much of the broadband spectral content of the pulse (Figure 5.3(b) left plots). If negative third order phase is added, a region of the pre-pulses will blue shift and spectrally interfere with the remainder of the pulse, increasing the number of fringes in the spectral morphology. If positive phase is instead added, the now-less-chirped main pulse will be blue shifted and will interfere with only a small band of frequencies in the post-pulses, reducing the number of fringes in the morphology. This appears as a stretching or contracting of the blue shift pattern versus grating separation. This can be understood in the time domain because added high order phase creates a larger phase difference between the front of the pulse and the rear. Because the pulse is otherwise transform limited, the quoted initial third order phase is also the phase at compression; the same is true for initial fourth order phase.

Initial fourth order phase ϕ_4 creates asymmetry in the intensity profile and nonlinear chirp with respect to peak compression. It adds pre-/post-pulses to the intensity profile on one side of compression and reduces the chirp of the main beam, reducing the resulting spectral interference fringes. On the other side of compression, it adds extended tails to the intensity profile, and the main pulse remains chirped (Figure 5.3(c) intensity profiles), adding spectral interference fringes.

Blue Shift Measurements at BELLA

Spectral blue shifting was measured at BELLA with a 1.5 cm slit gas jet target with a known density distribution. The expanding gas jet density profile was measured 10 mm from the slit jet (the distance from the laser axis to the jet face) by neutral gas interferometry and is shown in Figure 5.4 scaled to the pressure used in the blue shifting experiments. The uncertainty in the measured profile is estimated to be $\lesssim$10%. Since the slit jet lacks rotational symmetry, the profile was determined by tomographic reconstruction [51] discussed

in Chapter 3. The gas jet was operated in the blue shift experiments at higher voltage and backing pressure than in the pulse front tilt experiments so the density is considerably higher that the density profile determined for the latter operating conditions. The plateau helium density was $n_{atomic} = 1.3 \times 10^{18}\,\mathrm{cm}^{-3}$ and profile FWHM was 2.05 cm. The simulated profile was a constant density plateau of the same full width at half maximum (FWHM) and integrated density as the measured profile.

The ionizing region in a focusing laser pulse, where blue shifting occurs, will vary as the pulse focuses and its intensity changes. As the chirped pulse focuses, the region of spectrum that is blue shifted will change. The shifted spectrum of a focusing chirped pulse is therefore sensitive to the spatial distribution of neutral gas on the length-scale over which pulse intensity changes, the laser's Rayleigh length $\mathrm{Z_R}$. For this reason, the ionizing laser beam was sent through an aperture in the near field, indicated in the schematic 5.1(b), to enlarge the focal spot to $85\,\mu$m and make its focal depth longer than the jet so the spectra are relatively insensitive to the density profile except for its integrated density.

To determine a reference for spectral phase of the laser, FROG measurements [29] of the compressed laser pulses were made at a range of optical compressor settings [18, 77]. The spectral phase of the laser was determined from these measurements, which is the input for the following simulations. The match in blue shift morphology between experiment and simulations confirms that the spectral phase at focus is the same at that measured by the FROG, which samples the beam after propagation through a vacuum window and a collimating lens. The energy of the simulated pulses, except where noted, was chosen to match the experimentally determined peak fluence of 200 $\mathrm{J/cm^2}$.

The effect of density is shown in Figure 5.5. In Figure 5.5(a), the blue shifting resulting from the simulated density profile in Figure 5.4 is shown, while in Figure 5.5(b) the simulated density is lowered by 50% to $n_{He} = 6.5 \times 10^{17}\,\mathrm{cm}^{-3}$. Lowering the density results in a noticeable reduction in the maximum spectral shift, consistent with expectations from Eqn. 2. This effect is observed at other energies as well. Because the magnitude of spectral change is moderate, as seen by the small change in the 2% threshold for a large (50%) change in density, it is expected that the much smaller errors on the density measurement are not a significant source of error in matching simulations to measured spectra.

The dependence on energy is demonstrated in Figure 5.6, in which measured spectra (individually normalized to their peak intensity) in Figure 5.6(a) are compared with simulations of 27 mJ pulses (matching the measured pulse's peak fluence) in Figure 5.6(b). Simulations with 45 mJ shown in Figure 5.6(c) underestimate the fraction of energy in the blue shifted region, based on the 2% intensity profile. Simulations with 15 mJ shown in Figure 5.6(d) show an underestimation of the spectral shift. The temporal profile/spectral phase of the simulated pulses is taken from FROG measurements and is not varied to optimize the fit with the measured spectra. The solid lines indicate the smoothed contour at 2% of peak intensity of the spectrum. These simulations show that simulated pulses with energy (and thus fluence) too high/low lead to an over/under-estimation of the spectral shift, based on the location of the 2% intensity profile, and mismatch in qualitative morphology with the measured spectra.

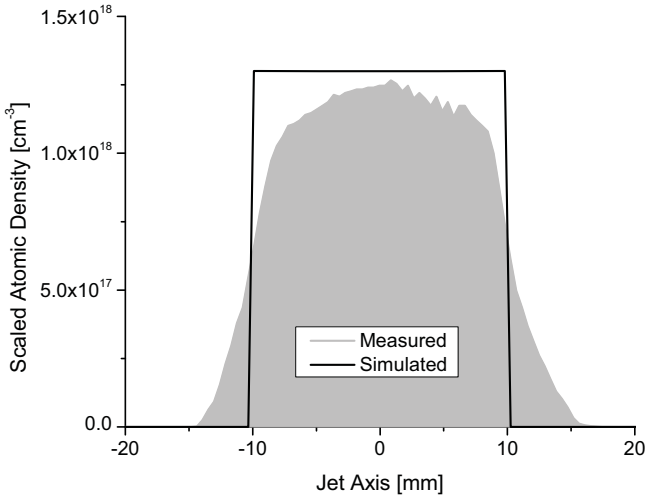

Figure 5.4: The measured on-axis density from the 1.5 cm slit jet a distance 10 mm away from the jet outlet is shown in grey scaled to the backing pressure used in the blue shifting experiment. The simulated density profile, with the same FWHM and integrated density is shown in black.

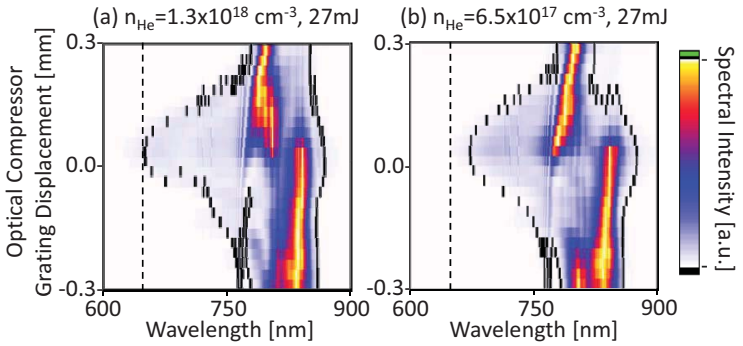

Figure 5.5: Simulated blue shifted spectra from 27mJ pulses as a function of compression at (a) the measured density ($n_{He} = 1.3 \times 10^{18}\,\mathrm{cm}^{-3}$) and (b) 50% lower density ($n_{He} = 6.5 \times 10^{17}\,\mathrm{cm}^{-3}$). The solid lines indicate the 2% intensity level for each of the individually normalized spectra. The dashed lines indicate the maximum extent of blue shifting for the $1.3 \times 10^{18}\,\mathrm{cm}^{-3}$ case.

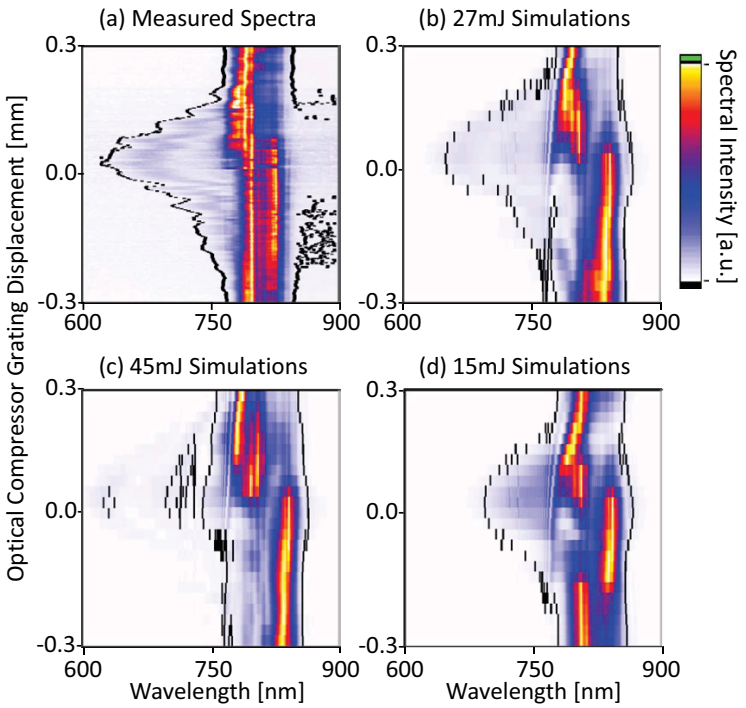

Figure 5.6: (a) Measured normalized spectra as a function of optical compressor grating spacing. (b) Simulated 27 mJ pulses, which show the closest match to the measured spectra. (c) Simulated 45 mJ pulses underestimate the fraction of energy in the blue shifted light while (d) simulated 15 mJ pulses underestimate extent of spectral shifting. The solid lines indicate the 2% intensity level for set of spectra.

Known dispersion was added to the ionizing laser to investigate limits on the sensitivity of this technique to different orders of phase. The total phase of the laser including the added dispersion is known, because the laser's initial phase (without added dispersion) was determined by multiple FROG measurements at various grating spacings and the dispersions add linearly to this. Spectral dispersion was introduced with a Fastlite DAZZLER acousto-optical modulator [81]. The optical compressor grating spacing was varied, in addition to the fixed dispersion from the DAZZLER, and the resulting blue shifted spectra of ionizing pulses were measured to determine their morphology. The optical compressor varied pulse length from a (measured) minimum of 34 fs to a (calculated) maximum of 120 fs in the absence of added dispersion. A scan of grating spacing is shown in Figure 5.7(a), and the matching simulations of 27 mJ pulses with the same initial phase is shown in Figure 5.7(b). Their agreement for this and other introduced dispersions (see Figures 5.8 and 5.9) indicates the validity of the model in this regime. An iterative algorithm to determine the best-fit spectral phase would allow determination of the initial phase from measured blue shifted spectra, but its application is constrained by the computational resources required for simulating

laser propagation including ionization defocusing. Agreement and sensitivity to blue shifting morphology is thus limited to changes in spectral phase that produce gross effects in the blue shifted morphology.

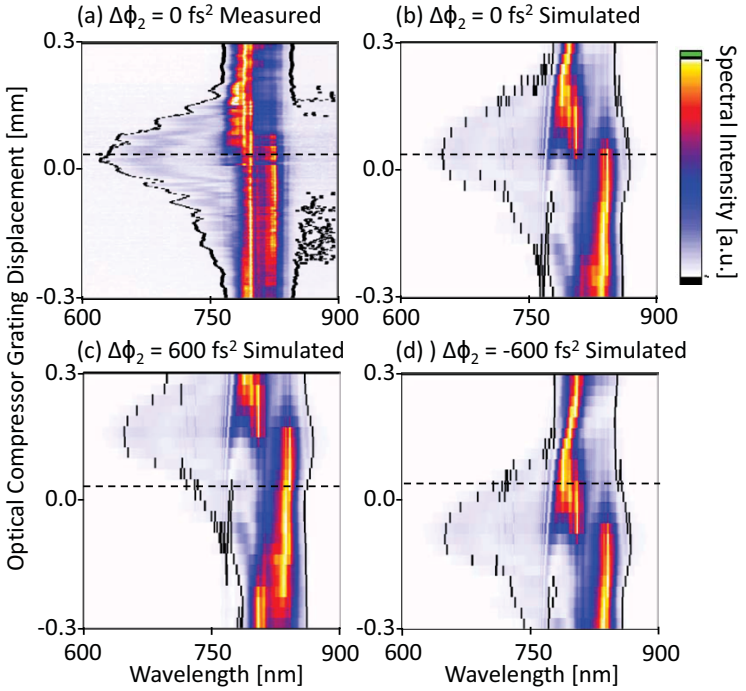

Figure 5.7: Normalized blue shifted spectra from a pulse with varying optical compression without added dispersion (a) measured at BELLA and (b) simulated with the same measured spectral phase. Mismatched simulations with (c) +600 fs^2 or (d) -600 fs^2 of added second order dispersion to demonstrate the sensitivity of the technique. The solid lines indicate the 2% intensity level for each spectrum, and the dashed line indicates the position with the maximum blue shift in the measured spectra.

To quantify the morphology's sensitivity to phase it is necessary to establish a metric for quality of fit. The relevant qualitative features of the shifted spectra vary with the specifics of the experiment. For blue shifting in the gas jet, the relevant features of the morphology are the range of compression that gives blue shifting and the shape of the spectrum. Based on these features, sensitivity to dispersion can be established for each order by determining the minimum change required for a subjective change in the morphology. As an example of the technique's sensitivity to second order phase, mismatched simulations are shown in Figs. 5.7(c) and 5.7(d). The blue shifted spectral pattern shifts up or down, respectively, relative to the compressed location for pulses without added dispersion, but the spectral morphology stays unchanged apart from the shift. In contrast, the spectral morphology changes dramatically with third order dispersion, as shown in Figure 5.8(a) and its matching simulation Figure 5.8(b). Adding less third order phase as in Figure 5.8(c) or more third

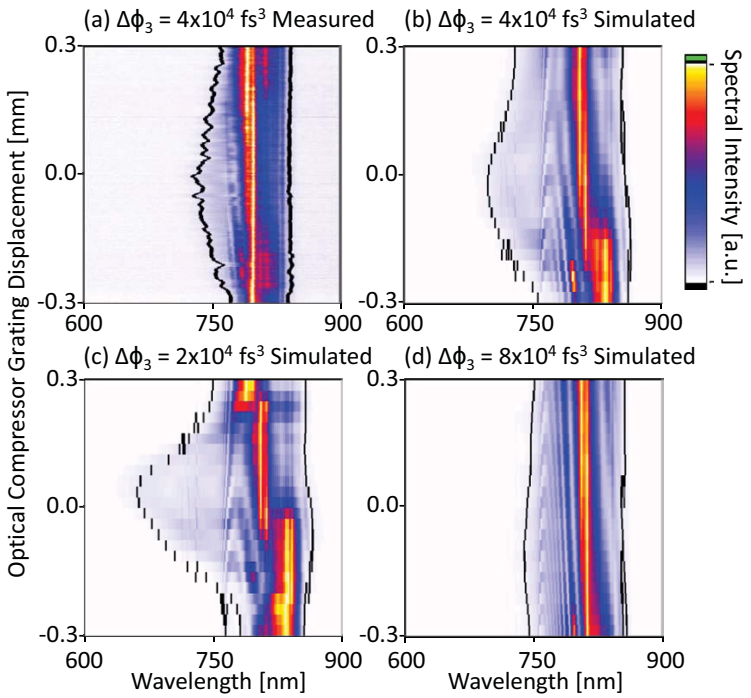

Figure 5.8: Normalized blue shifted spectra from a pulse with added third order spectral dispersion (a) measured at BELLA and (b) a simulation with same added initial spectral phase $\Delta\phi_3 = 4 \times 10^6\,\mathrm{fs}^3$. Mismatched simulations with (c) less dispersion $\Delta\phi_3 = 2 \times 10^6\,\mathrm{fs}^3$ and (d) more dispersion $\Delta\phi_3 = 8 \times 10^6\,\mathrm{fs}^3$ show the changes in spectral morphology with third order dispersion. The solid lines indicate the 2% intensity level for each spectrum.

order phase as in Figure 5.8(d) causes large changes in the spectral morphology, shown by the maximum blue shifted wavelength and the contour of the 2% intensity level. This establishes bounds on the sensitivity of the technique to third order phase. The spectral phase which gives the best agreement to the measured spectra appears to be between $\Delta\phi_3 = 4 \times 10^6\,\mathrm{fs}^3$ shown in Figure 5.8(b) and $\Delta\phi_3 = 8 \times 10^6\,\mathrm{fs}^3$ shown in Figure 5.8(d). The addition of fourth order phase significantly changes both the spectral morphology and the grating location that gives the largest blue shift. The measurements in Figure 5.9(a) and the matching simulation in Figure 5.9(b) show that blue shifting occurs at a different location and over a wider range of compressor grating spacings compared with Figs. 5.9(c)/5.7(b), which has no added dispersion. The disagreement of simulations Figs. 5.9(c) and 5.9(d) with the data, in comparison with the agreement between Figs. 5.9(a) and 5.9(b), shows how well the fourth order sensitivity can be determined. Conservative limits for sensitivity to each order of spectral phase based on fits to the gas jet blue shifted spectra are summarized in Table 5.1.

An iterative algorithm to guess a spectral phase, simulate it for several values of compression, and compare the results with experiment would allow direct determination of the initial phase from the blue shifted measurements, but its application is constrained by the

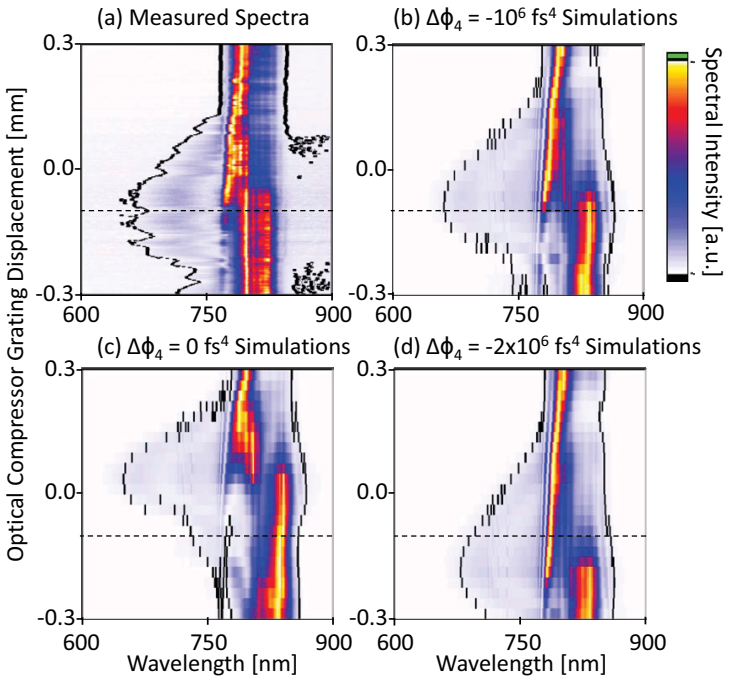

Figure 5.9: Normalized blue shifted spectra from a pulse with added fourth order spectral dispersion (a) measured at BELLA and (b) a simulation with same added initial spectral phase $\Delta\phi_4 = 10^6\,\mathrm{fs}^4$. Mismatched simulations to demonstrate sensitivity with (c) less dispersion $\Delta\phi_4 = 0\,\mathrm{fs}^4$ and (d) more dispersion $\Delta\phi_4 = 2\times10^6\,\mathrm{fs}^4$ differ in the morphology of the blue shifted spectra. The solid lines indicate the 2% intensity level for each spectrum, and the dashed line indicates the position with the maximum blue shift in the measured spectra.

Table 5.1: Blue shifting sensitivity to spectral dispersion based on simulated scans of grating spacing

Phase Order	Uncertainty
2^{nd}	$\pm 600 fs^2$
3^{rd}	$\pm 4\times10^4 fs^3$
4^{th}	$\pm 10^6 fs^4$

computational resources required for simulating the laser's self-consistent propagation. In the absence of such a method to determine the best fit to a given set of blue shifted spectral measurements, the sensitivity of blue shifting morphology is limited to changes in spectral phase that produce gross effects in the blue shifted morphology (Figures 5.7 and 5.9). The ability to set conservative limits such as those noted in Table 5.1 is still sufficient to crosscheck the spectral phase at laser focus/target measured by a second diagnostic at another location, such as FROG or SPIDER, or to provide a day-to-day consistency check of spectral phase.

In summary, a new technique is proposed for verifying the high-order spectral phase of a laser system based on the morphology of ionization blue shifting in a known gas target as a function of compression. The blue shifted spectra for different pulse compressions are straightforward to measure, and this technique allows characterization of the spectrum in-situ at the high-power laser's focus, making it particularly suited for laser plasma acceleration studies. The orders of the laser's spectral phase have distinct effects on the spectral morphology and can be tested via numerical simulation of the process given a known target density. This is demonstrated by agreement between simulations and data from BELLA.

5.2 Experimental Density Profile from Red Shifted Spectra

The spectrum of the laser after interacting with the gas jet target is a very sensitive probe of the target density. The primary effect is red shifting and modulation of the spectrum due to the plasma wake. In the experiment, the BELLA laser spectrum was measured for a range of vacuum focal locations by translating the gas jet along the laser axis. Simulations of the laser propagating through the gas jet were done using the 2D-cylindrical particle-in-cell envelope code INF&RNO [15–17] to verify that the experimental results were consistent with the density determined from tomography. Each set of simulations produced laser spectra as a function of vacuum focal location for a fixed laser temporal profile, spatial profile, and density profile. The simulated laser spectra include the effect of the off-axis collection area of the spectrometer in the experiment and are multiplied by the measured spectrometer collection efficiency and sensitivity, which allows direct comparison with the measured experimental results. The spatial profile of the laser was determined by phase retrieval [34] from images of the laser vacuum mode at a range of locations, and the temporal profile was determined via FROG measurements [29]. The shape of the simulated density profile was a 6.0 order 18 mm length (FWHM) super-Gaussian distribution based on the tomography results, and the absolute density of the distribution was varied to find the best match with the measured spectra.

The spectra resulting from different longitudinal profile plateau densities shown in Figure 5.10. The measured laser spectrum is shown in Figure 5.10(a) as a function of vacuum focal location (negative indicates a vacuum focal location upstream of the center of the gas jet nozzle). There are no measured spectra below -10 mm which is why the plot is uniform in

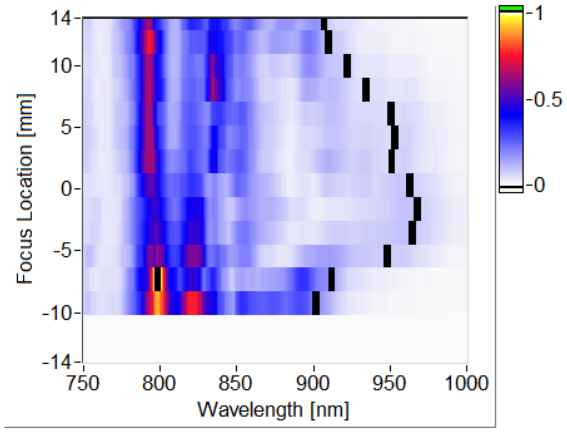

(a) Measured spectra of the laser after interaction with the gas jet, for a range of vacuum focal locations relative to the jet center

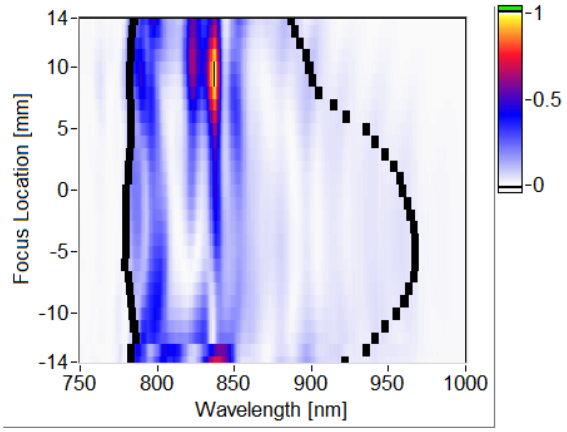

(b) Simulations of density $n_{atomic} = 4.35 \times 10^{17}$ cm^{-3} show similar morphology to measured spectra

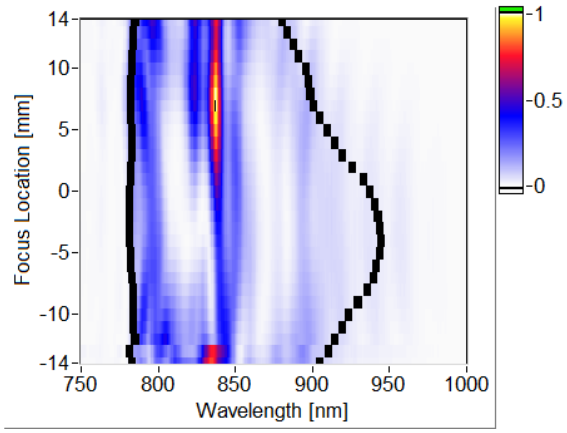

(c) Simulations of density $n_{atomic} = 4 \times 10^{17}$ cm^{-3} exhibit less red shifting than measurements

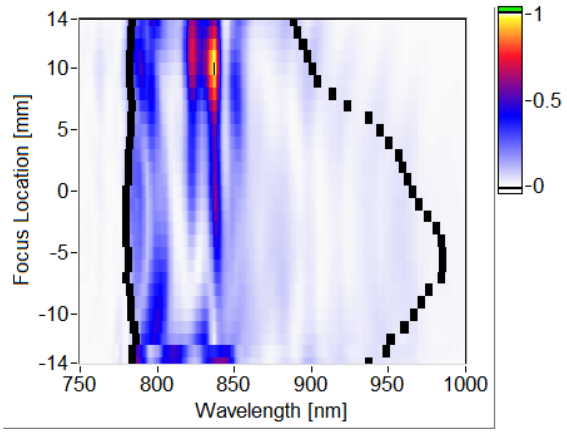

(d) Simulations of density $n_{atomic} = 4.5 \times 10^{17}$ cm^{-3} exhibit more red shifting than measured

Figure 5.10: Best match between measured laser spectra after the gas jet and simulation results, using the profile from tomography scaled to various densities, indicates the plateau density in the experiment.

this region. The black lines indicate the wavelength beyond which the remaining spectrum contains 5% of the total energy. The scaled density profile which gave the best match to the measured spectra was $n_{atomic} = 4.35 \times 10^{17}$ cm^{-3}, shown in Figure 5.10(b). Decreasing the density as in Figure 5.10(c) gives spectra that have less red shift than measured. Increasing the simulated density to $n_{atomic} = 4.5 \times 10^{17}$ cm^{-3}, which is still below the result from tomography, increases the maximum red shifted wavelength and the 5% energy boundary more than those of the measured spectra. This case is shown in Figure 5.10(d).

A caveat to the plots in Figure 5.10 is that the simulated focal position that gives the maximum red shift is shifted relative to the measured spectra. The uncertainty in determining the vacuum focal position in the experiment, which sets the y-axis offset for Figure 5.10(a), is $\sim \pm 1$ mm. Other possible causes of difference in the focal position with maximum red shifting are uncertainty in the spectrometer filter calibration and the phase retrieval of the laser spatial mode, which could introduce a shift in vacuum focal location.

Final Density Calibration

Based on this comparison with simulated laser spectra, the density of the gas jet along the laser axis was $n_{atomic} = 4.35 \times 10^{17}$ cm^{-3}. For the remainder of this thesis, this is the value of density which will be used along with the shape of the distribution from the tomographic reconstruction, since it is based on a match to the experiment. The result from tomography was a peak density of $n_{atomic} = 5.1 \pm 0.45 \times 10^{17}$ cm^{-3}, based on a super-Gaussian fit, and so the disagreement between the two is slightly larger than the estimated uncertainty in the tomographic result. A possible cause of the density difference is heating/cooling of the gas jet. The difference between the best match to simulations and the tomographic reconstruction corresponds to a 20°C rise in temperature, based on the gas jet model presented in Appendix A. The jet is cooled by a flow of water through the copper jacket (see Figure 3.1(b)) and through heat conduction to its mount. In the experiment, the jet was mounted by a single screw shown in Figure 5.11(a) to a thin anodized bracket. For the tomographic measurements, the jet was mounted by a block of aluminum which was in contact with approximately 1/4 of its circumference, as shown in Figure 5.11(b), which would conduct heat away from the jet much more efficiently.

The final density calibration of the gas jet consists of three components: the steady-state density result of $n_{atomic} = 4.35 \times 10^{17}$ cm^{-3} based on simulations (corresponding to 300-500 seconds in Figure 3.4(a)), the shape of the distribution given in Table 3.1, and the exponential decay of Figure 3.4(a) which gives the scaling factor for this density as a function of time, described by Eqn. 3.3. There is also a correction to the plateau height and decay rate due to jet repetition rate, as shown in Figure 3.4(d). As demonstrated in Figure 3.5, the jet reproducibly recovers to an initial starting condition once it has been turned off for 6 min or longer. Thus the gas jet has been characterized for steady state operation and for the case when the jet is turned on at the start of data acquisition after not a period of not firing of $\gtrsim$6 min.

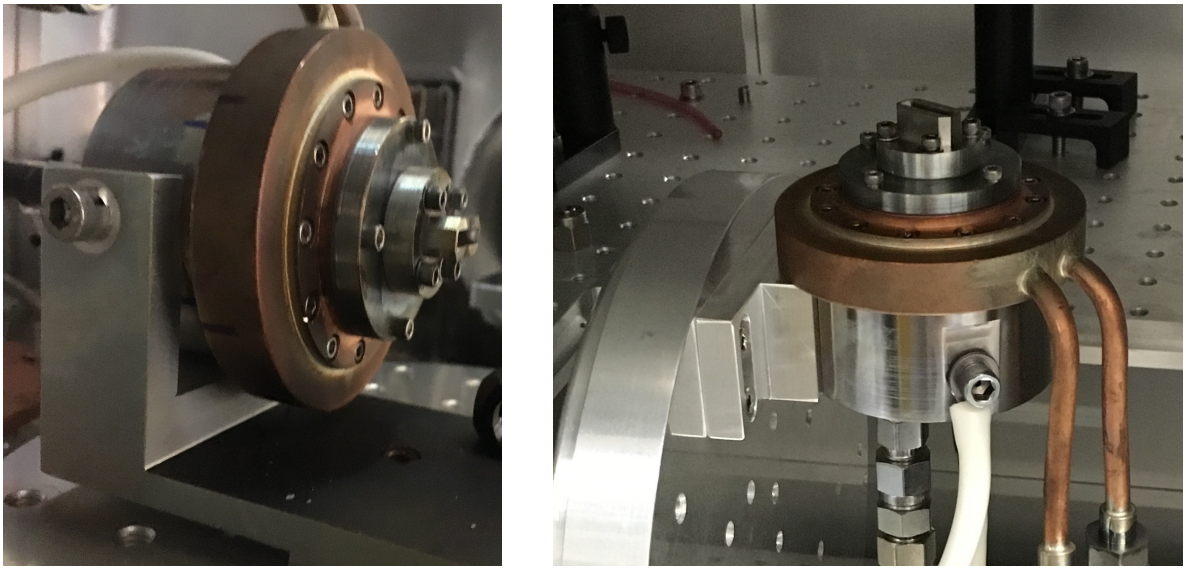

(a) Jet mount for LPA experiment (b) Circumferential jet mount for interferometry

Figure 5.11: Different jet mounting brackets for laser plasma accelerator experiments and for interferometry/tomography measurements.

The scaling of the density distribution as a function of time after activation and repetition rate is

$$n(t) = \left[p + (1-p)e^{-t/(56\pm11\text{ s})}\right] n_{max} \tag{5.2}$$

where $n_{max} = n_0/(0.835\pm0.005)$ is the density when the just is first turned on, $n_0 = 4.35\times10^{17}$ cm^{-3} is the steady-state operation density at 410µs delay for 1 Hz 300 V operation, and p is the plateau fraction which is the fractional decrease from the initial density immediately after turn on to the steady-state operation density. The factor p comes from a linear fit to the phase in Figure 3.4(d) and is given by

$$p = [1 + 0.21(1-f)](0.0835 \pm 0.005) \tag{5.3}$$

where f is the repetition frequency of the gas jet. For $f = 1$, this recovers the formula of Eqn. 3.3. The density gradients shown in Figure 3.14(a) and in Figure 3.14 can likewise be scaled by the ratio $n(t)/n_{tomo}$ where $n_{tomo} = 5.1 \times 10^{17}$ cm^{-3} is the peak density based on tomography alone.

5.3 Concluding Remarks

In this chapter, diagnostics were presented based on spectral shifting of an ultrafaset laser pulse which provide information about both the laser itself and the plasma target of an LPA system. The temporal profile of the laser, independently determined in Chapter 2,

was constrained by the ionization blue shifting of the pulse spectrum and its variation as a function of pulse compression. The density profile experienced by the laser in the pulse front tilt experiments was verified by determining the scaled density profile which agreed with the measured red-shifted laser spectra. These results will be used in Chapter 6 as the input for simulations used to explained the observed experimental trends.

Chapter 6

Pulse Front Tilt Experiments

Experiments were conducted at the BELLA Center to explore the effects of various spatiotemporal couplings on laser plasma acceleration. The experiment consisted of three elements: optimization of the laser plasma accelerator (LPA), baseline accelerator operation, and accelerator operation with a spatiotemporal distortion of the drive laser. The laser driving the LPA was the BELLA PW Laser operated at an energy at target of 13.5 J. The acceleration target was the supersonic gas jet whose density profile was described in Chapter 3.

The laser plasma accelerator was optimized (without any spatiotemporal coupling of the drive laser) to ensure sensitivity to the effects of pulse front tilt. The primary effect of pulse front tilt on laser plasma acceleration is deflection of the drive laser and steering of the accelerated electron beam (see Chapter 4), so the LPA was tuned for electron pointing stability. The gas jet trigger timing relative to the laser arrival time, transverse distance from the optical axis, and longitudinal position relative to the laser vacuum focal location were optimized to minimize the fluctuation in pointing direction of the accelerated electrons, as well as to ensure sufficiently large accelerated charge for an accurate pointing determination. The LPA was then characterized to provide a performance baseline for comparison with pulse front tilt experiments.

The spatiotemporal distortion of the LPA-driving BELLA laser was adjusted by rotation and displacement of the optical compressor diffraction gratings. The effects of adjustments to the grating angle and position were measured and discussed in Chapter 2. Angular chirp was added to the driving laser pulse by rotating the diffraction gratings of the final optical compressor orthogonal to the dispersion plane (clocking). The presence of angular chirp resulted in pulse front tilt which varied as a function of propagation. The residual group delay dispersion (GDD) of the pulse after compression was modified by changing the spacing of the optical compressor diffraction gratings. The pulse front tilt profile as well as the temporal profile of the laser pulse were significantly modified by the addition of GDD.

Electron Beam Diagnostics

The accelerator system incorporates a variety of laser and electron beam diagnostics characterize LPA operation and performance. After the LPA the accelerated electrons and the remaining driver laser are separated, and the electron energy, charge, and spatial distribution are measured. The three diagnostics of the electron beam properties are the magnetic spectrometer which gives the distribution of electron energies, the imaging phosphor screen which gives the electron charge and charge distribution, and the integrating current transformer (ICT) which gives an independent measurement of the beam charge. The accelerated electrons pass through the three electron diagnostics in series. After the LPA the electron beam must pass through the 1 in. (25.4 mm) diameter hole in the first telescope optic. Next it passes through a hole of the same size in a laser calorimeter and through an optically reflective foil, to eliminate any remaining laser light. The electron beam then strikes the imaging phosphor, if it is inserted, and passes through the ICT ring. Because the electron beam must pass through a series of apertures, the acceptance of the the electron beam diagnostics is limited to ± 1.2 mrad (4.5 µsr of total solid angle), and as a result of this limited acceptance apertures many electron beams from these experiments were partially obscured (clipped). The final electron diagnostic, the magnetic spectrometer, has an vertical entrance slit which improves the energy resolution of the spectrometer but this does not affect the other diagnostics.

The imaging phosphor screen is an insertable fast LANEX phosphor screen, which phosphoresces when x-rays or high-energy charged particles pass through it, that is imaged onto a camera. The phosphorescent light emitted by the screen is proportional to the local charge density of the electron beam, and so the phosphor screen yields an image of the spatial charge distribution of the electron beam. The phosphor screen is inserted before dispersion by the magnetic field of spectrometer, so the entire electron beam is imaged rather than a particular energy band. This charge distribution yields both the beam pointing, from its center location, and divergence, from its spread.

The integrating current transformer is a many-winding solenoid that acts as a transformer with the electron beam acting as the primary coil [82, 83]. A short (few-fs) relativistic electron bunch passing through the ICT induces a DC voltage in the coil, and the integral of this voltage pulse is logarithmically proportional to the total charge of the electron bunch. The ICT charge calibration was cross-checked against the charge measurements from the insertable imaging phosphor, and they were found to agree in most operational regimes [84]. The ICT is 20 cm closer to the magnetic spectrometer than the phosphor screen, so very low energy electrons may strike the phosphor and be deflected away from the ICT by the fringe fields of the magnetic spectrometer. For this reason, there may be a small discrepancy between the two charge measurements if the electron beam energy distribution has a large low energy tail.

The magnetic spectrometer consists of a variable-strength electromagnet (0-1.6 T) with a soft iron yoke and three fast LANEX phosphor screens. Electrons are dispersed downward by the dipole field as well as weakly focused in the other axis. Because higher energy particles have a larger bending radius for the same magnetic field, higher energy electrons are deflected

less than lower energy electrons. The momentum (and thus energy) of the electrons can be determined from their recorded deflection. The deflected electrons are recorded by the three fast LANEX screens which are imaged onto cameras.

6.1 Electron Beam Pointing Analysis

An analysis of the spatial charge distribution of the accelerated electrons was performed to determine the pointing and approximate size of the electron beams. Many of the electron beams were partially or completely blocked because of the apertures that the beams must pass through before being recorded by the phosphor screen. However, the spatial distribution of the accelerated electrons was always roughly elliptical. Using this *a priori* knowledge an analysis technique was developed to extract a position and size for partially obscured beams.

The electron beam pointing analysis consisted of fitting an ellipse to the edge of the thresholded charge density. A false color image of a typical charge distribution is shown in Figure 6.1(a). First, the image is set to zero wherever the charge density is below a specified threshold, either a fraction of the image's peak or a fixed charge density. In Figure 6.1(b) the false color image is shown after a threshold of 60% of the peak has been applied. Next, the region above the threshold value was made uniform (Figure 6.1(c)). The image was then smoothed applying a 5x5 low pass filter and then thresholding the filtered image at a value of half the uniform fill value (see Figure 6.1(d)). For images with a low signal-to-noise ratio, the thresholding process results in many disconnected regions (see Figure 6.1(e)), and the smoothing process significantly reduced the complexity of the resulting shape while maintaining the overall size and shape of the profile (see Figure 6.1(f)). The edge of the shape was extracted and the section of the intensity contour resulting from the aperture was removed if the beam was clipped, as seen in Figure 6.1(g). The points of the edge were fit to an ellipse with a bisquare weighting scheme to reduce the influence of outliers (see Figure 6.1(h)). The center of the fitted ellipse was taken to be the center of the electron bunch, and the ellipse's axes were taken as measures of the beam size. The electron beam pointing angle was calculated from its position relative to the optical axis, as in Eqn. 6.2 but using the distance of the phosphor to the target indicated in Figure 1.3.

The effects of different thresholding schemes and threshold levels were investigated by varying the vertical transverse offset between the driver laser and the gas jet target. The resultant deflection of the laser and electron beam is approximately linear with positive slope as a function of transverse offset. This agrees with ray tracing predictions of the laser for offsets much less than the transverse size of the jet plume ($\sim$4 mm full width at half maximum). The results are shown in Figure 6.2(a), with the maximum aperture acceptance indicated by the dashed lines. The ends of each profile is marked with filled circles. The retrieved pointing trend is independent of threshold for results within the aperture (provided that the threshold is sufficiently high, as is the case for all plots shown). The threshold was specified as a percentage of the peak charge density because the charge of the electron beam, shown in Figure 6.2(b), varies with transverse offset. Error bars in Figure 6.2(b) and the

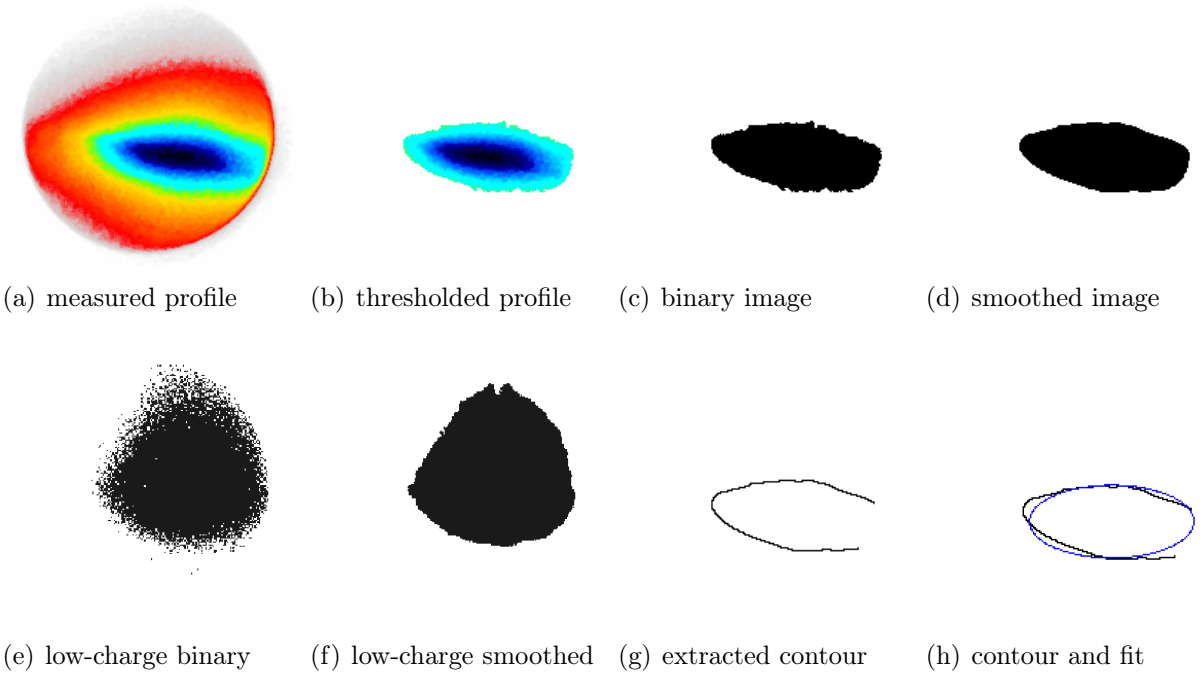

(a) measured profile (b) thresholded profile (c) binary image (d) smoothed image

(e) low-charge binary (f) low-charge smoothed (g) extracted contour (h) contour and fit

Figure 6.1: Steps of electron beam pointing analysis.

remainder of the chapter represent 95% confidence intervals on the value of the mean.

The pointing trends in Figure 6.2(a) plateau at a fixed value when the electron vertical angle becomes close to the acceptance aperture of the diagnostic (dashed lines). This is non-physical and due to clipping of the electron beam mode by the finite acceptance aperture of the phosphor screen diagnostic. Since the aperture is circular, a radial metric of beam position is appropriate to determine which electron beams are too clipped and therefore should be excluded from the analysis. The radial offset of the electron beam center is given by

$$\theta_r = \sqrt{\theta_x^2 + \theta_y^2} \tag{6.1}$$

where the position is expressed as an angle by Eqn. 6.2. This is a zenith angle, as it indicates absolute angular deflection from the optical axis. These parameters are illustrated in Figure 6.3(a), where the black ring represents the aperture, the shaded region represents the detected electron beam, and the blue oval represents the portion of the elliptical fit within the acceptance aperture. $\Delta\theta_x$ and $\Delta\theta_y$ are the angular size of the electron beam (the semi-axes of the elliptical fit). The radial position/zenith angle of electron beams for a range of laser transverse vertical offsets is plotted in Figure 6.3(b). The plateau in vertical pointing corresponds to electron beams with calculated positions outside the aperture of the phosphor diagnostic.

A relative threshold value of 70% of the peak charge density will be used for analysis of

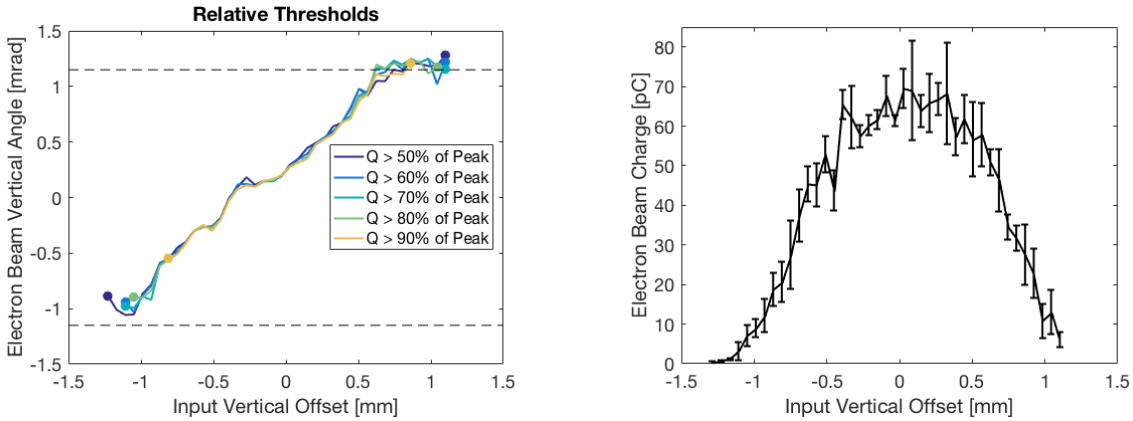

(a) Pointing trend for different thresholds (as fractions of peak charge density)

(b) Electron beam charge decreases with transverse offset, due primarily to clipping.

Figure 6.2: Effect of thresholding on electron beam position analysis.

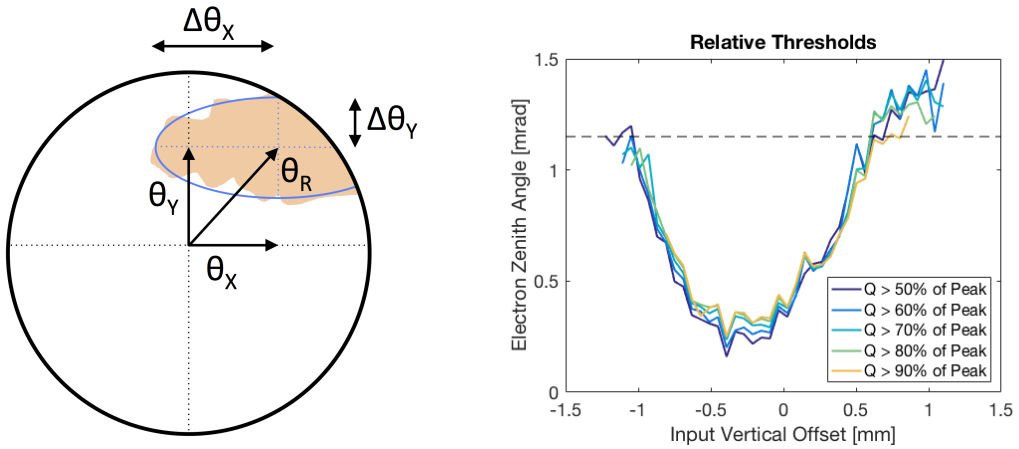

(a) Electron fit parameters.

(b) Electron beam radial position (zenith angle) as a function of input offset.

Figure 6.3: Electron radial position/zenith angle illustrated schematically and plotted as a function of transverse offset

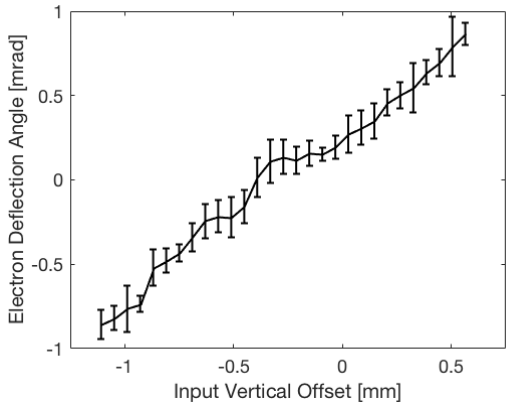

Figure 6.4: Laser and electron beam pointing trends using threshold level and filling method described in text.

the experimental electron pointing data, and any electron beams with $\theta_r \geq 1.15$ mrad, the acceptance aperture of the phosphor diagnostic, will be discarded. The threshold value was chosen because the electron beam pointing is insensitive to threshold value at this point, as demonstrated in Figure 6.2(a). Electron beams with θ_r larger than the acceptance aperture of the phosphor diagnostic will be discarded because this indicates the electron beam the position determination is not reliable. The electron beam pointing trend as a function of transverse vertical offset analyzed by these methods is shown in Figure 6.4 in black.

High Power Laser Diagnostics

In addition to the electron beam diagnostics, a variety of laser measurements are made of the input and transmitted laser pulse to gain information about the laser-plasma interaction. There are three primary laser diagnostics after the LPA interaction: the near-field imaging system, the optical spectrometer, and the far-field imaging system. The all-reflective telescope for the far-field diagnostic consists of an uncoated wedged optical flat with a hole, three uncoated curved optics, a flat window, two flat uncoated optics, and several silver-coated flat mirrors. The first optic separates the laser reflection from the electron beam and has a 1 inch (2.54 cm) hole centered at the optical axis to allow the electron beam to continue straight without passing through material. After the experiments presented in this thesis, the imaging system was upgraded so the first optic could be shifted to either center the hole, allowing electrons through, or offset the hole outside of the laser near-field mode. Since the optic is uncoated, only $\sim$4% of the incident light is reflected from the front surface for imaging. The second optic is an uncoated concave spherical surface ($f = 3736.5$ mm). The third optic is an anti-reflection coated (front and back) 1 inch (25.4 mm) thick glass optic with ≤ 5 arcmin of wedge that serves as a window separating the vacuum region from air. The fourth optic is an uncoated convex spherical surface ($f = -1848$ mm). The $\sim$4% reflection from the fourth

optic is transported to the far-field diagnostic and the transmitted portion of the laser is used for the laser spectrometer and the near-field diagnostic. The fifth optic is a concave uncoated spherical surface ($f = 4185$ mm), and the remaining optics are all flat.

The far-field imaging camera is located where the all-reflective telescope forms an image of the laser focus. The camera is on an automated translation stage, so the imaging location can be shifted through the focal volume. Without the LPA, it is used to determine the laser focal location by scanning the imaging plane and measuring the peak intensity and beam size versus propagation. It is also used to determine the input laser spatial mode (intensity and phase distribution) as discussed in Chapter 2. In LPA experiments, the far-field telescope was typically set to image the exit of the gas jet so it gave the change in laser mode and transverse position due to the interaction with the plasma.

The near-field imaging system consists of the first four optics of the telescope, a convex lens, an imaging screen, and a fixed camera, shown in Figure 1.3. Since the fourth telescope optic is uncoated, most of the laser light is transmitted. It is then imaged by an $f = 750$ mm converging lens onto a white diffuser screen. A camera with a fixed focal length objective images the screen, and these images give the position and distribution of light on the first optic after the LPA interaction.

Scattered light from the near-field diagnostic screen is collected by a reflective fiber collimator into a multimode fiber, which is connected to a fiber-coupled optical spectrometer. The fiber collimator consists of a reflective silver off-axis paraboloid in a threaded tube, together with an SMA fiber mount. The fiber tip is located at the paraboloid focus, so any light entering the collimator at small angles is efficiently coupled into the fiber. The fiber collimator has a limited acceptance aperture (clear aperture ∼21 mm for the fiber used) which is considerably smaller than the laser size on the imaging screen, so the optical spectrometer samples only an off-axis subsection of the beam (approximately 2 mrad from the laser axis).

6.2 Laser Pointing Analysis

The pointing direction of the laser after the LPA was determined from the near-field imaging system. The distance from the LPA to the optic (10.4 m) is fixed, so the vertical or horizontal angle of the laser is given by

$$\tan\theta_{x,y} \approx \theta_{x,y} = \frac{\text{offset}}{10.4\text{ m}} \tag{6.2}$$

where the offset is the vertical or horizontal component of the displacement between the laser mode and the optic hole.

Corrections for optical distortions needed to be made to the near-field images. The series of optics which images the laser onto the diffuser screen adds aberrations to the image. The diffuser screen itself is not perpendicular to either the imaging optic or camera and objective, so a perspective error is also introduced. These effects were measured by placing a uniform grid of small holes onto the first optic. The distorted image of the holes was recorded (green dots in Figure 6.5(a)), and the image was adjusted by software to correct the distortion

(blue dots in Figure 6.5(a)). Based on the calculated correction, the effect of the imaging aberrations on a (simulated) uniform grid is shown in Figure 6.5(c). The initial undistorted grid is shown in Figure 6.5(b). This analysis also gave a calibration for the diagnostic, since the holes had a 2 cm spacing.

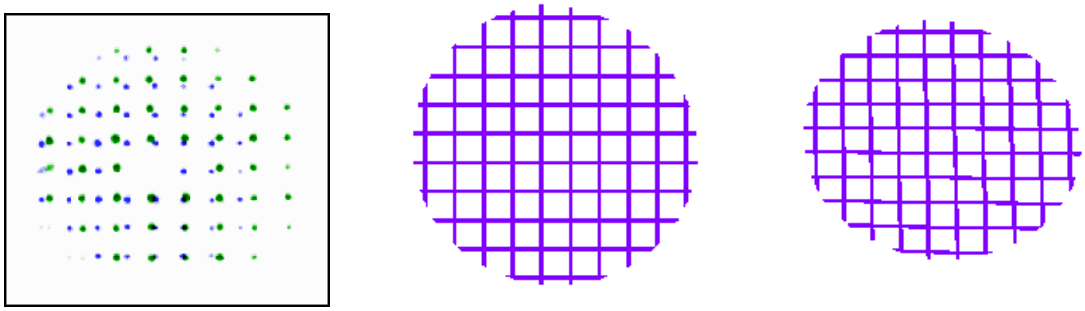

(a) Uncorrected (green) and corrected (blue) images of a uniform grid of holes

(b) Simulated uniform grid with 2 mrad spacing

(c) Effect of near-field imaging system aberration of grid

Figure 6.5: Image distortion from the near-field imaging system.

Several steps were taken to reduce the effect of stray light and noise on the near-field pointing analysis. A background image, taken in the absence of the laser, was subtracted from each near-field laser image to reduce the effect of CCD dark current as well as any damaged pixels. Because the near-field imaging system uses a diffuser screen, it is more sensitive to stray light than other laser diagnostics which directly image the laser. The vacuum mode laser is shown in Figure 6.6(a) in an image from the near-field imaging diagnostic which has been background-subtracted and distortion-corrected. Stray light features with sharp circular edges are visible overlapping the vacuum mode and extending beyond it. These are likely internal reflections from the vacuum window or imaging lens, which are reduced but not eliminated by an anti-reflective coating. Their intensity varies spatially so it is not possible to estimate their level outside the optic-region of the image and subtract their influence everywhere. All areas of the image outside of the first optic were masked (*i.e.*, set to zero) to minimize the effect of stray light on the diffuser screen. Although the intensity is low, these stray light patterns cover a large area of the image, so they may potentially affect the laser position analysis.

A lower threshold (*i.e.*, setting all pixels in an image below a specified value to zero) was implemented in the analysis. Thresholding was used to eliminate the effect of stray light patterns overlapping the image and to select the components of the laser near-field mode which best represent the laser steering. The image of the laser mode consists of light from several sources: the transmitted laser, stray light from internal reflections and back-reflections in the laser diagnostic telescope, forward-directed laser light scattered by the plasma (e.g. by ionization defocusing at the front edge of the pulse) from different longitudinal locations, etc. Under the assumption that the highest intensity features of the mode come

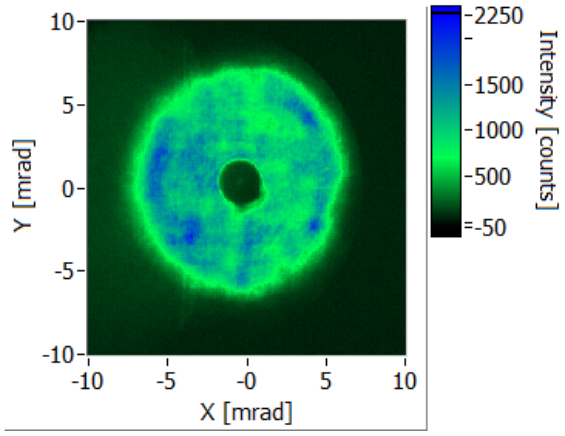

(a) Vacuum laser mode, with stray light patterns

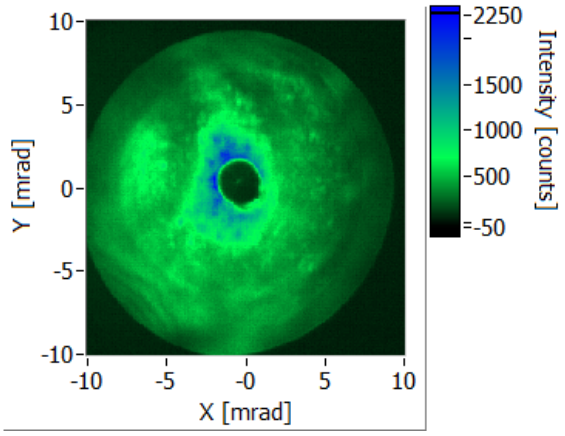

(b) Laser mode after interacting with the plasma

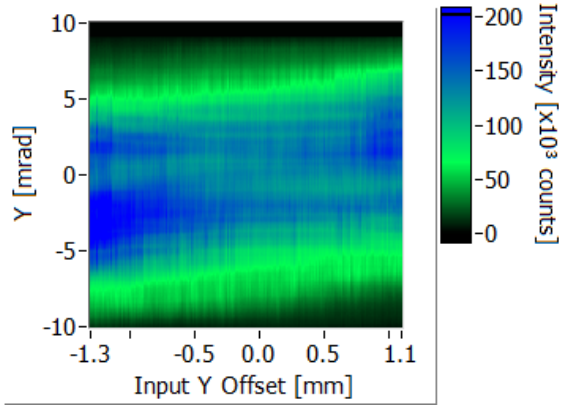

(c) Trend in vertical pointing vs. input laser offset

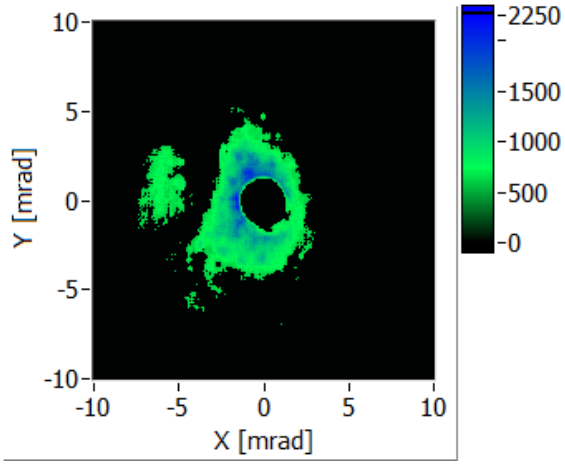

(d) Laser mode from (b) after lower thresholding to 150% of average pixel value.

Figure 6.6: Laser mode with (a) vacuum and (b) gas jet target (plasma). (c) Horizontally integrated laser mode vs. input offset. (d) Laser mode after lower thresholding and effect of hole.

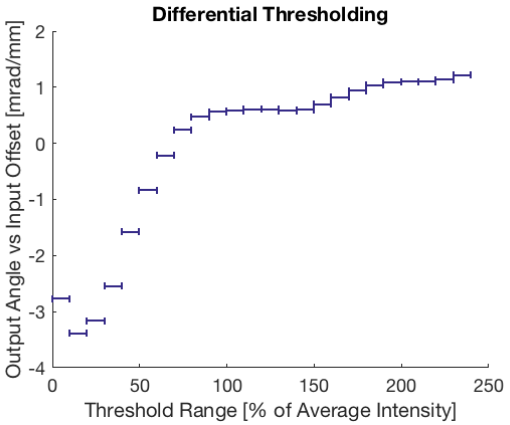

(a) Trend in vertical pointing (slope of linear fit to output laser angle vs. input laser offset) from pixel values in indicated threshold range.

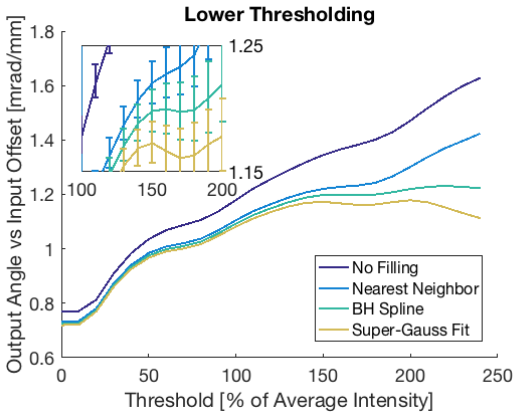

(b) Slope of vertical pointing vs. input laser plotted against lower threshold used for the analysis. Different lines are hole-filling methods. Inset is vertically magnified and shows 50% confidence level.

Figure 6.7: Trend in vertical pointing vs. input laser for different differential and absolute thresholds.

from the transmitted laser pulse, thresholding is an approximate method to isolate light from the transmitted laser and exclude all other sources from the pointing analysis. The near-field image thresholds were specified to allow for varying laser transmission, because the transmitted energy of the laser varies by a factor of several (based on integrated image intensity) over the range of transverse offsets. The absolute threshold was calculated on an image-by-image basis as a fraction of the average non-zero pixel intensity by

$$T_{abs} = T_{rel} I_{avg} = T_{rel} \frac{\Sigma I}{\Sigma p} \tag{6.3}$$

where

$$p = \begin{cases} 1 & I > 0 \\ 0 & I = 0 \end{cases}$$

Thresholding based on a specified fraction of the maximum intensity was also tested, but was found to be unreliable due to its sensitivity to changes in intensity distribution of the laser mode.

To determine the appropriate threshold value, the transverse position of the input laser relative to the jet target was varied by scanning the angle of the last optic before the laser-plasma interaction (see Figure 1.2). The transverse position could be shifted by a significant fraction of the jet width while changing the input laser angle less than 0.3 mrad because the optic is 10.4 m upstream. The effect of varying the input offset is that the output laser shifts linearly as the input offset is varied. This is shown in Figure 6.6(c) in horizontally-integrated

images of the near-field laser mode, which have not had a threshold applied. This trend is consistent with the expectation from linear optics that the laser should deflect away from the center of the plasma, where the density is highest and so the index of refraction is lowest.

Determining the correct threshold value is complicated by the observation that different intensity-components of the laser mode deflect by different amounts as a function of transverse input offset. The calculated output laser pointing trend as a function of differential threshold is plotted in Figure 6.7(a). To calculate a point in this plot, both an upper and lower threshold were applied to the images. The centroid location of the remaining pixels was calculated and by Eqn. 6.2 the output angle was determined for each image. A linear fit was performed to this angle as a function of input position, and so each point is the laser pointing trend (the slope from the fit) for only those pixels in the specified threshold range. Figure 6.7(a) shows that the laser pointing trend is dependent on the threshold value, and pixels with low intensity are anti-correlated with the input offset and overall laser pointing.

The lower threshold level should satisfy the condition that the pointing analysis results do not change if the threshold value is modified. This is desirable from a practical stance because there should be no free parameters to tune the results of the analysis. Physically, the intensity at each pixel is the sum of light from the transmitted laser and from scattered/stray light. Pixels above the correct threshold value get of their intensity from the transmitted, deflected laser pulse, and pixels below the threshold value get most of their intensity from other sources. At the threshold value the contribution from both is approximately equal so adding or removing pixels near this value by making small changes to the threshold should not affect the pointing analysis.

The calculated pointing trend (the slope of the calculated output angle vs. the input offset) after applying various lower threshold levels is plotted in dark blue in Figure 6.7(b). The condition for the correct lower threshold value is that the analysis result should not change with threshold (*i.e.*, the curve should be at a local extremum), but the curve monotonically increases, which means no appropriate threshold level exists. The reason can be seen in Figure 6.6(d) in which the near-field laser mode is shown with a threshold of 150% of the average pixel intensity. At low threshold values, the missing hole in the near-field diagnostic has little influence on the pointing analysis because it is much smaller than the laser mode, but as the threshold is increased the hole becomes a larger fraction of the near-field mode since the most intense part of the laser mode overlaps with the missing region. As a result, the error in the near-field pointing analysis grows with increasing threshold. The effect of the hole in the near-field diagnostic was investigated by numerically filling the hole in the image based on the surrounding laser mode.

Several techniques for numerically filling the hole in the near-field images were tested and compared, shown in Figure 6.8. (Note that the color scales are normalized separately for each image.) The points used in the interpolation of data in the hole-region are shown in Figure 6.8(a). The sampling region was made as small as possible without sampling diffraction from the hole edge or the small damaged region (the ragged region of the edge on the lower right), and the interpolated values were substituted for the interior of the sampled region. The simplest technique tested to fill the hole was nearest-neighbor filling,

shown in Figure 6.8(b). The resulting laser mode is clearly non-physical and the interpolated region cannot contain values higher or lower than those on its border. A biharmonic spline interpolation scheme [85], shown in Figure 6.8(c), gave good qualitative agreement with the laser mode. A rotated bi-super-Gaussian defined by

$$I = a_0 + a_1 \exp\left\{\left|\frac{x'}{L_x}\right|^{p_x} + \left|\frac{y'}{L_y}\right|^{p_y}\right\}$$

where

$$\begin{aligned} x' =& (x - x_0)\cos(\theta) - (y - y_0)\sin(\theta) \\ y' =& (x - x_0)\sin(\theta) + (y - y_0)\cos(\theta) \end{aligned}$$

was also fit to the surrounding points. All variables besides the coordinated x and y were parameters of the fit. A typical result is shown in Figure 6.8(c) where it performs similarly to the biharmonic spline in matching the qualitative features of the laser mode. The fit was constrained with additional data taken from beyond the hole boundary, show as white points in Figure 6.8(c), which adds information about the radial gradients in intensity. However, the laser mode fit cannot match the laser intensity at the boundary since the function has only 9 free parameters.

The laser pointing analysis was repeated using near-field images in which the hole was numerically filled by each method. The results are plotted in Figure 6.7(b) as a function of threshold. All of the hole-filling methods give a lower slope than analysis of the corresponding unfilled images, which indicates the necessity of accounting for the missing energy in the hole. Although no appropriate threshold exists for the unfilled images, both the biharmonic spline and the bi-super-Gaussian fit have local extrema (see inset in Figure 6.7(b)) which occur at/near the correct threshold level for an unbiased analysis. The appropriate threshold value is 160-170% for the biharmonic spline interpolation scheme and 150-170% for the fit. Both methods give similar results near these threshold values, with differences comparable to the uncertainty in the slope fit (error bars in Figure 6.7(b) inset).

The analysis of the experiment will use the biharmonic spline filling technique, with a relative threshold value of 160% of the average intensity in the mode, for analysis of the near-field laser mode. This filling method produces filled images which smoothly match the laser mode at the hole boundary and gives analysis results which only depend weakly on threshold level above the threshold used (*i.e.*, when the hole is filled by this method, all pixels above the threshold value steer in roughly the same direction, without intensity dependence). The results for the scan of input offset using these final analysis parameters are shown in Figure 6.9 along with the electron pointing results. To within error, the laser pointing trend shows zero deflection for no input offset, while the electron beam pointing has an offset of $\sim$0.2 mrad.

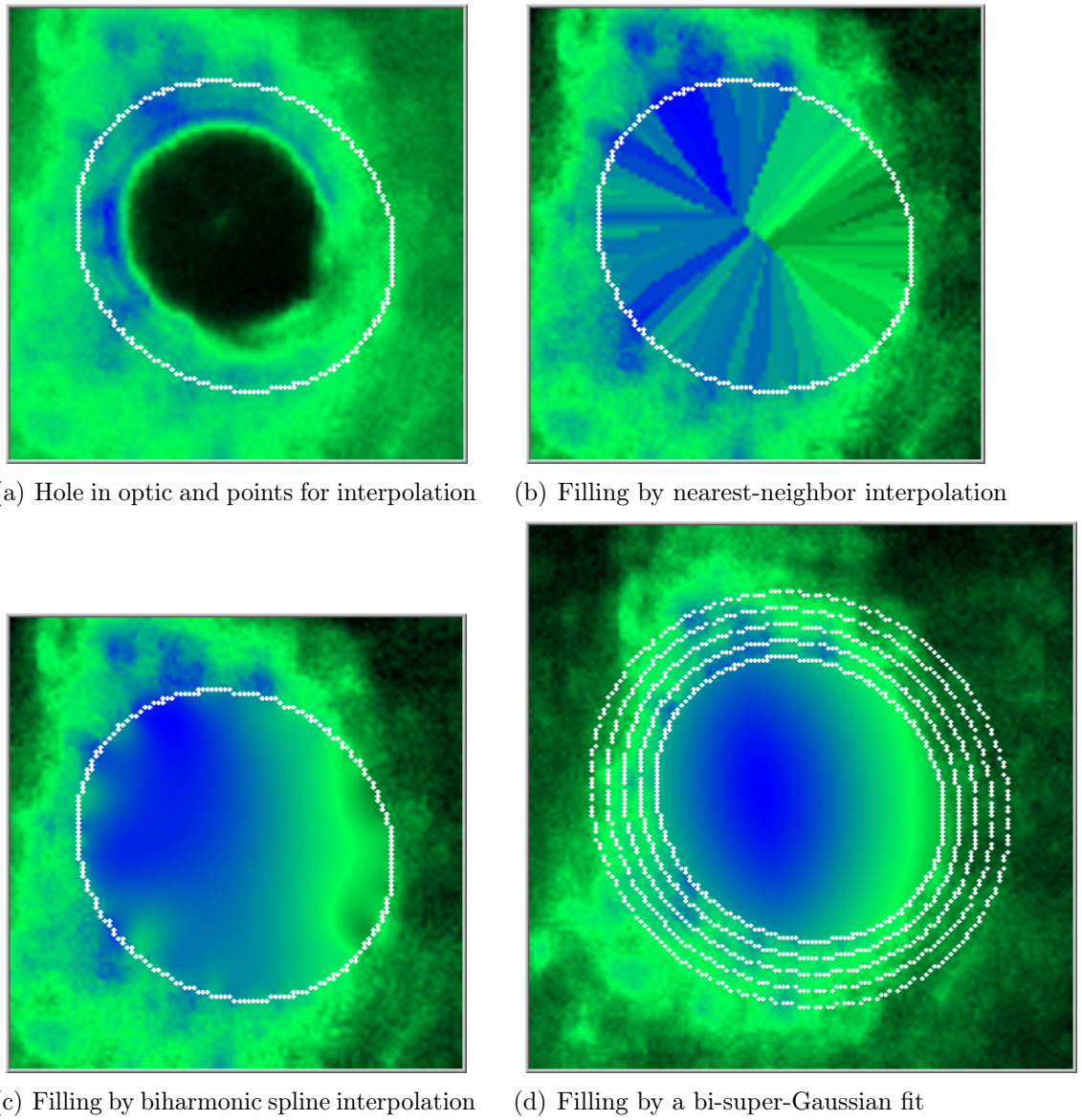

(a) Hole in optic and points for interpolation

(b) Filling by nearest-neighbor interpolation

(c) Filling by biharmonic spline interpolation

(d) Filling by a bi-super-Gaussian fit

Figure 6.8: Several methods of filling the image hole. White points indicate the locations used for the interpolation/fit.

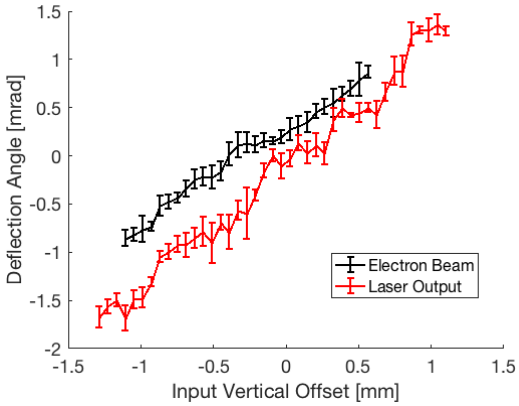

Figure 6.9: Laser (red) and electron (black) pointing using final analysis parameters described in text.

6.3 LPA Baseline Performance and Optimization

Electron beams with stable pointing and charge are necessary to see the effect of added pulse front tilt because these are its primary effects on LPA operation [10]. Relatively high charge is also useful since pulse front tilt tends to reduce the charge from the LPA. The LPA parameters optimized for this experiment were the density profile via the jet orientation, discussed in Chapter 3, the laser spatial mode, the jet timing relative to the laser, and the vacuum focus position of the drive laser. As part of this optimization, a series of measurements were taken to establish a baseline for LPA operation without pulse front tilt.

Laser Spatial Mode

The laser spatial mode was optimized as described in [18]. The focal quality was measured by a wavefront sensor in the Input Diagnostics area, indicated in Figure 1.2, and the adjustments were performed using a deformable mirror (DM), shown in the same figure. The resulting focal spot quality had a Strehl ratio of ~ 0.76, defined here as the energy ratio of a gaussian with the same amplitude and FWHM size to the measured spatial mode at focus.

Laser Vacuum Focus Position

The vacuum focus position was varied to find the regime with the most stable electron beam pointing. Since the vacuum focus is fixed by the off-axis paraboloid (OAP, see Figure 1.2), this was accomplished by translating the gas jet longitudinally. The standard deviation of pointing fluctuations for each vacuum focal location are plotted in Figure 6.11(a) as well as the beam charge. As the vacuum focal location is moved further downstream (the jet is moved towards the focusing optic), the stability increases by a factor of ~ 3 across the range of the jet. However, the charge is maximal when vacuum focus is located in the center of the

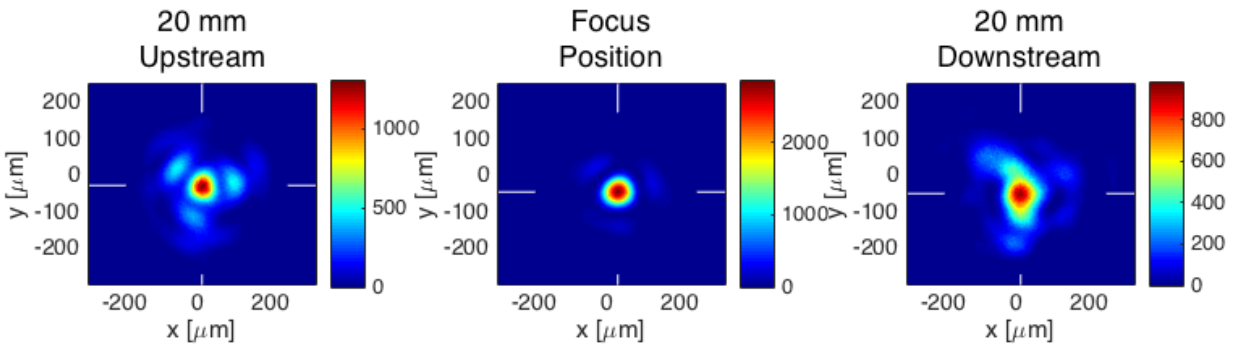

Figure 6.10: Vacuum laser mode after optimization is approximately Gaussian at focus, but develops significantly non-Gaussian features at distances comparable to the gas jet size.

jet. To investigate further, the effect of GDD on the electron beam was measured at two locations: close to the charge peak at the center of the jet (vacuum focus 1 mm upstream of the jet center) and in the stable region with the vacuum focus well downstream of the jet center (vacuum focus 9 mm downstream of the jet center). The results in Figure 6.11(b) show that the downstream focus location gives consistently more stable electron beam pointing as a function of GDD. The downstream focus location was used for the pulse front tilt measurements because of its greater stability, despite the lower charge at this location. In subsequent experiments at the BELLA Center beyond the scope of this work, the electron pointing stability was further improved.

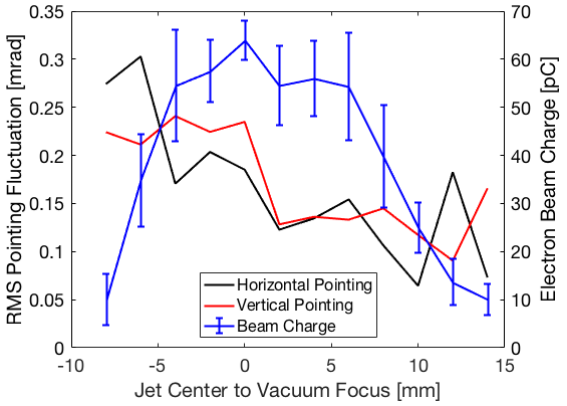

(a) Electron beam pointing fluctuations vs. vacuum focus position

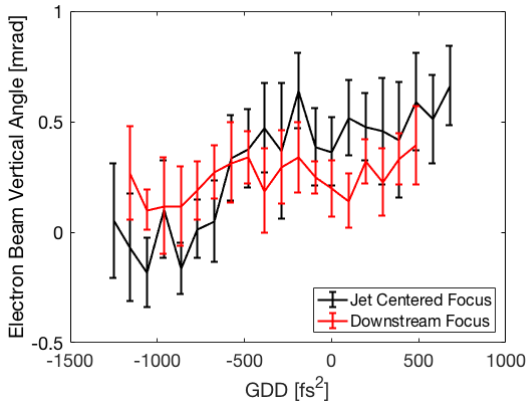

(b) Electron pointing stability vs. GDD at two longitudinal positions

Figure 6.11: Electron pointing stability increases as the vacuum focal location is moved downstream relative to the jet. The electron beam charge peaks with the vacuum focus centered on the gas jet.

Jet Relative Timing

The jet timing was varied and set to maximize the charge of electron beams from the LPA. The results are shown in black in Figure 6.12. The plotted charge is based on analysis of the phosphor screen rather than the integrating current transformer, due a problem with latter's timing, but the problem was resolved so these are the only measurements affected. Based on these measurements the jet was set to trigger 410 µs before the arrival of the drive laser, indicated in the figure by a dashed vertical line.

Two measurements of peak phase from neutral gas interferometry taken with 80 psia (red) and 100 psia (green) helium are also plotted in Figure 6.12. The time axes of these plots are the delay between triggering the jet and measuring its peak phase, which is proportional to the integrated density of the gas jet (see discussion of Figure 3.3(b)). The peak location of both phase measurements is consistent with the peak charge measured in the experiment.

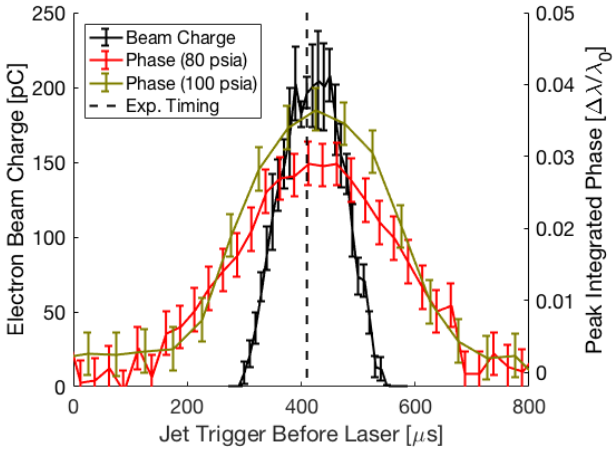

Figure 6.12: Charge (black) vs jet trigger timing and comparison with phase measurements (red and green) from offline interferometry show agreement in the timing of maximum density. This confirms that the jet trigger timing in the experiment was consistent with that in the interferometry measurements.

LPA Baseline and Target Density

The LPA was operated over a range of compressor positions to establish a baseline for comparison with the pulse front tilt measurements. Pulse front tilt was varied in the experiment by rotating an optical grating or by changing the GDD added by the final optical compressor. By definition, no residual pulse front tilt is the location of best compression and highest peak power. A baseline measurement of electron and transmitted laser properties as a function of residual GDD after the compressor was done before the measurements with pulse front tilt and repeated after those measurements. The electron vertical pointing results

are shown in Figure 6.13(b) and the laser vertical pointing results in Figure 6.13(a). In both plots, the initial baseline measurements are plotted in green and the measurements taken after those with pulse front tilt are in blue. The laser pointing agrees for residual GDD$\leq$0 fs^2 but the electron pointing is uniformly different. However, the trend in electron pointing is flat, varying by $\leq$0.5 mrad in both cases. The laser pointing is also flat to within 0.5 mrad between -900 fs^2 and 300 fs^2.

The difference between the two baseline measurements is due to the transient drop of the gas jet density profile in the first minutes after it is turned on, discussed in Chapter 3. In the initial (green) measurements, the gas jet was operating for $>$ 15 min before measuring the spectra but in the later measurement set the jet was turned on at the beginning of the measurements (the largest GDD value) after being allowed to cool down. Since both sets of spectra consists of 210 measurements in bins of 10, taken at 0.7 Hz, the density can be expected based on the functional density dependence of Eqn. 3.3 to drop by $\sim$ 15% between the first and fifth measurements (GDD $\approx$ 675 and 190 fs^2, respectively) and an additional $\sim$ 10% by the end of the scan . These percentage drops are relative to the equilibrium density value, the constant density value of the initial baseline. The jet was initially off and cooled down in the second baseline measurement and in the pulse front tilt measurements due to the need to re-align the laser at vacuum after rotating the compressor grating. Because they were taken in the same conditions, the second baseline measurement is the appropriate reference for determining the effect of added pulse front tilt.

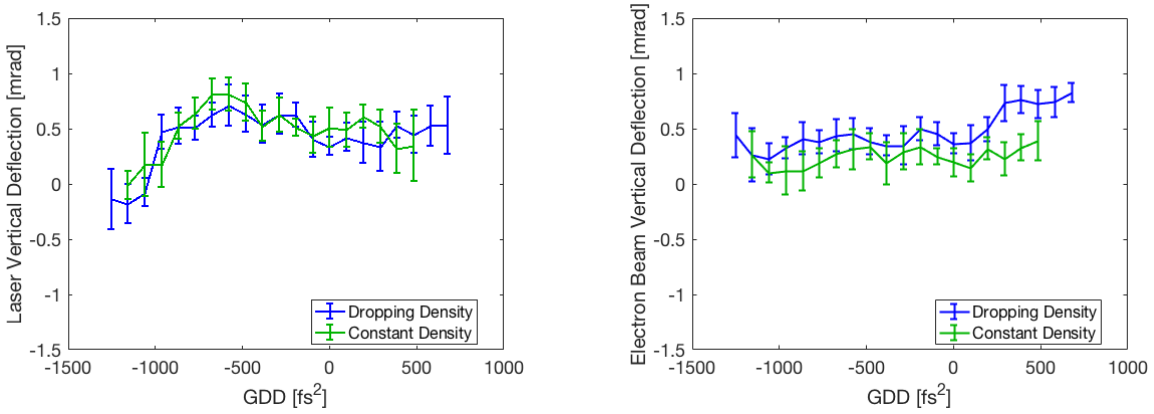

(a) Laser vertical deflection vs residual GDD

(b) Electron beam vertical deflection

Figure 6.13: Electron and laser vertical pointing dependence on GDD, measured before (green) and after (blue) similar measurements with added pulse front tilt. The laser end electron pointing trends for constant and time-varying density are consistent.

The baseline measurements also provide information on the dependence of other beam quantities on both optical compression, which varies with GDD, and density, which is fixed in one scan and dropping to the same value in the other. Like the electron beam pointing

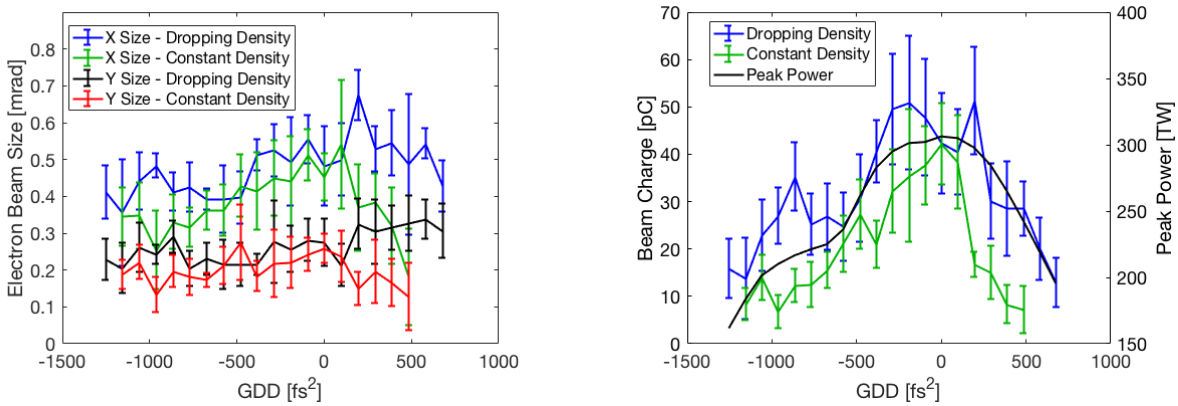

(a) Electron beam size at threshold vs. residual GDD

(b) Electron beam charge and laser peak power vs. residual GDD

Figure 6.14: Electron beam size and charge dependence on GDD. The beam size is the same for the constant and time-varying density, whereas the beam charge is significantly higher for the time-varying density.

shown in Figure 6.13(b), the size of the accelerated electron beams has little or no dependence on residual GDD. This is shown for both baseline measurements and both horizontal and vertical sizes in Figure 6.14(a). The beam charge, however, decreases significantly as the optical compressor is varied. The accelerated charge is plotted in Figure 6.14(b) for both baseline measurements. The peak laser power of the drive laser, which is a function only of the pulse energy and the temporal/spectral structure of the laser vs residual GDD, is plotted in black and is tracked well by the electron beam charge.

Laser Evolution from INF&RNO Simulations

The laser evolution in the LPA was studied using the 2D RZ-cylindrical particle-in-cell code INF&RNO [15–17]. The simulated laser was made as close to the experiment as possible. The temporal profile was obtained from FROG measurements at each GDD value, and the spatial distribution was derived from phase retrieval of intensity measurements of the focal volume. One limitation of these simulations is they could not model added spatiotemporal distortion because INF&RNO assumes azimuthal symmetry of the laser pulse. For the same reason, only an axisymmetric spatial profile could be modeled. To obtain such a profile, the asymmetric focal intensity and phase determined by phase retrieval was decomposed into Laguerre-Gaussian modes, and any non-axisymmetric ($l \neq 0$) modes were discarded. The energy of the simulated laser was reduced to 86.3% of the measured energy to account for the missing energy of the non-symmetric modes.

The INF&RNO simulations show the evolution of the laser pulse due its interaction with the plasma. The results are shown for several values of residual GDD in Figure 6.15(a).

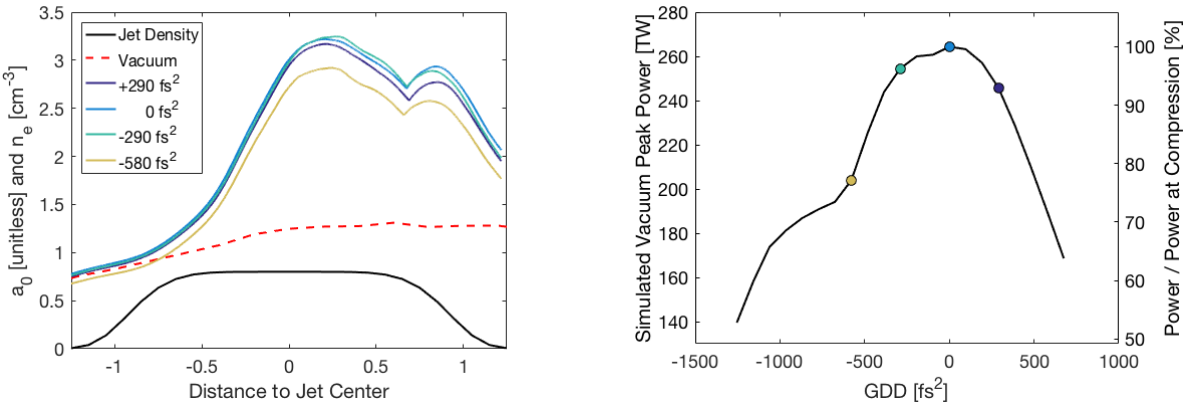

(a) Laser evolution simulated by INF&RNO for several values of GDD

(b) Simulated peak power vs. GDD

Figure 6.15: INF&RNO simulation results for different values of GDD show strong self-focusing of the laser.

For comparison, the vacuum evolution of the normalized vector potential $a_0 \propto \sqrt{I}$ is shown in red, and the simulated jet density profile is plotted in black. For these simulations, the jet density was 8×10^{17} cm^{-3}, which is 10% lower than the matching density determined by simulation, discussed at the end of Chapter 3. For this reason, the plotted a_0 evolution somewhat underestimates the self-focusing on the laser evolution. Despite this, the on-axis intensity of the driving laser pulse rapidly increases after the laser pulse enters the gas jet. The a_0 evolution is insensitive to moderate ($\lesssim$10%) changes in the peak power of the intial temporal profile (shown in Figure 6.15(b)) as the profiles for compression and $\pm$290 fs^2 are all within 0.1 of each other. Even the largest simulated residual GDD (-580 fs^2 which corresponds to a $\sim$75% drop in peak power compared to compression causes decrease in peak a_0 of only 0.3, which is a 10% drop in peak intensity.

6.4 LPA with Pulse Front Tilt

The electron beam and transmitted laser properties were measured for a range of temporal and angular chirp values to determine the latter's relative effect on and importance for stable and efficient LPA operation. As discussed in Chapter 2, pulse front tilt near focus can be a result of angular and/or spatial chirp in the near-field laser. The pulse front tilt angle evolves as a laser pulse propagates, and the profile of pulse front tilt angle as a function of propagation depends strongly on the temporal profile of the laser since the angle itself is a result of spatiotemporal coupling. The temporal profile of the laser is set by grating spacing in the optical compressor, which is easily and routinely adjusted. As discussed, angular chirp can be added in the near-field by either rotating (a rotation within the dispersion plane)

or clocking (a rotation about the grating surface normal) the final grating of the optical compressor.

In these experiments, pulse front tilt was added to the LPA drive laser by the addition of angular chirp, and the pulse front tilt magnitude and evolution as a function of propagation was varied by adjusting the temporal chirp, expressed by the residual GDD after compression. The resulting vacuum evolution of the laser is described by the theory presented in Chapter 2, but the non-linear interaction with the plasma causes strong self-focusing of the laser, as discussed in §4.3 and §6.3. Thus, the effect of changing the angular or temporal chirp of the laser on the pulse front tilt evolution cannot be inferred despite knowing the vacuum evolution. Further, self-focusing is power dependent, and increasing the magnitude of temporal chirp decreases the peak pulse power ($\sim 1/\tau$, given by Eqn. 2.11 for a Gaussian pulse) whereas the drop in power from adjusting the angular chirp is small.

To avoid conflating the effects of input angle/transverse offset and pulse front tilt, the laser path to target was realigned each time the angular chirp was adjusted. For each measurement, the final optical compressor grating was clocked in the range of -30 to +120 µrad and the laser input pointing was adjusted using the next mirror in its optical path to keep to vacuum focal spot position fixed. The distance from the grating to the next mirror was 4.3 m, and at the largest angular chirp setting (+120 µrad) the central wavelength of 810 nm would be vertically offset by ∼0.7 mm after propagating that distance. This near-field shift corresponds to an 52 µrad change in the laser input angle. This is much larger than the 1.3 µrad RMS input pointing fluctuation measured in [18], but in Figure 6.4 both the input angle and position are being changed, both of which deflect the laser in the same direction, so it provides an upper limit on the difference in pointing from changing only the input angle. The bins in Figure 6.4 are separated by ∼675 µrad, and the change in pointing between adjacent bins is close to the error on each binned set of measurements. So, changing the input angle by only $\sim 1/10^{\text{th}}$ of this will not cause a noticeable change in output pointing.

Effect of Angular Chirp

The effect of changing angular chirp on electron and laser steering is shown in Figure 6.16(a). The horizontal dashed line indicates zero deflection. A laser pulse is only included in the average at a particular angular chirp if the associated electron beam is also included (*i.e.*, has sufficient charge for detection, does not fall outside the phosphor aperture...). The observed linear trend in electron steering in the pulse front tilt plane for small-to-moderate angular chirp values is consistent with previous measurements done with compressed laser pulses, shown in Figure 6.16(b) [10]. However, at larger values of angular chirp the electron and laser pointing trends become less-than-linear. Further, the laser and electron pointing trends are strongly anti-correlated with each other, except at the leftmost laser pointing value.

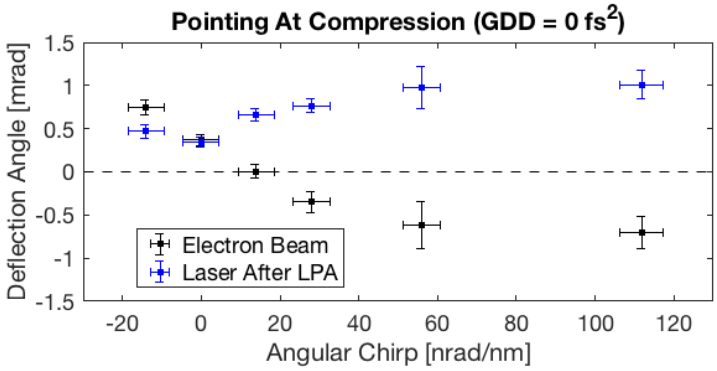

(a) Measured laser and electron beam vertical pointing at compression.

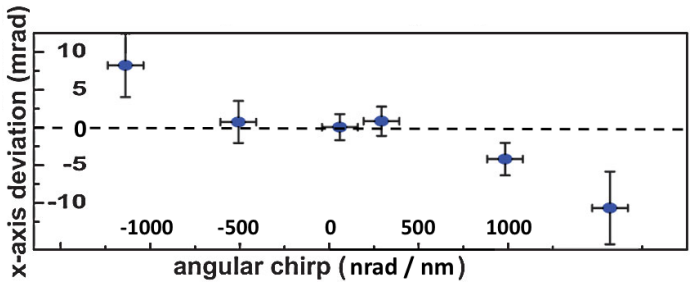

(b) Electron pointing trend measured in previous work. Adapted from Fig. 2 of [10] with permission.

Figure 6.16: Electron and laser pointing at compression [GDD = 0 fs^2] for different values of near-field angular chirp. The trends (a) measured in this work are consistent with (b) the electron pointing trends measured in previous work.

Effect of Temporal Chirp

The resulting trends in electron beam and output laser pointing are shown in Figure 6.17(a) for the case where angular chirp is kept fixed at 28 nrad/nm and the temporal chirp of the drive laser is varied [71]. Again, the electron and laser pointing trends are anti-correlated, and both are nonzero at compression (GDD = 0 fs^2). In Figure 6.16(a), the pointing trend of both the laser and electron beam was shown to be linear for near-field angular chirp values $|\psi| \lesssim 40$ nrad/nm. As a function of temporal chirp, the pointing trends are also linear in the shaded region of $-600\,\mathrm{fs}^2 \lesssim \mathrm{GDD} \lesssim 0\,\mathrm{fs}^2$ but become less-than-linear or even reverse direction outside that range.

The linear pointing range corresponds to the region of temporal chirp which maximizes red shifting of the output laser spectrum, shown in Figure 6.17(b). The shaded region is the range where red shift wavelength of the spectrum $\lambda_R \gtrsim 895$ nm. The red shift wavelength is defined as the wavelength above which the spectrum contains $1/e^2 \approx 13.5\%$ of its energy and

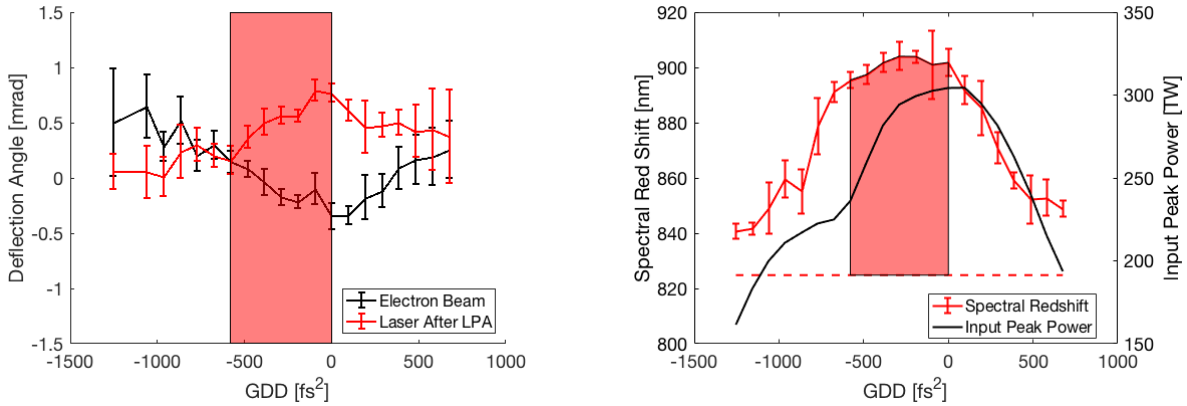

(a) Laser and electron pointing as functions of GDD (b) Peak power and red shift as functions of GDD

Figure 6.17: At fixed angular chirp $\psi = 28$ nrad/nm, (a) laser and electron beam vertical pointing are linear with temporal chirp in the shaded region. (b) The shaded region corresponds to maximum red shifting of the output laser spectrum, indicating high-amplitude plasma wake.

is given by

$$\frac{1}{e^2} = \frac{\int_{\lambda_R}^{\infty} I(\lambda) d\lambda}{\int_{-\infty}^{\infty} I(\lambda) d\lambda}.$$

The red shift of the input laser, measured as the output laser with no plasma, is shown as a dashed horizontal line in the lower plot for comparison. Red shifting of the output spectrum increases with wake amplitude and propagation distance in the plasma [60, 76]. The maximum change in laser transverse position across the gas jet $\Delta y_{max} \approx \theta_{y,max} \times L_{\text{gas jet FWHM}} < 40$ µm is much less than the transverse scale over which the jet density profile changes. So, all laser pulses travel the same distance through the plasma and encounter the same effective density profile regardless of angular deflection, and the change in spectral red shift in the output laser must be due to the wake amplitude being on average higher in the shaded region than outside it. The trend in red shifting as a function of GDD is not peaked at GDD $= 0$ fs^2 and does not follow the peak power of the input laser plotted in black in Figure 6.17(b). This is because the spectrum of the laser contains high-order phase resulting in a significantly non-Gaussian temporal profile, the structure of which affects the wake amplitude, so the self-guiding of the laser is not a only a function of the ratio P/P_c [58, 60].

Laser Deflection Comparison with Theory

The output laser pointing as a function of temporal chirp is plotted for all measured values of added angular chirp in Figure 6.18(a). For all added angular chirp values, the trends coincide at GDD ≈ -250 fs^2 at a laser deflection of $\theta_l \approx 0.55$ mrad. The laser pointing trend with no

added angular chirp also goes through the crossing point, which confirms that the laser is deflected upward by the LPA even in the absence of pulse front tilt. The significance of the crossing point is that the effect of pulse front tilt on laser pointing cancels out at this value of GDD so the deflection level at the crossing is the zero point of laser pointing. Although the plot of $\psi = 0$ nrad/nm should contain the same information, the deflection level determined by the crossing point is independent of angular chirp calibration. The 0.55 mrad deflection corresponds to the transverse density gradient caused by a 250 µm input offset based on ray tracing and the final density profile from Chapter 3. This is consistent with the 50 ± 200 µm input transverse offset determined in Appendix B.

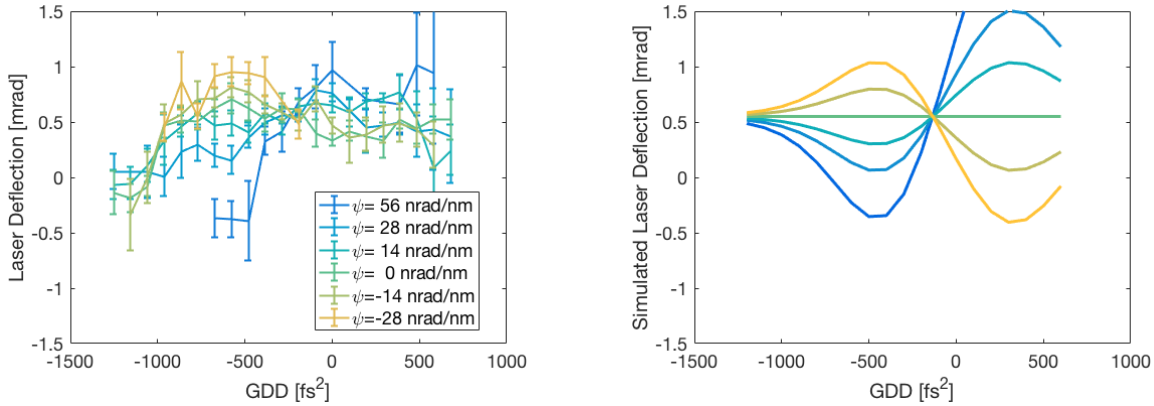

(a) Laser deflection angle as a function of GDD for all values of added angular chirp

(b) Laser deflection from simulation of a non-evolving Gaussian laser, with a 0.55 mrad offset

Figure 6.18: (a) Measured laser output steering and (b) predicted laser steering from simulation, offset by 0.55 mrad, show good qualitative agreement.

An expression was derived in Chapter 4 for the deflection of a Gaussian laser with pulse front tilt by interaction with a plasma. The expression gave good agreement with two dimensional simulations for $a_0 \lesssim 3$. The predicted laser deflection at a particular location was given by Eqn. 4.61 as

$$\left\langle \frac{d\Theta}{dz} \right\rangle = \frac{a_0^2}{\gamma_0} \frac{n_0}{n_c} \frac{k_{p,NL}}{16} (pc)(k_{p,NL}L)\sqrt{\pi} e^{-\frac{(k_{p,NL}L)^2}{4}} \times \begin{cases} \frac{1}{2} + \frac{3}{(k_p W)^2} & \text{(2D)} \\ \frac{1}{2\sqrt{2}} + \frac{4}{\sqrt{2}(k_p W)^2} & \text{(3D)} \end{cases} \tag{6.4}$$

where $pc = \tan\theta_{PFT}$ is the pulse front tilt at z, L is the $1/e^2$ pulse length, W is the pulse width, and $\gamma_0 = \sqrt{1 + a_0^2/2}$. The nonlinear wavenumber of the plasma was defined as

$$k_{p,NL} = \frac{k_p}{1 + (3/16)(E_{max}/E_0)^2} \approx k_p \left[1 + \frac{3\pi a_0^4}{2^9 \gamma_0^2} e^{-(k_p L)^2/4} \right]^{-1}. \tag{6.5}$$

The approximation is for a Gaussian laser driver. The results of this theory are plotted in Figure 6.18(b) for a non-evolving Gaussian laser. The simulated results are offset by

0.55 mrad to account for the transverse density gradient indicated by the crossing point of the measured laser deflection trends. The length of the laser L as a function of GDD was taken from the FROG measurements discussed in Chapter 2. The focal spot size $w_0 = 62$ µm and $a_0 = 1.5$ were set so the Gaussian beam approximately matched the measured intensity evolution, determined by phase retrieval (also discussed in Chapter 2). The simulated laser deflection in Figure 6.18(b) is in good qualitative agreement with the measured laser deflection Figure 6.18(a) for GDD$\lesssim 0$ fs^2.

Electron Pointing Trends and Comparison with Theory

The electron beam pointing deflection for all values of added angular chirp pointing are plotted in Figure 6.19(a) as a function of temporal chirp (GDD). The electron pointing trends are qualitatively different from the trends in laser pointing plotted in Figure 6.18(a), and the electron trends cross at a distinct location. This crossing point is located at GDD ≈ -900 fs^2 at a value of $\theta_e \approx 0.35$ mrad (~ 0.2 mrad below the laser crossing point). These differences confirm that the electron beam is deflected by a different mechanism than the laser and that the difference in laser and electron pointing cannot be an artifact of the analysis.

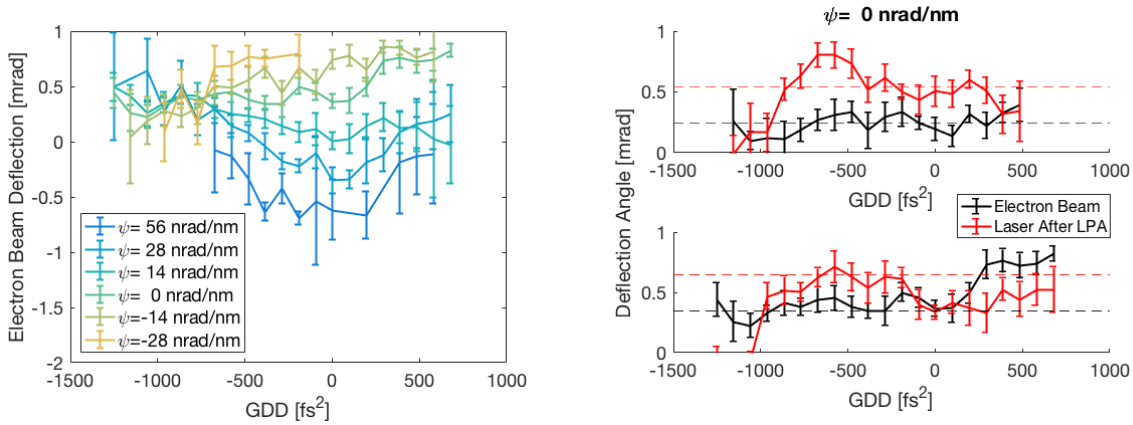

(a) Measured electron beam output angle as a function of GDD for all values of added angular chirp

(b) No added near-field angular chirp. Density is constant in upper plot and time-varying in lower plot. Dashed lines are separated by 0.3 mrad.

Figure 6.19: (a) Electron pointing trends as a function of near-field angular chirp and temporal chirp are qualitatively similar with trend magnitude scaled by angular chirp; (b) Laser and electron pointing as a function of temporal chirp (no angular chirp) show electrons are consistently ~ 0.3 mrad below laser output, except when density is rapidly dropping on the right of the lower plot.

The difference in output pointing at the electron crossing point ($\theta_e \approx 0.35$ mrad) in Figure 6.19(a) and the laser crossing point ($\theta_l \approx 0.55$ mrad) in Figure 6.18(a) indicates that there is an offset between the laser and electron beam in addition to the deflection caused

by pulse front tilt. Such an offset was also observed in Figure 6.9. The offset between the electron beam and laser output pointing is shown in Figure 6.19(b) as a function of GDD with no added angular chirp. In the upper plot, the gas jet has been allowed to operate for > 10 min so the jet density has reached its equilibrium value. With a constant density target, the electron beam is consistently deflected ~ 0.3 mrad below the laser, consistent with the difference in crossing values between the electron and laser pointing trends. In the lower plot in Figure 6.19(b), gas jet operation is initiated at start of the measurements (GDD = 650 fs^2) and drops according to Eqn. 5.2 as GDD is decreased. The same trend in density is also present in the measurements of pointing with added near-field angular chirp. With target density, the electrons are offset ~ 0.3 mrad below the laser pointing for GDD<0 fs^2. The change in offset for GDD$\gtrsim 0$ fs^2 is likely due to the dropping density, since the rate of density change is highest in this region.

An ellipsoidal model of the wake was developed in Chapter 4 to predict electron steering in an LPA and deflection at the end of the plasma target. The electron pointing at the end of the gas jet was estimated in Eqn. 4.77 to be

$$\theta_e = \theta_l + \frac{\mathrm{d}y_e}{\mathrm{d}z} - \frac{\pi^2}{2}\left(\frac{\mathrm{d}y_e}{\mathrm{d}z} + \frac{\mathrm{d}\theta_l}{\mathrm{d}z}\lambda_\beta\right). \tag{6.6}$$

where the wake position y_e was given in Eqn. 4.66 as

$$y_e = (\xi_e - \xi_b)\tan\theta_w = [(v_g - c)(t_{inj} - t) - 2[L_{inj} - L_w] - L_w]\tan\theta_w. \tag{6.7}$$

Here, W_w and L_w are the width and length of the wake, respectively. The wake angle is given by

$$\tan\theta_w = \frac{pcW_w^2}{L_w^2 + (pcW_w)^2} \approx pc\left(\frac{W_w}{L_w}\right)^2 \tag{6.8}$$

since the pulse front tilt is assumed to be small. The wake length L_w was estimated for the bubble regime when the laser and bubble sizes are not matched to be $L_w \approx 2/k_{p,NL}$ where $k_{p,NL}$ is the nonlinear plasma wavenumber given in Eqn. 6.5. The wake width W_w was estimated to be similar in size to the pulse width, so $W_w \approx W$.

The electron deflection depends on the evolution of the laser in the plasma, so it is not possible to predict the electron deflection based on vacuum laser evolution. To make predictions about the electron steering, three dimensional simulations of laser evolution were conducted using the particle-in-cell code WARP [12–14]. Simulations were performed for a range of temporal chirp values (GDD values) and a near-field angular chirp of 28 nrad/nm. The simulated plasma density profile was a super-Gaussian given by

$$n(z) = 2 \times [4.35 \times 10^{17}\,\mathrm{cm}^{-3}] \exp\left\{-\ln(2)\left(\frac{2(z - z_0)}{18\text{ mm}}\right)^6\right\} \tag{6.9}$$

which corresponds to the gas density which best matched the observed red shifting from the experiment (see Chapter 3). The factor 2 is a conversion from atomic helium density

to electron density, and the gas was assumed to be fully ionized since the intensity of the laser pulse is many orders of magnitude above the ionization threshold. The spatial profile was determined by phase retrieval as discussed in Chapter 2 and shown in Figure 2.6(c). The temporal profile of the laser pulse at each value of GDD was determined by FROG measurements. The intensity profiles are shown Figure 2.2.

The laser steering predicted by WARP simulations and the electron beam pointing predicted by Eqn. 6.6 are plotted against corresponding measured deflection values in Figure 6.20. The WARP simulation results are output in 1 mm increments, but this increment is comparable to the density gradient length scale at the end of the gas jet.To evaluate the electron pointing theory, Eqn. 6.6 was interpolated from the nearest output locations to the z-location where Eqn. 4.78 is satisfied. The simulated laser steering values have been offset by 0.55 mrad to agree with the measured crossing point from Figure 6.18(a), which accounts for the transverse density gradient present in the experiment but not in the simulation. The electron pointing predicted by theory has been offset by -0.3 mrad to account for the measured laser-electron offset illustrated in Figure 6.19(b). A possible explanation for the electron-laser offset is a spatially varying transverse density gradient. The agreement between the measured and theoretical electron deflection angles indicates that the ellipsoid model correctly describes the physics responsible for the pointing trend as a function of GDD [71].

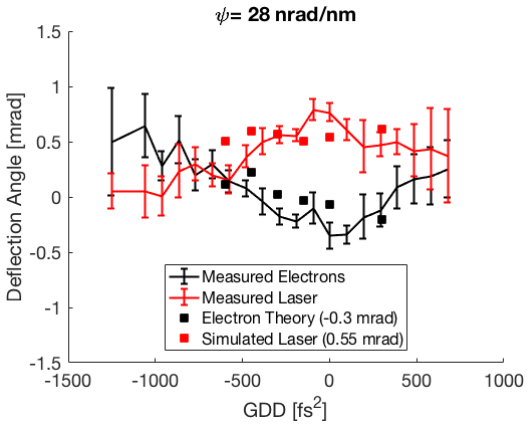

Figure 6.20: Comparison of measured laser and electron pointing with that predicted by simulation and theory shows good agreement.

The WARP simulations also suggest an explanation for the qualitative agreement between the measured laser deflection shown in Figure 6.18(a), which is non-Gaussian and strongly self-focused, and the predictions based on a non-evolving Gaussian laser shown in Figure 6.18(b). The pulse front tilt evolution of a laser pulse with GDD = -300 fs^2 and near-field angular chirp $\psi = 28$ nrad/nm is shown in Figure 6.4. The vacuum evolution of the pulse front tilt angle is plotted in blue, and the evolution in a plasma is plotted in red. (The plasma profile is flat between $z = 5$ mm and $z = 20$ mm and drops to ~ 0 within 5 mm.) The curves begin to diverge at $\sim$10 mm which coincides with the onset of self-focusing of the laser pulse, shown

by the normalized vector potential a_0 plotted as dashed curves. After the laser in plasma has focused to a high intensity a_0, it remains stable due to self-focusing until the end of the gas jet, and the pulse front tilt evolution matches the vacuum trend in slope, even when the laser is diffracting (region of dropping a_0) at the end of the gas jet. The similarity in pulse front tilt evolution despite the differences in laser intensity and size between plasma and vacuum propagation may account for the success of the non-evolving Gaussian model.

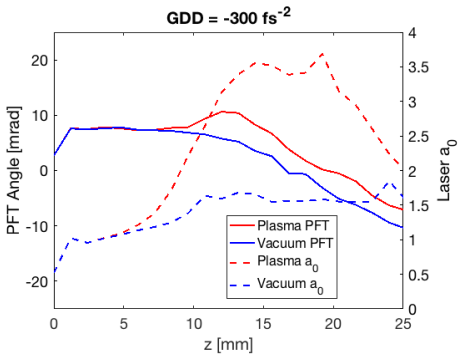

Figure 6.21: Vacuum (blue) and plasma (red) evolution of a_0 and pulse front tilt angle from WARP simulations show that pulse front tilt evolution in plasma follows vacuum evolution, except in region of rapid self-focusing.

6.5 Concluding Remarks

The effect on an LPA of pulse front tilt from near-field angular chirp and from temporal chirp was measured in a set of experiments at the BELLA Center. To compare the measurements with the theoretical model developed in Chapter 4, simulations were performed utilizing the BELLA laser structure and the density profile of the plasma target determined and verified in the preceding chapters. The results were found to be in good agreement with the model of laser and electron deflection.

Chapter 7

Conclusion

In this work, the effects on laser plasma accelerators of temporal profile and spatiotemporal coupling resulting in pulse front tilt were studied theoretically and compared with experiments performed at the BErkeley Laboratory Laser Accelerator (BELLA) Center at Lawrence Berkeley National Laboratory. Modulation of the laser spectrum was used to probe both the plasma density profile of an LPA experiment in §5.2 and to constrain the temporal profile of the BELLA laser in §5.1. A formula for the steering of a tilted Gaussian laser pulse was derived and validated with two-dimensional particle-in-cell simulations in §4.3. A theoretical model of the resulting asymmetric plasma wake was created in §4.4 to explain the steering of electrons in the plasma and their deflection at the end of the plasma target. The BELLA experiments presented in Chapter 6 demonstrated good agreement with the predictions of the model as well as with simulations of laser propagation. The experiments covered a wider range of pulse front tilt profiles than previous work [10], examining the effect of both near-field angular chirp and temporal profile.

Detailed knowledge of the accelerating structure (the plasma wake) is necessary to understand and optimize a laser plasma accelerator. This microscopic structure can be determined through numerical simulation [12–14] or direct wake imaging [46], but this work provides a simple, predictive model to relate plasma wake structure to the laser profile. Using this model, it is possible to immediately calculate the pulse front tilt (and the required adjustments necessary to the optical compressor) needed to steer the laser and/or electron beam by a desired angle. A potential application is the separation of accelerated electrons from the driving laser pulse at the end of the accelerator. In typical LPA systems, the electron beam is separated from the laser with a large magnet, to deflect the electrons, or a mirror with a hole, as discussed in Chapter 6. Another possible use is compensation of undesired electron beam deflection caused by other factors (laser intensity asymmetry, plasma target density gradients, etc).

The sensitivity of laser and electron deflection to temporal chirp could be used as a diagnostic of angular chirp for laser plasma accelerator systems. By rotating/clocking the optical compressor diffraction grating to minimize the variation in laser and electron pointing as a function of temporal chirp, angular chirp and resulting pulse front tilt can be minimized.

It is important to note that only varying the angular chirp is insufficient to determine the grating clocking which minimizes angular chirp in the laser because the laser and electron zero points, determined by their crossing values, are nonzero. This method has an advantage over other diagnostics of pulse front tilt because it is an in-situ measurement and can be implemented in a typical LPA system with no additional equipment or modification.

The electron deflection theory demonstrates the importance of control of LPA targets and associated diagnostics such as those discussed in Chapter 3. The model of electron beam deflection developed in Chapter 4 shows how strongly the accelerated electron beams from a laser plasma accelerator depend on the exit section of the plasma target. If the density drop at the end of the plasma target was sufficiently sharp ($n/(\mathrm{d}n/\mathrm{d}z) \lesssim \lambda_p$) that Eqn. 4.78 was never satisfied, then the electron beam would follow the laser. However, in the plasma target used in these experiments, characterized in Chapter 3, there was an extended region over which the electrons were exposed to the focusing forces of the wake, resulting in their deflection.

Several future developments of the methods and techniques presented here are possible. It may be possible to tune the structure of the wake (e.g. to obtain a particular focusing force profile) via controlled spatiotemporal coupling of the laser pulse with a more complicated spatial dependence. Such controlled coupling would be possible either by using an adaptive optical system or a custom wave plate. It may also be possible to extend these results and their potential applications to preformed plasma channels, which allow guiding of the laser pulse. The laser steering derivation assumed a flat background plasma profile, but a preformed plasma channel with density gradients on the scale of the laser spot size was used for the highest-energy-to-date laser plasma accelerator result [5]. Preformed plasma channels have many advantages over reliance on self-guiding of the driving laser pulse [73], and the presence of strong density gradients will likely change the laser steering result.

Bibliography

[1] W. K. H. Panofsky, "The evolution of particle accelerators and colliders", Beam Line **Spring**, 36–44 (1997).

[2] *Advanced light source activity report 2006*, tech. rep. LBNL-62841 (Lawrence Berkeley National Laboratory, 2006).

[3] C. B. Schroeder, E. Esarey, C. G. R. Geddes, C. Benedetti, and W. P. Leemans, "Physics considerations for laser-plasma linear colliders", Phys Rev ST Accel Beams **13**, 101301 (2010).

[4] *Advanced light source 2015 quick facts*, Sept. 2015.

[5] W. P. Leemans, A. J. Gonsalves, H.-S. Mao, K. Nakamura, C. Benedetti, C. B. Schroeder, C. Tóth, J. Daniels, D. E. Mittelberger, S. S. Bulanov, J.-L. Vay, C. G. R. Geddes, and E. Esarey, "Multi-gev electron beams from capillary-discharge-guided subpetawatt laser pulses in the self-trapping regime", Phys Rev Lett **113**, 245002 (2014).

[6] C. B. Schroeder, "Challenges and opportunities for plasma acceleration for high energy colliders", Advanced Accelerator Concepts (San Jose, CA), 2014.

[7] T. Tajima and J. Dawson, "Laser electron accelerator", Phys Rev Lett **43**, 267 (1979).

[8] E. Esarey, C. B. Schroeder, and W. P. Leemans, "Physics of laser-driven plasma-based electron accelerators", Rev Mod Phys **81**, 1229 (2009).

[9] M. Schnell, A. Sävert, I. Uschmann, M. Reuter, M. Nicolai, T. Kämpfer, B. Landgraf, O. Jäckel, O. Jansen, A. Pukhov, M. C. Kaluza, and C. Spielmann, "Optical control of hard x-ray polarization by electron injection in a laser wakefield accelerator", Nat Commun **4**, 2421 (2013).

[10] A. Popp, J. Vieira, J. Osterhoff, Z. Major, R. Hörlein, M. Fuchs, R. Weingartner, T. P. Rowlands-Rees, M. Marti, R. A. Fonseca, S. F. Martins, L. O. Silva, S. M. Hooker, F. Krausz, F. Grüner, and S. Karsch, "All-optical steering of laser-wakefield-accelerated electron beams", Phys Rev Lett **105**, 215001 (2010).

[11] M. Kaluza, S. Mangles, A. Thomas, Z. Najmudin, A. Dangor, C. Murphy, J. Collier, E. Divall, P. Foster, C. Hooker, et al., "Observation of a long-wavelength hosing modulation of a high-intensity laser pulse in underdense plasma", Phys Rev Lett **105**, 095003 (2010).

[12] D. P. Grote, A. Friedman, J.-L. Vay, and I. Haber, "The warp code: modeling high intensity ion beams", in Aip conference proceedings, Vol. 749, 1 (AIP, 2005), pp. 55–58.

[13] J.-L. Vay, "Simulation of beams or plasmas crossing at relativistic velocity a", Physics of Plasmas **15**, 056701 (2008).

[14] J.-L. Vay, "Noninvariance of space- and time-scale ranges under a lorentz transformation and the implications for the study of relativistic interactions", Physical Review Letters **98** (2007) `10.1103/PhysRevLett.98.130405`.

[15] C. Benedetti, C. Schroeder, E. Esarey, C. Geddes, and W. Leemans, "Efficient modeling of laser-plasma accelerators with inf&rno", in Aip conference proceedings, Vol. 1299, 1 (AIP, 2010), pp. 250–255.

[16] C. Benedetti, C. B. Schroeder, E. Esarey, and W. P. Leemans, "Efficient modeling of laser-plasma accelerators using the ponderomotive-based code inf&rno", in Proceedings of icap (2012), THAAI2.

[17] C. Benedetti, C. Schroeder, C. Geddes, E. Esarey, and W. Leemans, "An accurate and efficient laser-envelope solver for the modeling of laser-plasma accelerators", Plasma Phys Contr F **60**, 014002 (2017).

[18] K. Nakamura, H. S. Mao, A. J. Gonsalves, H. Vincenti, D. E. Mittelberger, J. Daniels, A. Magana, C. Toth, and W. P. Leemans, "Diagnostics, control and performance parameters for the bella high repetition rate petawatt class laser", IEEE J Quantum Elect **53**, 1–21 (2017).

[19] D. Mittelberger, K. Nakamura, R. Lehe, A. Gonsalves, C. Benedetti, H.-S. Mao, J. Daniels, N. Dale, S. Venkatakrishnan, K. Swanson, et al., "Characterization of the spectral phase of an intense laser at focus via ionization blueshift", J Opt Soc Am B **33**, 1978–1985 (2016).

[20] B. C. Stuart, M. D. Feit, S. Herman, A. M. Rubenchik, B. W. Shore, and M. D. Perry, "Nanosecond-to-femtosecond laser-induced breakdown in dielectrics", Phys Rev B **53**, 1749–1761 (1996).

[21] D. Strickland and G. Mourou, "Compression of amplified chirped optical pulses", Opt Commun **56**, 219–221 (1985).

[22] V. Leshchenko, A. Povrozin, and S. Karelin, "Calculation of stretching factor for optical pulse stretcher", Probl Atom Sci Tech, Nuclear Physics Investigations **97**, 132–135 (2015).

[23] O. E. Martinez, T. Prabhuram, M. C. Marconi, and J. J. Rocca, "Magnified expansion and compression of subpicosecond pulses from a frequency-doubled nd: ylf laser", IEEE J Quantum Elect **25**, 2124–2128 (1989).

[24] G. Cheriaux, B. Walker, L. F. Dimauro, P. Rousseau, F. Salin, and J. P. Chambaret, "Aberration-free stretcher design for ultrashort-pulse amplification", Opt Lett **21**, 414–416 (1996).

[25] Z. Zhang, Y. Song, D. Sun, L. Chai, H. Sun, and C.-y. Wang, "Compact and material-dispersion-compatible offner stretcher for chirped pulse amplifications", Opt Commun **206**, 7–12 (2002).

[26] E. Treacy, "Optical pulse compression with diffraction gratings", IEEE J Quantum Elect **5**, 454–458 (1969).

[27] C. Fiorini, C. Sauteret, C. Rouyer, N. Blanchot, S. Seznec, and A. Migus, "Temporal aberrations due to misalignments of a stretcher-compressor system and compensation", IEEE J Quantum Elect **30**, 1662–1670 (1994).

[28] L. Sarger and J. Oberlè, "How to measure the characteristics of laser pulses", in *Femtosecond laser pulses*, edited by C. Rullière, 2nd ed. (Springer Science+Business Media, Inc., New York, NY, USA, 2005) Chap. 7, pp. 195–222.

[29] R. Trebino and D. J. Kane, "Using phase retrieval to measure the intensity and phase of ultrashort pulses: frequency-resolved optical gating", J Opt Soc Am A **10**, 1101–1111 (1993).

[30] R. Trebino, K. W. DeLong, D. N. Fittinghoff, J. N. Sweetser, M. A. Krumbügel, B. A. Richman, and D. J. Kane, "Measuring ultrashort laser pulses in the time-frequency domain using frequency-resolved optical gating", Rev Sci Instrum **68**, 3277–3295 (1997).

[31] C. Iaconis and I. A. Walmsley, "Spectral phase interferometry for direct electric-field reconstruction of ultrashort optical pulses", Opt Lett **23**, 792–794 (1998).

[32] C. Kolmeder, W. Zinth, and W. Kaiser, "Second harmonic beam analysis, a sensitive technique to determine the duration of single ultrashort laser pulses", Opt Commun **30**, 453–457 (1979).

[33] P. O'Shea, M. Kimmel, X. Gu, and R. Trebino, "Highly simplified device for ultrashort-pulse measurement", Opt Lett **26**, 932–934 (2001).

[34] J. R. Fienup, "Phase retrieval algorithms: a comparison", Appl Opt **21**, 2758–2769 (1982).

[35] S. Marchesini, "Invited article: a unified evaluation of iterative projection algorithms for phase retrieval", Rev Sci Instrum **78**, 011301 (2007).

[36] Y. Shechtman, Y. C. Eldar, O. Cohen, H. N. Chapman, J. Miao, and M. Segev, "Phase retrieval with application to optical imaging: a contemporary overview", IEEE Signal Process Mag **32**, 87–109 (2015).

[37] L. Allen and M. Oxley, "Phase retrieval from series of images obtained by defocus variation", Opt Commun **199**, 65–75 (2001).

[38] R. W. Gerchberg and W. O. Saxton, "A practical algorithm for the determination of the phase from image and diffraction plane pictures", Optik **35**, 237–246 (1972).

[39] J. R. Fienup, "Reconstruction of an object from the modulus of its fourier transform", Opt Lett **3**, 27–29 (1978).

[40] J. R. Fienup, "Phase-retrieval algorithms for a complicated optical system", Appl Opt **32**, 1737–1746 (1993).

[41] S. Akturk, X. Gu, E. Zeek, and R. Trebino, "Pulse-front tilt caused by spatial and temporal chirp", Opt Express **12**, 4399–4410 (2004).

[42] S. Akturk, M. Kimmel, P. O'Shea, and R. Trebino, "Measuring pulse-front tilt in ultrashort pulses using grenouille", Opt Express **11**, 491–501 (2003).

[43] R. Lehe, "Evolution of a pulse with spatio-temporal couplings", unpublished communication, 2017.

[44] G. R. Plateau, N. H. Matlis, C. G. R. Geddes, A. J. Gonsalves, S. Shiraishi, C. Lin, R. A. van Mourik, and W. P. Leemans, "Wavefront-sensor-based electron density measurements for laser-plasma accelerators", Rev Sci Instrum **81**, 033108 (2010).

[45] T. Weineisen, B. Göppner, K. Schmid, M. Fuchs, H. Schröder, S. Karsch, and F. Grüner, "Density measurement in a laser-plasma-accelerator capillary using raman scattering", Phys Rev ST Accel Beams **14**, 050705 (2011).

[46] N. H. Matlis, S. Reed, S. S. Bulanov, V. Chvykov, G. Kalintchenko, T. Matsuoka, P. Rousseau, V. Yanovsky, A. Maksimchuk, S. Kalmykov, G. Shvets, and M. C. Downer, "Snapshots of laser wakefields", Nat Phys **2**, 749–753 (2006).

[47] M. Krishnan, J. Wright, and T. Ma, "A fast, electromagnetically driven supersonic gas jet target for laser wakefield acceleration", AIP Conference Proceedings **1086**, 264–269 (2009).

[48] M. Krishnan, K. W. Elliott, C. G. R. Geddes, R. A. van Mourik, W. P. Leemans, H. Murphy, and M. Clover, "Electromagnetically driven, fast opening and closing gas jet valve", Phys Rev ST Accel Beams **14**, 033502 (2011).

[49] J. D. Anderson, *Modern compressible flow: with historical perspective*, 3rd (McGraw-Hill Education, 2002).

[50] A. C. Kak and M. Slaney, *Principles of computerized tomographic imaging* (SIAM, 2001).

[51] P. C. Hansen and M. Saxild-Hansen, "Air tools - a matlab package of algebraic iterative reconstruction methods", J Comput Appl Math **236**, 2167–2178 (2012).

[52] A. Alexeenko, D. Levin, S. Gimelshein, R. Collins, and G. Markelov, "Numerical simulation of high-temperature gas flows in a millimeter-scale thruster", J Thermophys Heat Tr **16**, 10–16 (2002).

[53] X. M. Tong and C. D. Lin, "Empirical formula for static field ionization rates of atoms and molecules by lasers in the barrier-suppression regime", J Phys B-At Mol Opt **38**, 2593 (2005).

[54] M. V. Ammosov, N. B. Delone, and V. P. Krainov, "Tunnel ionization of complex atoms and of atomic ions in an alternating electromagnetic field", Sov Phys JETP-USSR **64**, 1191–1194 (1986).

[55] S. P. L. Blanc, R. Sauerbrey, S. C. Rae, and K. Burnett, "Spectral blue shifting of a femtosecond laser pulse propagating through a high-pressure gas", J Opt Soc Am B **10**, 1801–1809 (1993).

[56] P. Chessa, E. De Wispelaere, F. Dorchies, V. Malka, J. R. Marquès, G. Hamoniaux, P. Mora, and F. Amiranoff, "Temporal and angular resolution of the ionization-induced refraction of a short laser pulse in helium gas", Phys Rev Lett **82**, 552–555 (1999).

[57] E. Esarey, G. Joyce, and P. Sprangle, "Frequency up-shifting of laser pulses by copropagating ionization fronts", Phys Rev A **44**, 3908–3911 (1991).

[58] W. P. Leemans, P. Catravas, E. Esarey, C. G. R. Geddes, C. Toth, R. Trines, C. B. Schroeder, B. A. Shadwick, J. van Tilborg, and J. Faure, "Electron-yield enhancement in a laser-wakefield accelerator driven by asymmetric laser pulses", Phys Rev Lett **89**, 174802 (2002).

[59] L. M. Gorbunov and V. I. Kirsanov, "Excitation of plasma waves by an electromagnetic wave packet", Sov Phys JETP-USSR **93** (1986).

[60] P. Sprangle, E. Esarey, and A. Ting, "Nonlinear interaction of intense laser pulses in plasmas", Phys Rev A **41**, 4463 (1990).

[61] S. I. Braginskii, "Transport phenomena in a completely ionized two-temperature plasma", Sov Phys JETP-USSR **6**, 358–369 (1958).

[62] J. T. Dakin, "Nonequilibrium lighting plasmas", IEEE T Plasma Sci **19**, 991–1002 (1991).

[63] J. D. Huba, *Nrl plasma formulary*, tech. rep. (Naval Research Laboratory, Plasma Physics Division, Naval Research Laboratory, Washington, DC, 20375, 2016).

[64] F. F. Chen, *Introduction to plasma physics and controlled fusion*, 2nd ed., Vol. Volume 1: Plasma Physics (Plenum Press, New York and London, 1984).

[65] P. Sprangle, E. Esarey, and A. Ting, "Nonlinear theory of intense laser-plasma interactions", Phys Rev Lett **64**, 2011 (1990).

[66] P. Sprangle, C.-M. Tang, and E. Esarey, "Relativistic self-focusing of short-pulse radiation beams in plasmas", IEEE T Plasma Sci **15**, 145–153 (1987).

[67] W. Lu, C. Huang, M. Zhou, W. B. Mori, and T. Katsouleas, "Nonlinear theory for relativistic plasma wakefields in the blowout regime", Phys Rev Lett **96**, 165002 (2006).

[68] D. J. Griffiths, *Introduction to electrodynamics*, 3rd (Prentice Hall, 1999).

[69] W. Lu, M. Tzoufras, C. Joshi, F. S. Tsung, W. B. Mori, J. Vieira, R. A. Fonseca, and L. O. Silva, "Generating multi-gev electron bunches using single stage laser wakefield acceleration in a 3d nonlinear regime", Phys Rev ST Accel Beams **10**, 061301 (2007).

[70] C. Benedetti, C. B. Schroeder, E. Esarey, F. Rossi, and W. P. Leemans, "Numerical investigation of electron self-injection in the nonlinear bubble regime", Phys Plasmas **20**, 103108 (2013).

[71] D. E. Mittelberger, M. Thévenet, K. Nakamura, A. J. Gonsalves, C. Benedetti, R. Lehe, E. Esarey, and W. P. Leemans, "Pulse front tilt effects on laser plasma accelerators", in preparation.

[72] E. Esarey, B. Shadwick, P. Catravas, and W. Leemans, "Synchrotron radiation from electron beams in plasma-focusing channels", Physical Review E **65**, 056505 (2002).

[73] A. J. Gonsalves, K. Nakamura, C. Lin, D. Panasenko, S. Shiraishi, T. Sokollik, C. Benedetti, C. B. Schroeder, C. G. R. Geddes, J. van Tilborg, J. Osterhoff, E. Esarey, C. Toth, and W. P. Leemans, "Tunable laser plasma accelerator based on longitudinal density tailoring", Nat Phys **7**, 862–866 (2011).

[74] S. Steinke, J. van Tilborg, C. Benedetti, C. G. R. Geddes, C. B. Schroeder, J. Daniels, K. K. Swanson, A. J. Gonsalves, K. Nakamura, N. H. Matlis, B. H. Shaw, E. Esarey, and W. P. Leemans, "Multistage coupling of independent laser-plasma accelerators", Nature **530**, 190–193 (2016).

[75] S. Steinke, J. van Tilborg, C. Benedetti, C. G. R. Geddes, J. Daniels, K. K. Swanson, A. J. Gonsalves, K. Nakamura, B. H. Shaw, C. B. Schroeder, E. Esarey, and W. P. Leemans, "Staging of laser-plasma accelerators", Phys Plasmas **23**, 056705 (2016) `http://dx.doi.org/10.1063/1.4948280`.

[76] S. Shiraishi, C. Benedetti, A. J. Gonsalves, K. Nakamura, B. H. Shaw, T. Sokollik, J. van Tilborg, C. G. R. Geddes, C. B. Schroeder, C. Tóth, E. Esarey, and W. P. Leemans, "Laser red shifting based characterization of wakefield excitation in a laser-plasma accelerator", Phys Plasmas **20**, 063103 (2013) `http://dx.doi.org/10.1063/1.4810802`.

[77] K. Nakamura, H.-S. Mao, A. Gonsalves, A. Magana, J. Riley, C. Toth, and W. Leemans, "Diagnostics and controls for temporal structure of the bella laser system", in Aip conference proceedings, Vol. 1777, 1 (AIP Publishing, 2016), p. 110004.

[78] W. P. Leemans, C. E. Clayton, W. B. Mori, K. A. Marsh, P. K. Kaw, A. Dyson, C. Joshi, and J. M. Wallace, "Experiments and simulations of tunnel-ionized plasmas", Phys Rev A **46**, 1091–1105 (1992).

[79] W. Leemans, C. Clayton, W. Mori, K. Marsh, A. Dyson, and C. Joshi, "Plasma physics aspects of tunnel-ionized gases", Phys Rev Lett **68**, 321 (1992).

[80] J. K. Wahlstrand, Y.-H. Cheng, and H. M. Milchberg, "High field optical nonlinearity and the kramers-kronig relations", Phys Rev Lett **109**, 113904 (2012).

[81] F. Verluise, V. Laude, Z. Cheng, C. Spielmann, and P. Tournois, "Amplitude and phase control of ultrashort pulses by use of an acousto-optic programmable dispersive filter: pulse compression and shaping", Opt Lett **25**, 575–577 (2000).

[82] S. Artinian, J. Bergoz, F. Stulle, P. Pollet, and V. Schlott, "Development and first tests of a high sensitivity charge monitor for swissfel", Proceedings of IBIC **12** (2012).

[83] S. Artinian, J. Bergoz, F. Stulle, P. Pollet, and V. Schlott, "Goubau line and beam characterization of turbo-ict for swissfel", IPAC2013, MOPME005 (2013).

[84] K. Nakamura, D. E. Mittelberger, A. J. Gonsalves, J. Daniels, H.-S. Mao, F. Stulle, J. Bergoz, and W. P. Leemans, "Pico-coulomb charge measured at bella to percent-level precision using a turbo-ict", Plasma Phys Contr F **58**, 034010 (2016).

[85] D. T. Sandwell, "Biharmonic spline interpolation of geos-3 and seasat altimeter data", Geophys. Res. Lett. **14**, 139–142 (1987).

Appendix A

Electromechanical Jet Model

A.1 Jet Electrical Model

An analytical model of the jet was created to study the effects of operating voltage and backing pressure on the jet's operation and make predictions about jet performance. Electrically, the jet driver is a series RLC circuit (the jet solenoid, driver capacitors, and internal resistance) inductively coupled to an RL circuit (the plunger and flyer plate). The equivalent circuit is shown schematically in Figure A.1(a). The current through the solenoid, I_1, and the plate, I_2, are described by

$$L_1\frac{d^2}{dt^2}I_1(t) + R_1\frac{d}{dt}I_1(t) + \frac{1}{C_1}I_1(t) + M\frac{d^2}{dt^2}I_2(t) = 0 \tag{A.1}$$

$$L_2\frac{d^2}{dt^2}I_2(t) + R_2\frac{d}{dt}I_2(t) + M\frac{d^2}{dt^2}I_1(t) = 0 \tag{A.2}$$

where $M = k\sqrt{L_1 L_2}$ is the mutual inductance, $k \leq 1$ is the coupling coefficient of the two inductors, and R, L, and C are the effective resistance, capacitance, and inductance of their respective circuits. The initial condition is that the capacitors are charged to some applied voltage V and no current flows. The coupling coefficient $k \approx 1$ since the displacement of the plunger is small compared to the solenoid diameter and to the plunger plate diameter, as will be shown.

The model can be simplified, which allows for a closed-form analytical solution and more intuitive interpretation, by neglecting the mutual inductance term from the first equation since $L_2 \ll L_1$ (*i.e.* ignoring the plate's effect on the jet driver current as in Figure A.1(b)). The current through the gas jet driving circuit is then described by

$$\frac{d^2}{dt^2}I(t) + \frac{R}{L}\frac{d}{dt}I(t) + \frac{1}{LC}I(t) = 0 \tag{A.3}$$

where $I(t)$ is the time-varying current, L is the solenoid inductance, C is the equivalent capacitance in the jet driver, and R is the total resistance of the solenoid and cabling. The

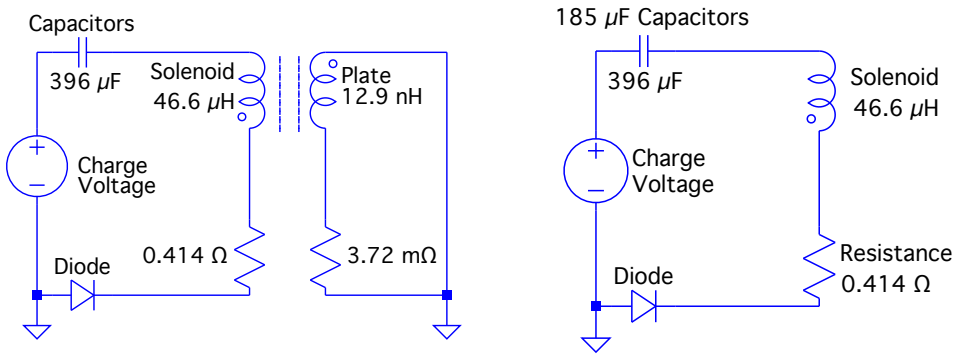

(a) Coupled model of the jet driver and piston plate.

(b) RLC model of the driver only.

Figure A.1: Electrical diagram of the coupled driver-jet circuit and the simplified driver circuit.

general solution to this equation is

$$I(t) = A_1 e^{-\alpha t} \sin(\omega t) + A_2 e^{-\alpha t} \cos(\omega t) \tag{A.4}$$

with the damped oscillation frequency is

$$\omega^2 = \omega_0^2 - \alpha^2 \tag{A.5}$$

where $\omega_0 = 1/\sqrt{LC}$ is the undamped oscillation frequency and $\alpha = R/2L$ is the attenuation factor. This solution assumes that the circuit is underdamped ($\omega_0 > \alpha$) which is the case for the jet in normal operation. The solution also assumes that the inductance L of the solenoid is fixed. The effective inductance of the solenoid is actually changing because of the moving plunger [48], but for the operating conditions here the maximum change in inductance is estimated to be $\leq 5\%$. To satisfy the initial conditions, it can immediately be seen that $A_2 = 0$. Further, the voltage across the inductor must be exactly opposite to the voltage across the capacitor in order that no current initially flows so

$$V = L\frac{d}{dt}I(t) = LA_1 e^{-\alpha t}[-\alpha \sin(\omega t) + \omega \cos(\omega t)]\Big|_{t=0} = \omega L A_1 \tag{A.6}$$

which gives $A_1 = V/L\omega$. The current through the inductor is thus

$$I(t) = \frac{V}{L\omega} e^{-\alpha t} \sin(\omega t). \tag{A.7}$$

This time-dependent current through the solenoid creates a changing magnetic flux in the conductive plate, which induces a current to flow. An N-turn solenoid generates a magnetic

flux Φ given by $\Phi = LI/N$. Since the displacement of the plunger is small compared to the solenoid diameter and to the plunger plate diameter, the coupling of the magnetic flux from the solenoid to the eddy current plate can be approximated as perfect (*i.e.* $\Phi_1 = \Phi_2$). Faraday's Law gives the electromotive force induced in the plate as

$$V_2(t) = -\frac{d\Phi_2}{dt} = -\frac{d\Phi_1}{dt} = \frac{-L_1}{N}\frac{dI_1(t)}{dt}. \tag{A.8}$$

The plate can be modeled as a single-turn solenoid (a loop of wire) for the purpose of circuit analysis. The effective area A_2, resistance R_2, and inductance L_2 of the loop are based on the geometry of the plate. The voltage drop going around the loop must equal the supplied voltage, so

$$V_2(t) = I_2 R_2 + L_2\frac{dI_2}{dt} = \frac{-L_1}{N}\frac{dI_1(t)}{dt}. \tag{A.9}$$

Provided the voltage drop from resistance is much larger than the reactance of the plate current ($R_2 \gg \omega L_2$), the inductive term can be dropped to yield

$$I_2 \approx V_2(t)/R_2 = \frac{-L_1}{NR_2}\frac{dI_1(t)}{dt} = \frac{-V}{NR_2}\frac{\omega_0}{\omega}e^{-\alpha t}\sin(\omega t + \phi) \tag{A.10}$$

where $\phi = \arctan(-\omega/\alpha)$.

Component	Measured	Uncertainty	Best Fit
Solenoid L	n.a.	n.a.	46.6 µH
Solenoid R	0.3 Ω	±0.1 Ω	0.414 Ω
Driver C	370 µF	±37 µF	396 µF
Plate L	n.a.	1-50 nH	12.9 nH
Plate R	n.a.	0.1-5 mΩ	3.72 mΩ

Table A.1: Measured and best fit circuit component values. Note: the presence of the aluminum plunger in the solenoid changes its effective impedance.

The best fit circuit component values listed in Table A.1 were used for both the numerical and analytic solutions. The solenoid resistance, R_1, and driver capacitance, C_1, were measured directly but the measurements both had $\gtrsim 10\%$ uncertainty. The effective resistance and inductance of the eddy currents in the plate,R_2 and L_2 respectively, could be estimated based on the geometry of the plunger plate. Starting from these estimates, best fit values for the driver components were determined by matching the analytical expression for the driver current with the measured current from the solenoid. The plunger plate resistance R_2 was set by matching the opening time of the gas jet model to the measured gas output. Although the parameter L_2 does not explicitly appear in the analytic model, comparing Eqn. A.1 with the derivative of Eqn. A.9 shows that the assumptions of the analytic model are equivalent to $M = \sqrt{L_1 L_2} = L_1/N$ or $L_2 \equiv L_1/N^2$.

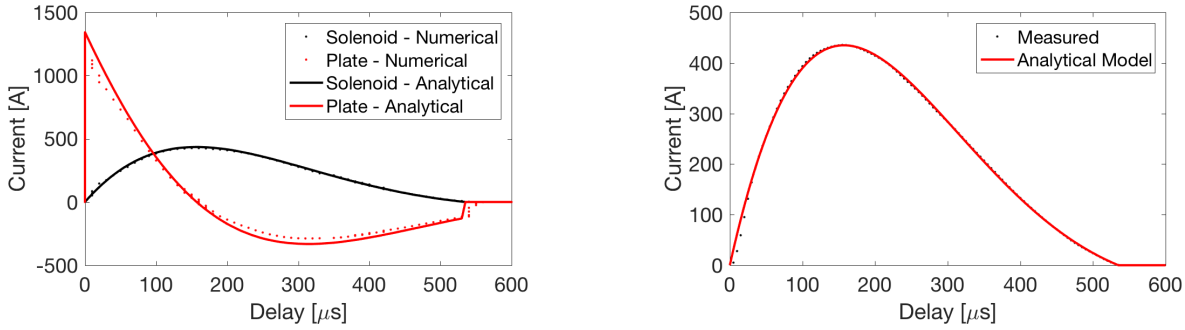

(a) Numerical vs analytical current solutions

(b) Measured current and analytical model

Figure A.2: Comparison of measured current profile, simplified analytical electrical model, and numerical solution.

The circuit shown in Figure A.1(a) which is described by Eqns. A.1 and A.2 was solved numerically using the commercial software package LTSpice (Linear Technology Corporation). The numerical solution agrees with the simplified analytical model given by Eqns. A.10 and A.7, as shown in Figure A.2(a). The analytical model also agrees with the measured current profile, shown in Figure A.2(b). Note a 100 µs delay between the jet trigger and the rising edge of the current, caused by the finite switching time of the driver electronics, has been removed from this plot.

A.2 Jet Operation Model

The motion of the plate was determined from the force between the plate and the solenoid. The solenoid current and the countercurrent in the plate result in each possessing a magnetic moment. The magnetic moment of an N-turn solenoid of area A is $d = NIA$. The interaction energy of two dipoles $\vec{d}_1$ and $\vec{d}_2$ is

$$U = \frac{\mu_0}{4\pi r^3}\left[\vec{d}_1 \cdot \vec{d}_2 - 3(\vec{d}_1 \cdot \hat{r})(\vec{d}_2 \cdot \hat{r})\right] \tag{A.11}$$

which results in a force

$$\begin{aligned}\vec{F} = \frac{3\mu_0}{4\pi r^4}\Big[&(\hat{r} \times \vec{d}_1) \times \vec{d}_2 + (\hat{r} \times \vec{d}_2) \times \vec{d}_1 - \\ &2\hat{r}(\vec{d}_1 \cdot \vec{d}_2) + 5\hat{r}((\hat{r} \times (\hat{r} \times \vec{d}_1) \cdot (\hat{r} \times \vec{d}_2))\Big]\end{aligned} \tag{A.12}$$

where $\vec{r}$ is the displacement between the dipoles. In the gas jet, rotational symmetry requires the dipole moments and displacement all be aligned so $\hat{d}_1 = \pm\hat{d}_2$ and $\hat{d}_1 = \pm\hat{r}$. This simplifies the force to

$$\vec{F} = \frac{\mp 3\mu_0}{2\pi r^4}(d_1 d_2)\hat{r} \tag{A.13}$$

where the $\mp$ refers to the dipoles being aligned or anti-aligned, respectively. The force between the solenoid and the plate is thus

$$\begin{aligned}\vec{F} &= \frac{-3\mu_0}{2\pi z^4}(NA_1I_1)(A_2I_2)\hat{z} \\ &\approx \frac{3\mu_0 A_1 A_2}{2\pi z^4}\frac{V^2}{L_1 R_2}\frac{\omega_0}{\omega^2}e^{-2\alpha t}\sin(\omega t)\sin(\omega t+\phi)\hat{z}.\end{aligned} \tag{A.14}$$

The plunger-solenoid force from Eqn. A.14 (the black curve in Figure A.3(a)) was incorporated into an electromechanical model of the jet's operation. The net force on the plunger is

$$\vec{F}_{net} = m\vec{a} = \vec{F}_{EM} + \vec{F}_{spring} + \vec{F}_{gas} \tag{A.15}$$

where m is the plunger mass. The spring force is given by Hooke's Law, $\vec{F} = -k_s(x + x_0)$, where k_s is the spring constant (250 lbs/in), x is the displacement of the jet plunger, and x_0 is the initial compression of the spring from a spacer ($x_0 = 0.5$ mm), added to ensure a sealing force even when $x = 0$. When the valve is closed, the gas force equals the plenum pressure times the area of the o-ring which seals the valve. The gas force on the plunger must also fall continuously to zero as the value is opened. To meet these requirements, the gas force was modeled by an exponential function, $\vec{F} = -PA\exp\{(-x/L_{gas})\}$ where P is the backing pressure and A is the area of the o-ring. The characteristic length of the gas interaction L_{gas} was taken to 0.3 mm, but varying this parameter of the model had only a small effect on the open time of the gas jet. The effective areas of the solenoid and plunger plate, A_1 and A_2, were estimated from their geometry to be 0.31 cm^2 and 0.35 cm^2. These forces and the resulting displacement of the gas jet plunger are shown as a function of time in Figure A.3(a).

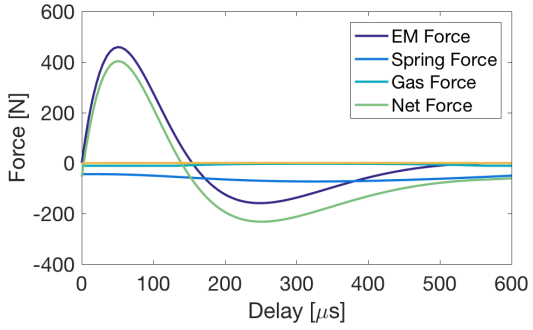

(a) Modeled forces and resulting displacement of the plunger in the gas jet.

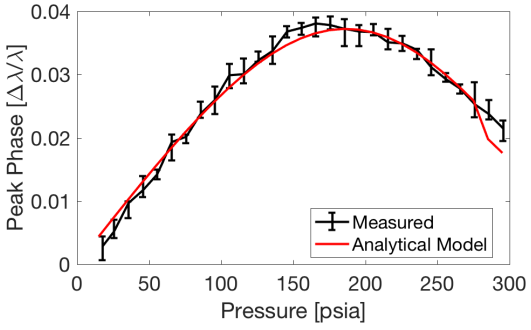

(b) Peak phase measured 10 mm above the gas jet and the simulated phase (Eqn. A.16) for varying pressure

Figure A.3: Model of get jet (a) predicts motion and opening time of jet and (b) matches measured phase scaling versus pressure.

An empirical model of the gas output of the jet was developed, since it is the gas density profile rather than the plate displacement which is measured. The gas output of the jet was assumed to be rise proportional to plunger displacement x and eventually saturate, since the flow is choked downstream at the jet throat for large x. The gas output can be modeled with these properties by

$$\phi = kP\left(1 - \exp\left\{-\left(\frac{x}{x_0}\right)^{\rho}\right\}\right) \tag{A.16}$$

where ϕ is the fractional phase shift from the gas, P is the backing pressure, $x(t - t_0)$ is the displacement of plunger, k is a scaling constant, x_0 is a characteristic distance beyond which the jet is open, ρ is the power of the roll off, and $t_0 = L/v_0$ is a time delay. The measurements are done a distance L away from the jet, and the time delay is caused by the gas flowing at an average speed v_0 from the gas jet to the measurement height. The function $x(t)$ comes from the electromechanical model and the backing pressure P and distance L of any particular measurement are known. The other parameters k, v_0, r, and x_0 were chosen to match the pressure scaling of the measured phase at fixed timing. The best fit is shown in Figure A.3(b).

Appendix B

Jet Alignment

Precise knowledge of the gas jet location and orientation relative to the laser axis is necessary to determine the density profile experienced by the laser as it propagated in the LPA experiment. The gas jet was mounted in the experimental chamber on a six-degree-of-freedom positioner (Model MX-824, Physik Instrumente GmbH) which has a stated repeatability of $\pm 0.1\mu$m and $\pm 2.5\mu$rad. This hexapod allowed the gas jet location and angle to be varied with respect to the laser. The angle and height to the laser were kept fixed for the LPA experiments. The longitudinal position (the distance from the gas jet to the BELLA laser vacuum focus) was kept fixed unless noted, as for the measurements of spectral shifting as a function of laser focus shown in Figure 5.10(a). Likewise, the transverse position was initially optimized and then left unchanged for the experiment. The absolute positioning and orientation of the gas jet in the LPA experiment is the subject of this Appendix.

B.1 Jet Longitudinal Position

The longitudinal location of the gas jet was determined by mounting a razor blade to the hexapod and determining the location where the razor was best imaged using an existing imaging system with a known magnification. An adjustable telescope that images the region near focus onto a camera, which is also used to determine its vacuum focal location, was used to determine the relative razor position. Using this method, the laser vacuum focus was measured to be 8.5 ± 1 mm downstream of the center of the gas jet nozzle at the hexapod position setting used in the LPA experiment.

B.2 Jet Height

The height of the laser axis above the jet nozzle outlet was determined from images of the laser-formed plasma taken by a camera mounted transverse the laser axis and the jet flow at the Target Chamber (see Figure 1.2). The spatial calibration of the camera was measured by moving the gas jet in 1 mm steps along the laser axis using the hexapod positioner and

finding the average spacing of the images of the gas jet. An averaged spatially-calibrated image of the plasma and partially-illuminated gas jet is shown in Figure B.1 along with a vertical lineout from the image that shows sharp features from the gas jet and the plasma. Based on this lineout, the jet height was determined to be 10 ± 0.25mm.

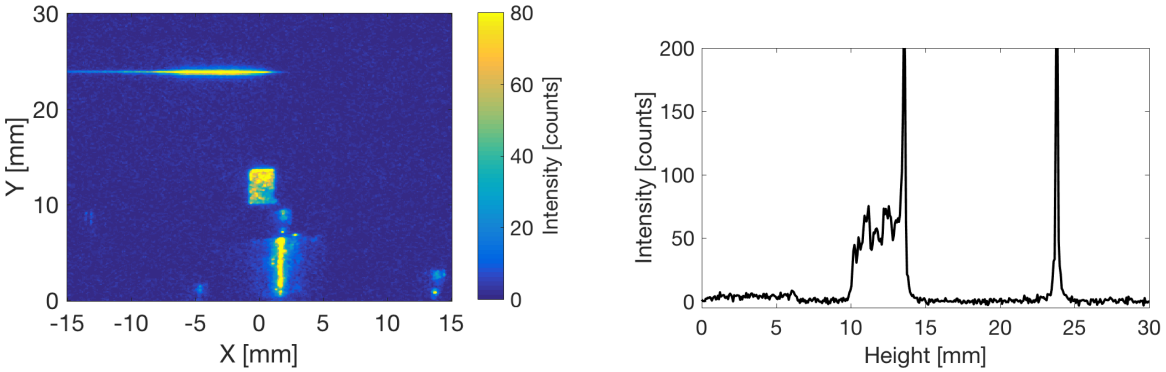

(a) View of plasma emission with gas jet illuminated by laser halo

(b) Vertical lineout through gas jet and plasma

Figure B.1: Determination of laser axis height above jet outlet

B.3 Jet Angle

The angular orientation of the jet (the angle between the jet's long axis and the laser axis) was set based on measurements using low-energy (0.5 J) laser operation. The gas jet was removed from the target chamber and reinstalled before the experiments, and additional measurements were taken to confirm that the angular orientation setting was still valid. However, re-analysis of both the initial orientation measurements revealed that the angle set point of the gas jet relative to the laser axis was not optimal (*i.e.* there was a non-zero angle between the laser axis and the long jet axis).

Initial Jet Alignment

The gas jet was aligned by repeatedly translating the jet transverse to the laser axis and monitoring the plasma emission for different jet angle settings. As the jet is translated through the laser, the total light emission from the plasma rises and falls in proportion to the total gas density along the laser axis. In the parallel orientation, the rise and fall is rapid, but if there is a relative angle between the gas jet and the laser axis the rise and fall will be more gradual, because the rotated gas jet has a wider transverse profile. Based on this technique, the gas jet angle setting was set to $\theta_{set} = 1.25°$. This alignment method assumes that the gas

output of the gas jet is constant, but as shown in Figure 3.4(a) there is a time-dependence in integrated jet density after the gas jet is first turned on. The time-dependence skews the results of any method based on total plasma emission.

The angular alignment data was reanalyzed based on the longitudinal center of the plasma emission, as determined by the horizontal centroid of the plasma emission light. The time-dependence affects the total density of the gas jet but not the gas distribution, so an alignment method based on normalized plasma emission such as a centroid will not be skewed. The horizontal location of the center of the plasma (plasma light centroid) as a function of transverse position is shown in Figure B.2 for various angle settings. It is clear that trend becomes symmetric for a setting between $-0.5°$ and $0°$ and increasingly asymmetric for larger or smaller angles. So, the angle setpoint at which the jet is best aligned is $\theta_{opt} = -0.25° \pm 0.25°$ and the relative angle with the laser axis was $\theta_{jet} = \theta_{set} - \theta_{opt} = 1.5° \pm 0.25°$. This corresponds to a clockwise rotation as seen by the plasma emission camera.

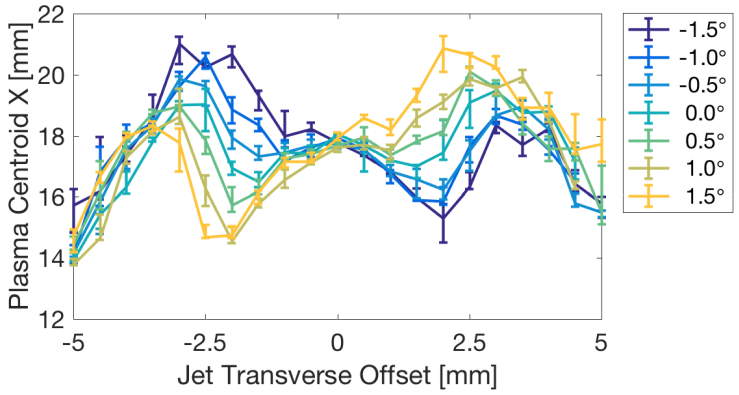

Figure B.2: Trend of plasma centroid location along the laser axis vs transverse offset for different hexapod angle set points.

Jet Alignment After Reinstallation

The mounting screws which attach the jet nozzle to the larger valve assembly and their washers are visible in some of the plasma images taken during the initial alignment, although the nozzle itself is obscured by light from the plasma. The screws are also visible in some of the plasma images taken close to the experiment after the final re-installation of the gas jet. *A priori* the screw locations cannot be used as fiducial markers of the nozzle location because there is some freedom to reposition the jet nozzle relative to the screws when they are loosened, but comparison of jet images from the initial alignment and near the experiment shows the screws' washers remained in the same position relative to their respective screws, indicating the screws were never loosened nor disassembled. Using these screws' outlines

as references it was possible to determine the relative rotation of the gas jet between the experiment and the initial alignment measurements. Based on the location of the screws mounting the nozzle and their washers, the jet rotated by $\Delta\theta_{jet} = -1.5^\circ \pm 1^\circ$ where the negative indicates the rotation was in the counterclockwise direction as viewed by the plasma emission camera. The uncertainty is the additional rotation necessary for the outlines of the screws and washers to be noticeably misaligned.

The camera recording images of the gas jet and plasma could itself have rotated slightly relative to the laser axis. The orientation of the plasma is physically fixed to the laser axis because the plasma is created by the laser, and the laser axis is fixed by alignment monuments. Thus any apparent change in the plasma orientation is a result of camera rotation. Images of the plasma from the time of the initial alignment and from near the experiment were averaged separately, and the averaged images were analyzed and compared to determine the relative rotation of the camera. The analysis consisted of thresholding the plasma image to a percentage of it's maximum and fitting a rotated ellipse to the boundary of the thresholded plasma. The angle of the rotated ellipse's major axis is the plasma angle, which defines the relative angle between the camera and the laser axis. The average and standard deviation of the plasma angles over the range of image thresholds 20%, 25%, 30%, $\cdots$, 90% was calculated for each averaged image. The apparent change in plasma angle, actually caused by rotation of the camera, was $\Delta\theta_{plasma} = -0.1^\circ \pm 0.4^\circ$, where the sign is consistent with the jet angle setpoint definition. The angle of the jet during the experiment relative to the laser axis was therefore $\theta_{jet,exp} = \theta_{jet} + \Delta\theta_{jet} - \Delta\theta_{plasma} = -0.1^\circ \pm 1.1^\circ$.

B.4 Jet Transverse Position

The jet transverse position was determined based on the distribution of light from the laser-formed plasma, integrated along the laser axis, as a function of transverse gas jet position. When the laser axis is well centered on the jet, the plasma emission light decreases symmetrically with distance from the laser axis, as shown in Figure B.3(a) near 0 transverse offset. However, when the laser is offset from the gas jet center there is a density gradient so the plasma light falls off faster on the low-density side of the laser axis than the high-density side. This trend is clearest in Figure B.3(b) where each longitudinally-integrated plasma profile from Figure B.3(a) is normalized to its peak intensity. The second moment of these profiles are plotted in black in Figure B.3(c). Plotted in red are the second moment of the plasma profiles taken from a similar scan on the day of the experiment with a smaller range of transverse offsets. Because of differences in jet timing and distance from the laser axis, the emission on the day of the experiment was much higher intensity which causes the sharper features in Figure B.3(c). The zero-point of transverse offset here is defined as the location of the jet during the experiment. The transverse offset based on this method is $\Delta y = 50 \pm 200$ µm.

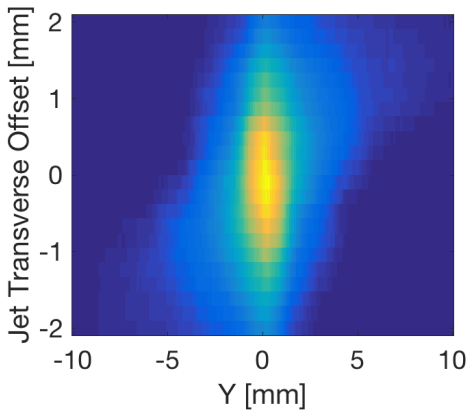

(a) Transverse profile of plasma emission vs jet transverse offset

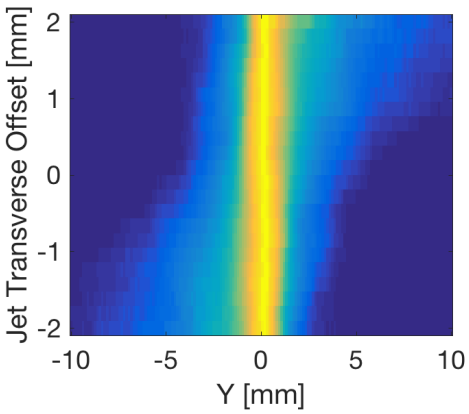

(b) Normalized transverse profile of plasma emission vs jet transverse offset

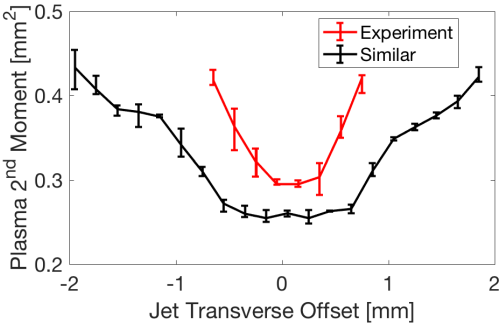

(c) Plasma second moment vs transverse offset for two gas jet densities

Figure B.3: Determination of jet center.